이학박사학위논문

Surface-Enhanced Raman Scattering of 4-Aminobenzenethiol and 4-Nitrobenzenethiol at Silver and Gold Nanogaps and Nanostructures

은과 금 나노 틈 및 나노 구조체에서의 4-아미노벤젠치올과 4-니트로벤젠치올의 표면 증강 라만 산란

2015년 2월

서울대학교 대학원

화학부 물리화학 전공

최 정 용

Surface-Enhanced Raman Scattering of 4-Aminobenzenethiol and 4-Nitrobenzenethiol at Silver and Gold Nanogaps and Nanostructures

은과 금 나노 틈 및 나노 구조체에서의 4-아미노벤젠치올과 4-니트로벤젠치올의 표면 증강 라만 산란

지도교수: 김 관

이 논문을 이학박사 학위논문으로 제출함

2014 년 11 월

서울대학교 대학원

화학부 물리화학전공

최 정 용

최정용의 이학박사 학위논문을 인준함

2014 년 11 월

위 원 장 _____ ㊞

부위원장 _____ ㊞

위 원 _____ ㊞

위 원 _____ ㊞

위 원 _____ ㊞

Ph. D. Thesis

Surface-Enhanced Raman Scattering of 4-Aminobenzenethiol and 4-Nitrobenzenethiol at Silver and Gold Nanogaps and Nanostructures

Supervisor: Professor Kwan Kim

Major: Physical Chemistry

By Jeong Yong Choi

Department of Chemistry

Graduate School of Seoul National University

2015

Abstract

Surface-Enhanced Raman Scattering of 4-Aminobenzenethiol and 4-Nitrobenzenethiol at Silver and Gold Nanogaps and Nanostructures

Jeong Yong Choi
Department of Chemistry, Physical Chemistry
The Graduate School
Seoul National University

In Chapter 1, "The General Introduction", we provide background information on surface-enhanced Raman scattering (SERS), along with the characteristics of "finite-difference time-domain (FDTD) method" adopted in this thesis.

In Chapter 2, SERS spectra of 4-nitrobenzenethiol (4-NBT) and 4-aminobenzenethiol (4-ABT) on Ag obtained under ambient conditions and in icy environments at 77 K are presented. This study was conducted to resolve the debate on the origin of b_2-type bands appearing in the SERS of 4-NBT and 4-ABT. The origin of b_2-type bands in the SERS of 4-NBT and 4-ABT has recently been debated because these bands are very similar to those attributed to a photoreaction product such as 4,4′-dimercaptoazobenzene (4,4′-DMAB). We confirmed in this work that under ambient conditions, the b_2-type bands distinctly appeared in the SERS spectra of both 4-NBT and 4-ABT. In contrast, no b_2-type peaks appeared in the SERS of 4-NBT in icy environments, suggesting that 4-NBT did not undergo a photoreaction. However, the SERS spectral pattern of 4-ABT was the same both at room

temperature and in icy conditions. Based on our separate observation that hot electrons are plasmonically generated from Ag even in icy environments, the lack of photoreaction of 4-NBT is likely a result of the small spaces between the ice crystals, rendering the N–O bond difficult to break. The situation of 4-ABT on Ag is identical to that of 4-NBT on Ag in the same conditions; therefore, the b_2-type bands observed in icy conditions must be because of the 4-ABT, and not because of the production of 4,4′-DMAB or other photoreaction products. Regardless of temperature, hot electrons were more easily generated at lower excitation wavelengths, and the b_2-type bands appeared more distinctly with a decrease in the excitation wavelength. From these observations, we conclude that the hot electrons, as well as the b_2-type bands of 4-ABT, are associated with the charge-transfer chemical enhancement mechanism in SERS.

In Chapter 3, SERS of 4-ABT at the nanogaps between metal nanoparticles and a flat Au substrate is described. This study was conducted to understand the characteristics of one kind of 'hot' site for SERS. In fact, although no Raman signal is observable when 4-ABT, for instance, is self-assembled on a flat Au substrate, a distinct spectrum is obtained when Ag or Au nanoparticles are adsorbed on the pendent amine groups of 4-ABT. This is definitely due to the electromagnetic coupling between the localized surface plasmon of Ag or Au nanoparticle with the surface plasmon polariton of the planar Au substrate, allowing an intense electric field to be induced in the gap even by visible light. On this basis, firstly, we have thoroughly examined the size effect of Ag nanoparticles, along with the excitation wavelength dependence, by assembling 4-ABT between planar Au and a variable-

size Ag nanoparticle (from 20- to 80-nm in diameter). Regarding the size dependence, a higher Raman signal was observed when larger Ag nanoparticles were attached onto 4-ABT, irrespective of the excitation wavelength. Regarding the excitation wavelength, the highest Raman signal was measured at 568 nm excitation, slightly larger than that at 632.8 nm excitation. The Raman signal measured at 514.5 and 488 nm excitation was an order of magnitude weaker than that at 568 nm excitation, in agreement with the three-dimensional finite-difference time domain (3-D FDTD) simulation. It is noteworthy that placing an Au nanoparticle on 4-ABT, instead of an Ag nanoparticle, the enhancement at the 568 nm excitation was several tens of times weaker than that at the 632.8 nm excitation, suggesting the importance of the localized surface plasmon resonance of the Ag nanoparticles for an effective coupling with the surface plasmon polariton of the planar Au substrate to induce an very intense electric field at the nanogap.

In addition, secondly, the Raman spectral characteristics of 1,4-phenylenediisocyanide (1,4-PDI) and 4-ABT positioned at the nanogap formed by Au/Ag alloy nanoparticles and a flat Au substrate were examined, and 3-D FDTD calculations were carried out. More intense Raman signal was measured, regardless of the excitation wavelength, when Ag-rich Au/Ag alloy nanoparticles were used to form the nanogaps. Regarding the excitation wavelength, 568 nm light was the most effective in inducing a Raman signal, particularly when Ag nanoparticles were adsorbed on 1,4-PDI or 4-ABT, whereas 632.8 nm light was slightly more effective than 568 nm light when Au nanoparticles were adsorbed onto them. The Raman spectra of 1,4-PDI could be attributed to the electromagnetic enhancement

mechanism. The dependencies of the Raman spectra of 1,4-PDI on the excitation wavelength and the type of Au/Ag alloy nanoparticle were comparable to those predicted by the 3-D FDTD calculations. From the measured NC stretching frequencies, the surface of 35-nm sized Au/Ag alloy nanoparticles containing more than 5 mole percent of Ag atoms was concluded to be covered fully with Ag atoms. The Raman spectra of 4-ABT were interpreted to be a product of electromagnetic and chemical enhancement mechanisms. Assuming that the Raman intensity ratios of the b_2- and a_1-type bands were indicative of the extent of chemical enhancement, the Ag-to-4-ABT electron transfer appeared more facile than the Au-to-4-ABT transfer did and more favorable by excitation with a 514.5 nm laser than 568 nm or 632.8 nm laser.

In Chapter 4, SERS of 4-NBT at the nanogaps between a planar Au substrate and a Ag nanostructure is described. This study was conducted to appreciate the effectiveness of 'hot' electrons plasmonically generated from Ag nanoparticles. As described in Chapter 2, 4-NBT adsorbed on a nanostructured Ag substrate can be reduced to 4-ABT by the irradiation of a visible laser. In order to evaluate the effectiveness of hot electrons generated from Ag, we have carried out a SERS study by forming a nanogap system composed of a planar Au substrate and an Ag-coated micrometer-sized silica bead, wherein 4-NBT was adsorbed firstly onto the Au substrate and then Ag-coated silica beads, derivatized with 1-alkanethiols, were spread over the 4-NBT layer: the distance between 4-NBT and a nanostructured Ag substrate was varied by the chain length of alkanethiol molecules. Although the planar Au substrate itself was ineffective in the reduction of 4-NBT, hot electrons

usable in the reduction of 4-NBT were generated from the Ag-coated silica beads. The hot electrons generated by 514.5-nm radiation were more effective in the reduction of 4-NBT to 4-ABT than those generated by 632.8-nm radiation, although the nanogap was more SERS-active with the excitation at 632.8-nm than at 514.5-nm. The photoreduction efficiency of hot electrons nonetheless decreased linearly with the distance they travelled from the Ag surface: the reduction capability at a distance of 2 nm apart is about one fourth of that in contact situations.

***Keywords**: Surface-enhanced Raman scattering, SERS, 4-Nitrobenzenethiol, 4-Aminobenzenethiol, 4,4'-Dimercaptoazobenzene, 1,4-Phenylenediisocyanide, Hot electron, Hot spot, Electromagnetic mechanism, Chemical enhancement, Charge-transfer, b2-type band, Alloy nanoparticle, Finite-difference time-domain, FD TD, Nanogap*

Student Number: 2008-22740

Contents

List of Figures

Chapter 1

Chapter 2

nm radiation; b_2-type bands are starred in the figures.

Figure 2.4. Relative peak intensities of the (a) 9b, (b) 3, and (c) 19b bands of 4-ABT on Ag compared to the 7a band, i.e. I(ν_{9b})/I(ν_{7a}), I(ν_3)/I(ν_{7a}), and I(ν_{19b})/I(ν_{7a}), measured under ambient conditions (filled circles) and in icy environments (open circles); plotted against excitation wavelengths. Error bars indicate the average and standard deviation from the experiments performed in triplicate.

Figure 2.5. Series of SERS spectra of 4-ABT on Ag obtained after cooling a surrounding acidic solution (pH 3) down to 77 K using an excitation source of 514.5 nm; b_2-type bands are starred in the figure.

Chapter 3

Figure 3.1. (a) TEM images of four different Ag nanoparticles prepared in this work (scale bar = 100 nm), (b) their histograms of size distribution, and (c) their UV/vis absorption spectra in colloid state.

Figure 3.2. FE-SEM images of Ag@4-ABT/Au measured after soaking in Ag sol, comprised of (a) 20-, (b) 40-, (c) 60-, and (d) 80-nm sized Ag particles, for 1 h (scale bar = 200 nm).

Figure 3.3. Normal Raman spectra of 4-ABT (a) in neat solid state and (b) in anionic state in alkaline solution, taken using the 632.8 nm line of a He/Ne laser (top), the 568 nm line of an Ar/Kr laser (middle), and the 514.5 nm line of an Ar ion laser (bottom) as excitation sources. All spectral intensities were normalized with respect to those of silicon wafers used for instrument calibration.

Figure 3.4. SERS spectra of 4-ABT on flat Au taken after soaking for 1 h in Ag sol

comprised of (a) 20-, (b) 40-, (c) 60-, and (d) 80-nm sized Ag particles, using 632.8, 568, 514.5, and 488 nm radiation (from top to bottom) as the excitation sources. All spectra were taken while spinning at 3000 rpm to minimize the effect of inhomogeneous distribution of Ag nanoparticles. In addition, all spectral intensities were normalized with respect to those of silicon wafers used for instrument calibration and also to the number of Ag nanoparticles adsorbed on 4-ABT on Au.

Figure 3.5. (a) Experimental and (b) theoretical enhancement factors (EFs) determined for the 7a band of 4-ABT in Ag@4-ABT/Au drawn as a function of the excitation wavelength, as well as the size of Ag nanoparticles. Experimental EFs were determined by referring to the SERS spectra shown in Figure 3. Theoretical EFs were predicted using the 3D-FDTD method by taking into account the portions of the perpendicular and parallel polarizations in actual experimental conditions. See text.

Figure 3.6. Intensity distribution ($|E/E_0|^4$) of induced local electric field E relative to the excitation field E_0 near 80-nm sized Ag sphere and Au cuboid, calculated by the 3D-FDTD method in a condition that the electric field (568 nm radiation) is directed perpendicular (a and b) or parallel (c and d) to the surface of the Au cuboid. Insets are the magnified images of the gap sites.

Figure 3.7. The relative peak intensities of the (a) 3, (b) 9b, and (c) 19b bands of 4-ABT in Figure 3.4 with respect to the 7a band, i.e., $I(\nu_3)/I(\nu_{7a})$, $I(\nu_{9b})/I(\nu_{7a})$, and $I(\nu_{19b})/I(\nu_{7a})$, drawn versus the excitation wavelength. All of the symbols shown were the average of 5 different measurements with the error bars denoting their standard deviation.

Figure 3.8. (a) UV/vis absorption spectra of Ag, $Au_{0.5}Ag_{0.5}$, $Au_{0.95}Ag_{0.05}$, and Au nanoparticles in the colloid state. (b) Positions of surface plasmon bands plotted against the mole fraction of Ag (x_{Ag}) in the nanoparticles.

Figure 3.9. FE-SEM images measured after soaking 1,4-PDI/Au for 1 h in (a) Ag, (b) $Au_{0.5}Ag_{0.5}$, (c) $Au_{0.95}Ag_{0.05}$, or (d) Au sols (scale bar = 200 nm).

Figure 3.10. Raman spectra of 1,4-PDI/Au measured after soaking for 1 h in (a) Ag, (b) $Au_{0.5}Ag_{0.5}$, (c) $Au_{0.95}Ag_{0.05}$, or (d) Au sols, using 632.8-, 568-, or 514.5-nm radiation (from top to bottom) as the excitation source.

Figure 3.11. (a) Extinction spectra and (b) electric field intensities calculated by the 3D-FDTD method for nanogaps composed of a 35-nm Ag, $Au_{0.5}Ag_{0.5}$, $Au_{0.95}Ag_{0.05}$, or Au sphere and a Au cuboid. Spectra in (a) correspond, from left to right, to Ag, $Au_{0.5}Ag_{0.5}$, $Au_{0.95}Ag_{0.05}$, and Au spheres. Wavelengths of excitation lasers used in this work are marked as vertical lines; their Stokes regions (covering 800 to 2400 cm^{-1}) are marked with shaded areas. Intensities in (b) refer to those at the gap center determined as a function of the wavelength of an illuminating light. (c) Experimental EFs determined for the 9a band of 1,4-PDI and (d) FDTD-calculated EFs drawn as a function of excitation wavelength and Au/Ag alloy nanoparticle type. For (c), the error bars indicate the average and standard deviation of 3 different measurements.

Figure 3.12. Raman spectra of 4-ABT/Au measured after soaking for 1 h in (a) Ag, (b) $Au_{0.5}Ag_{0.5}$, (c) $Au_{0.95}Ag_{0.05}$, or (d) Au sols, using 632.8-, 568-, or 514.5-nm radiation (from top to bottom) as the excitation source. Starred peak is the 7a band of 4-ABT.

Figure 3.13. Relative peak intensity of the 19b and 7a bands of 4-ABT in Figure

3.12 drawn versus the mole fraction of Ag (x_{Ag}) in Au/Ag alloy nanoparticles and the excitation wavelength. The error bars indicate the average and standard deviation of 3 different measurements.

Chapter 4

Figure 4.1. FE-SEM images of 1 μm-sized silica beads recorded (a) before and (b) after silvering them using butylamine as the reductant of $AgNO_3$.

Figure 4.2. SERS spectra of 4-mercaptobenzoic acid (4-MBA) adsorbed on Ag-coated silica beads measured at (a) 514.5 nm and (b) 632.8 nm excitations. (c) Normal Raman spectrum of 4-MBA.

Figure 4.3. (a) AFM image of a vacuum-evaporated Au film on a glass slide and (b) optical microscope image of micrometer sized, Ag-coated silica beads spread on an Au film.

Figure 4.4. Raman spectra of Ag@C_n0/4MBA/Au, Ag@C_n4/4MBA/Au, Ag@C_n10/4MBA/Au, and Ag@C_n16/4MBA/Au obtained using (a) 514.5 nm and (b) 632.8 nm radiations as the excitation sources. (c) Intensity variation of the 4-MBA ring 8a band versus the chain length observed in (a) and (b).

Figure 4.5. Raman spectra of Ag@C_n0/4NBT/Au, Ag@C_n4/4NBT/Au, Ag@C_n10/4NBT/Au, and Ag@C_n16/4NBT/Au obtained using (a) 514.5 nm and (b) 632.8 nm radiations as the excitation sources.

Figure 4.6. (a) Intensity variation of the 4-NBT NO_2-stretching band in Figure 4.5(a) and (b) that in Figure 4.5(b) represented versus the chain length. The dotted lines represent the NO_2-stretching band intensities expected when 4-NBT has not been

subjected to a photoreduction. See text.

Figure 4.7. (a) Relative peak intensities of the 4-ABT ring 7a band at ~1080 cm^{-1} and (b) ring 19b band at 1435 cm^{-1}, both measured with respect to the peak intensities of the NO_2-stretching band at 1350 cm^{-1} in Figures 4.5(a) (see filled circles) and 5.5(b) (see open circles). The relative peak intensities are represented versus the chain length.

Figure 4.8. Raman spectra of Ag@C_n0/4ABT/Au and Ag@C_n4/4ABT/Au measured using (a) 514.5 nm and (b) 632.8 nm radiations as the excitation sources. (c) Relative peak intensities of the b_2-type bands measured with respect to the ring 7a band in (a) represented versus the chain length. (d) Similar ratios plotted using the data in (b).

List of Tables

Chapter 1

Table 1.1. The electromagnetic spectra in the wavelength scale in meters.

Chapter 3

Table 3.1. Raman spectral peaks of 4-aminobenzenethiol measured in free and surface adsorbed state using the excitation laser of 568 nm.

List of Schemes

Chapter 2

Scheme 2.1. Experimental arrangement for the measurement of SERS spectra of 4-NBT, 4-ABT, and Fe^{3+}-adsorbed cyanide on Ag in ice, performed at the temperature of liquid N_2 (77 K).

Chapter 3

Scheme 3.1. Schematic diagram of a nanogap, formed by a planar Au substrate and a spherical Ag nanoparticle (20-, 40-, 60-, and 80-nm in diameter), in which a probe molecule, 4-aminobenzenethiol, is bound via thiolate sulfur and amine group to Au and Ag, respectively.

Scheme 3.2. A scheme for the preparation of a nanogap and the enhancement factor

Chapter 4

Scheme 4.1. A scheme for the preparation of a nanogap and the subsequent Raman spectral measurement adopted in this work.

Chapter 1

: Introduction

1.1. Raman Scattering

1.1.1. Basic Theory

When Light interacts with matter, the photons which make up the light may be absorbed or scattered, or may not interact with the material and may pass straight through it. If the energy of an incident photon corresponds to the energy gap between the ground state of a molecule and an excited state, the photon may be absorbed and the molecule promoted to the higher energy excited state. It is this change which is measured in absorption spectroscopy by the detection of the loss of that energy of radiation from the light. However, it is also possible for the photon to interact with the molecule and scatter from it. In this case there is no need for the photon to have an energy which matches the difference between two energy levels of the molecule. The scattered photons can be observed by collecting light at an angle to the incident light beam, and provided there is no absorption from any electronic transitions which have similar energies to that of the incident light, the efficiency increases as the fourth power of the frequency of the incident light.

Scattering is a commonly used technique. For example, it is widely used for measuring particle size and size distribution down to size less than 1 μm. One every day illustration of this is that the sky is blue because the higher energy blue light is scattered from molecules and particles in the atmosphere more efficiently than the lower energy red light. However, the main scattering technique used for molecular identification is Raman scattering.

The process of absorption is used in a wide range of spectroscopic

techniques. For example, it is used in acoustic spectroscopy where there is a very small energy difference between the ground and excited state and in X-ray absorption spectroscopy where there is a very large difference. In between these extremes are many of the common techniques such as NMR, EPR, infrared absorption, electronic absorption and fluorescence emission, and vacuum ultraviolet (UV) spectroscopy. Table 1.1 indicates the wavelength ranges of some commonly used types of radiation.

X-rays	UV-visible	near IR	mid IR	far IR	micro-radio
10^{-11}	10^{-7}	10^{-6}	10^{-5}	10^{-4}	10^{0}

Table 1.1. The electromagnetic spectra in the wavelength scale in meters.

Radiation is often characterized by its wavelength (λ). However, in spectroscopy, because we are interested in the interaction of radiation with stats of the molecule being examined and this being usually discussed in terms of energy, it is often useful to use frequency (ν) or wavenumber ($\tilde{\nu}$) scales, which are linearly related with energy, The relationships between these scales are given below:

$$\lambda = c / \nu$$

$$\nu = \Delta E / h$$

$$\tilde{\nu} = \nu / c = 1 / \lambda$$

It is clear from above equations that the energy is proportional to the reciprocal of

wavelength and therefore the highest energy region is on the left in Figure A-2 and the longest wavelength on the right.

The way in which radiation is employed in infrared or Raman spectroscopy is different. In infrared spectroscopy, infrared energy covering a range of frequencies is directed onto the sample. Absorption occurs where the frequency of the incident radiation matched that of a vibration so that the molecule is promoted to a vibrational excited state. The loss of this frequency of radiation from the beam after it passed through the sample is then detected. In contrast, Raman spectroscopy uses a single frequency of radiation to irradiate the sample and it is the radiation scattered from the molecule, one vibrational unit of energy different form the incident beam, which is detected. Thus unlike infrared absorption, Raman scattering does not require matching of the incident radiation to the energy difference between the ground and excited state. In Raman scattering, the light interacts with the molecule and distorts (polarizes) the cloud of electrons around the nuclei to form a short-lived state called a 'virtual state'. This state is not stable and the photon is quickly reradiated.

The Raman spectroscopy provide information about molecular vibrations. Raman effect relies on inelastic scattering of monochromatic radiation source. In elastic scattering called Rayleigh scattering, the molecule is excited to a virtual state, and then relaxes back to the original vibrational state by re-radiating a photon at the same frequency as the incident light. The molecule absorbs no energy from the incident radiation in this case.[1,2]

Only a very small fraction of molecules undergo inelastic scattering called Raman scattering. When the excited molecule relaxes to a different vibrational state,

rather than to the original state, the Raman scattering occurs. The energy of inelastically scattered light is different from that of the incident light. In the Raman spectrum, the energy gap between the incident and scattered lights appears as a frequency shift between the scattered light ν' and the excitation frequency ν. These two frequencies, ν and ν', are related to the vibrational energy by the following equation (see also Figure 1.1):

$$h\nu = h\nu' + \Delta E_{vibration} \tag{3}$$

It should be noted that in Raman experiments, the final vibrational state of the molecule can be either higher or lower than the original state. In the case where the final vibrational state is lower than the original state, the scattered light has a higher frequency than the incident light. Thus, a blue shift from the excitation frequency is observed. Raman bands of this type are called anti-Stokes line. Similarly, a red shift from the incident radiation is observed when the final state exhibits higher energy than the original state; these Raman bands are referred to as Stokes lines. Since most of the molecules are at ground vibrational state (υ = 0) at room temperature, the Stokes lines exhibit higher Raman intensity than the corresponding anti-Stokes lines which originate from an elevated vibrational state (υ = 1). Therefore, the Stokes lines are more commonly used for molecular characterization.

If the direction of observation of the radiation scattered by the sample is perpendicular to the direction of the incident polarized laser beam source, and also to its direction vector, polarized Raman spectra can be obtained. A polarizer is placed

between the sample and the spectrometer. It can be oriented parallel and perpendicular to the electric vector of the incident radiation. The Raman band intensity ratio, namely the perpendicular polarization intensity divided by the parallel polarization intensity, is called the depolarization ratio ρ. With a laser source, a totally symmetric vibration will generate a polarized Raman band where ρ has a value between 0 and 3/4. A vibration that is not totally symmetric will generate a depolarized Raman band where $\rho = 3/4$.

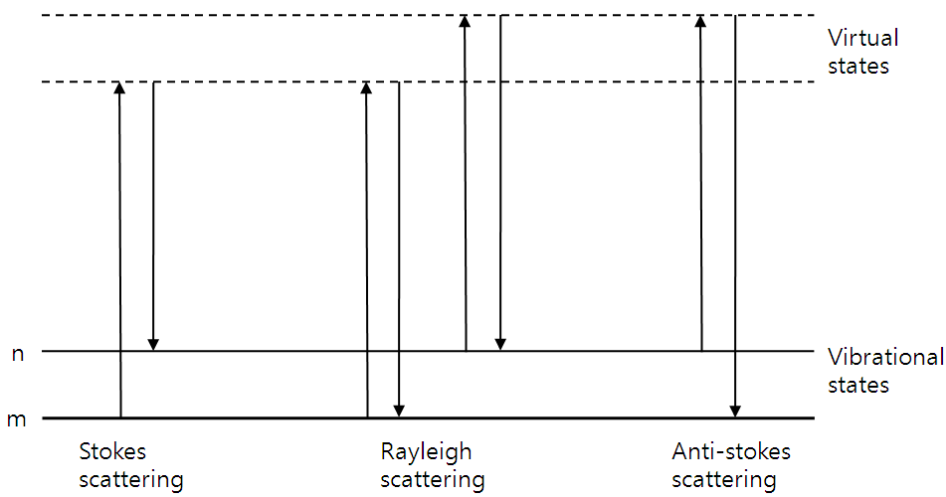

Figure 1.1. Diagram of the Rayleigh and Raman scattering processes.

1.1.2. Selection Rules

A vibrational mode is IR-active when the dipole moment of the molecules changes during the vibration; a vibrational mode is Raman-active when polarizability changes during the vibration. Specifically, antisymmetric vibrational modes and vibrations due to polar groups are more likely to reveal remarkable infrared

absorption, while a symmetric vibrational mode shows strong Raman activity. Molecules with a symmetry center have no fundamental lines in common in the IR and Raman spectra. This is called as the mutual exclusion rule.

1.2. Surface Enhanced Raman Scattering (SERS)

1.2.1. Mechanisms of SERS

Surface-enhanced Raman scattering (SERS) is a process in which the apparent Raman cross sections of molecules, adsorbed on roughened metal surfaces and particles, are magnificently enhanced by local electromagnetic fields.[3-14] According to theoretical studies, there are two major mechanisms which have proposed, one is an electromagnetic enhancement (EM) mechanism and the other is a chemical enhancement (CHEM) mechanism.[15,16] The EM mechanism is based on the enhanced electromagnetic fields which can be generated on metal surface with appropriate morphology and the CHEM mechanism on changes in the electronic structure of molecule which occur upon adsorption and which can bring about to resonance Raman scattering.

1.2.2. Electromagnetic (EM) enhancement

The plasmon is a collective oscillation of the electron cloud of the conductor; if the collective oscillation is enclosed to the surface region it is called surface plasmon. The surface plsmon resonance is resonant oscillation of conduction electrons at the interface between a negative and positive permittivity material stimulated by incident light. There are two types of SPRs that can be generated, one is surface plasmon polaritons (SPPs)[17-19] which appears from propagating waves along a metal surface and the other is localized surface plasmon resonance (LSPR)[18,20-22] which is localized to a volume with dimensions smaller than the wavelength of incident

radiation. The electromagnetic field can be coupled into the free conduction electrons at the metal surface. Typically, Au, Ag, or Cu thin films are used as metal substrates. Light will also interact with metal nanoparticles which is smaller than the wavelength of incident light to generate a LSPR because the dimensions of the particle are too small to provide for a propagating wave. Small spherical particles have a single and sharp absorption band due to the excitation of a dipole plasmon resonance, where the total charge distribution of the particle oscillates at the frequency of the incident radiation. See Figure 1.2. The electromagnetic field near the surface can be hugely enhanced under circumstance of excited surface plasmon; the amplification of both the incident field and the scattered Raman field via their interaction near the surface constitutes the electromagnetic enhancement. Electromagnetic enhancement depends on Raman active probe molecules being restricted within these electromagnetic fields and contributes an enhancement factor of 10^4.

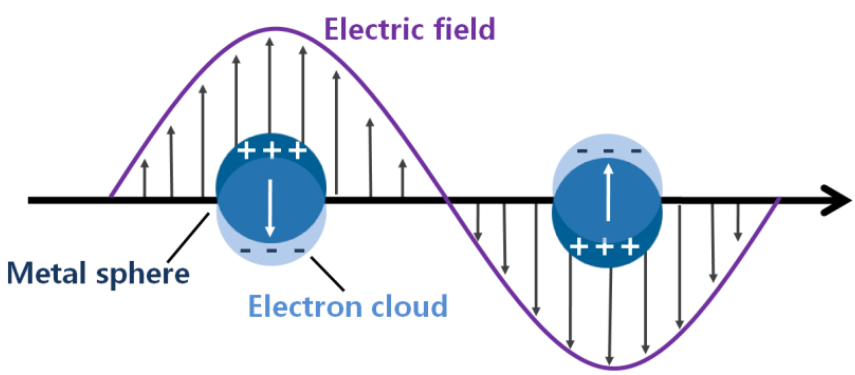

Figure 1.2. Illustration of generation of the localized surface plasmon resonance of spherical metal nanoparticles by incident electromagnetic field.

Many theoretical modeling has been carried out to provide understanding

of electromagnetic enhancement by noble metal nanoparticles. The simple example of an isolated metal sphere, with a quasi-static description of the incident electromagnetic field, has been used to derive the proportionality

$$E^2 \propto E_0^2 \left| \frac{\varepsilon_m - \varepsilon_0}{\varepsilon_m - 2\varepsilon_0} \right|^2$$

in which E is the electric field intensity at the surface on the sphere, E_0 is the incident field intensity, ε_m is the wave-dependent dielectric constant of the metal consisting the sphere, and ε_0 is the dielectric constant of the surrounding environment around the metal sphere. This relation revels that when $\varepsilon_m = -2\varepsilon_0$, which can be achieved for Au and Ag at certain wavelength in the near IR and visible regions, the intensity of the electric field at the surface of the metal sphere becomes very strong. This enhancement of electric field is induced by satisfying the LSPR condition. Similar relations can be derived for the scattering and extinction cross sections of the metal nanoparticle. Maximization of these cross sections at resonant wavelengths yields the spectroscopic signature of exciting the LSPR.

The electromagnetic enhancement is easily calculated for particles much smaller than the wavelength of light, for the problem reduces to an electrostatic one. The field induced in a small particle by a uniform external electric field is uniform inside the particle, parallel to the applied field and of strength where $\varepsilon_1(\omega)$ is the

$$E_{in} = \left[1 + \left\{ \left(\frac{\varepsilon_1(\omega)}{\varepsilon_2} - 1 \right) A \right\}^{-1} \right] E_{out}$$

frequency dependent dielectric function of the metal, ε_2 is the dielectric constant of the surroundings, E_{in} and E_{out} refer to the fields inside and outside the particle, respectively. A is a depolarization factor that depends upon the particle geometry. For the particular case of the sphere, A=1/3 so that which is resonant for frequency

$$E_{out} = \frac{\varepsilon_1(\omega) - \varepsilon_2}{\varepsilon_1(\omega) + 2\varepsilon_2} E_{in}$$

where $\varepsilon_1(\omega) = -2\varepsilon_2$. Thus, excitation of this dipolar resonance creates extensive fields at the particle surface that, in effect, increase the laser power at the molecule. In addition to its effect on the incident field, the particle amplifies the scattered Raman field. The molecular oscillation drives the radiated sphere resonance. The extreme sensitivity of SERS to small increases in the local field is readily seen since it scales roughly as $|E_{\text{out}}|^4$.

The last statement is not quite correct, because the Raman scattering occurs at a shifted frequency from the incident light frequency. Including this fact, and containing the distance dependence of the enhanced field that is given by the dipole decay law, the complete enhancement factor for a sphere in the electrostatic (Rayleigh) limit. Where L and S represent to the laser and Stokes fields

$$G = \left[\frac{\varepsilon_1(\omega_{\text{L}}) - \varepsilon_2}{\varepsilon_1(\omega_{\text{L}}) + 2\varepsilon_2}\right]^2 \left[\frac{\varepsilon_1(\omega_{\text{s}}) - \varepsilon_2}{\varepsilon_1(\omega_{\text{s}}) + 2\varepsilon_2}\right]^2 \left(\frac{r}{r+d}\right)^{12}$$

respectively, r is the radius of sphere, and d is the molecule-surface distance.

This formula based on a very simple model describes important properties of electromagnetic enhancement of SERS and provides qualitative understanding of many of the experimental results. Resonance occurs when $\varepsilon_1 = -2\varepsilon_2$ at either the incident light frequency or the scattered frequency. If the vibrational frequency shift is small, both excitation and emission can be resonant simultaneously. At resonance, the enhancement order is the fourth power of the local field of the metal nanostructure. This relation explains why metals having high reflectivity are better enhancers. The distribution of molecular orientations and the variation of the electric field of the dipole over the surface of the sphere lead to large depolarization ratios. Electromagnetic enhancement of SERS does not need direct attach between metal and molecule but it strongly decreases with increasing distance demonstrated by the decay of the field of a dipole over the distance $(1/d)^3$ to the fourth power, resulting in $(1/d)^{12}$.

As the particle size increases beyond the Rayleigh boundary, the entire enhancement decreases. The physical reasons of this decrease are dynamic depolarization and radiation damping, the former to the partially destructive interferences between radiations emitted at different location of the larger particles, and the latter term referring to energy loss from the induced moment by emission of radiation. The effect of incident electromagnetic field on the combined colloidal metal particle and target molecule may simply be described as follow: In the first place, interaction between electromagnetic field and colloidal surface results in Rayleigh scattering a 2-photon process which involves the generation of surface

plasmon modes. Rayleigh scattering is an elastic process where a photon of identical frequency to that of the incident photon is forced out following the generation of a surface plasmon on the metal surface. In considering the effect of the incident radiation on the target molecule only, Raman scattering as an inelastic process is observed. In the case of normal Raman scattering, no metal particles are existing and the target molecule interacts directly with the incident electromagnetic field. In this case, the frequency of the incident and scattered photon are mismatched due to variations within the vibrational energy levels of the target molecule. Incident radiation interact with both the metal to create a surface plasmon and the target molecule where the vibrations in the energy levels of the molecule result in photon of unidentical frequency being returned to the metal and scattered. The combination of incident field and the vibrational energy of the molecule lead to enormously increased scattering power observed as SERS.

1.2.3. Chemical (CHEM) Mechanism

Similarly electromagnetic enhancement mechanism, chemical enhancement mechanism contributes substantially to enhance the SERS signal. In terms of 'chemical enhancement mechanism', it has been widely suggested that the target molecule must in some way, adsorb onto surface of the SERS substrate for the enhancement mechanisms to be applied. Several evidence suggest that the electromagnetic enhancement mechanism is not the only one effect that contributes to the enhancement.

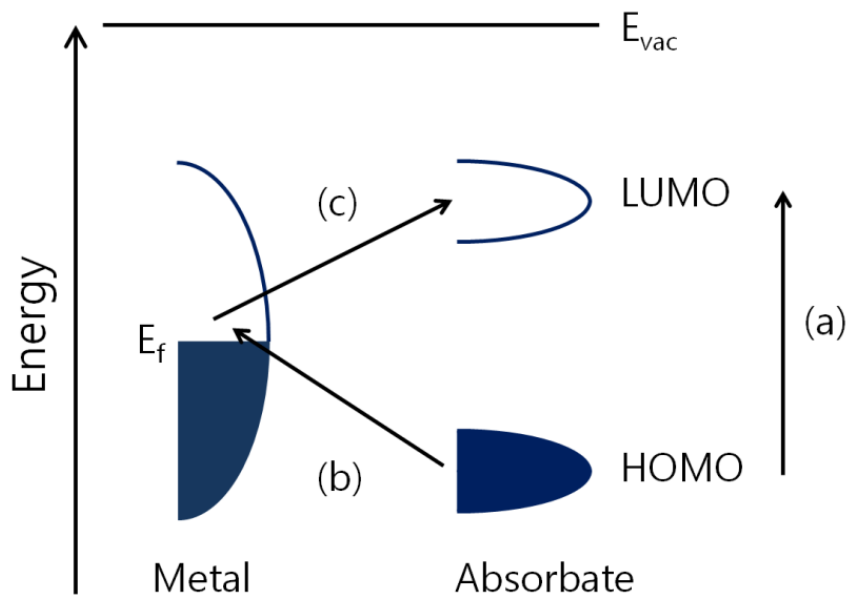

Figure 1.3. Energy level diagram for the system of a molecule adsorbed on a metal surface. The HOMO and LUMO are broadened into resonances by their interaction with the metal energy states; orbital occupancy depends on the Fermi energy. Possible charge transfer excitations are shown.

A possible enhancement mechanism is attributed to specific interactions, for example, formation of an adsorbate-surface complex and electronic coupling between molecule and metal. This complex form increases the Raman cross section of the adsorbed molecule compare with that of a free molecule. Other possible electronic SERS mechanisms involve a resonance Raman effect, which becomes operative due to a charge-transfer generated between the metal and adsorbate molecules. The existence of the charge-transfer state raises the probability of a

Raman transition by providing a route for resonant excitation. This mechanism is site-specific and analyte dependent. The molecule must be directly adsorbed to the roughened metal surface to undergo the chemical enhancement.

1.2.4. Selection Rules

Basically, the selection rules in SERS are the same as those for conventional Raman spectroscopy. In brief, a molecular vibrational mode is Raman-active only if it changes the polarizability $\boldsymbol{\alpha}$ of the molecule $(\partial\boldsymbol{\alpha}/\partial\mathbf{Q}) \neq 0$.[23] $\mathbf{Q}$ is the normal coordinate of the vibration. Selection rules are relaxed leading to the appearance of commonly forbidden Raman modes in the surface spectra. Furthermore, because the local field at the surface is highest in the direction perpendicular to the surface, vibrational modes involving changes in the adsorbate polarizability normal to the surface are firstly enhanced.[24] This plus the fact that the amplitude of the electromagnetic field falls off rapidly with distance from the surface allows one to determine the adsorbate orientation with respect to the average surface normal as well as the proximity of adsorbate functional groups to the surface.

1.3. Finite-Difference Time-Domain (FDTD) Method

1.3.1. Short Description

Finite-difference time-domain (FDTD) method is a computational electrodynamics modeling technique. It is easy to understand and implement in software. Since it is a time-domain method, solutions can cover a wide frequency range with a single simulation run.

The basic FDTD space grid and time-stepping algorithm trace back to a seminal 1966 paper by Kane Yee in IEEE Transactions on Antennas and Propagation.[25] The descriptor "Finite-difference time-domain" and its corresponding "FDTD" acronym were originated by Allen Taflove in a 1980 paper.[26] Since about 1990, FDTD techniques have emerged as primary means to computationally model many scientific and engineering problems dealing with electromagnetic wave interactions with material structures. As summarized by Taflove et. al.,[27] current FDTD modeling applications range from near-DC (ultralow-frequency geophysics involving the entire Earth-ionosphere waveguide) through microwaves (radar signature technology, antennas, wireless communications devices, digital interconnects, biomedical imaging/treatment) to visible light (photonic crystals, nanoplasmonics, solitons, and biophotonics).

The FDTD method belongs to the general class of grid-based differential time-domain numerical modeling methods. The time-dependent Maxwell's equations (in partial differential form) are discretized using central-difference approximations to the space and time partial derivatives. The resulting finite-

difference equations are solved in a leapfrog manner for electric and magnetic field: the electric field vector components in a volume of space are solved at a given instant in time, and then the magnetic field vector components in the same spatial volume are solved at the next instant in time. The processes are repeated over and over again until the desired transient or steady-state electromagnetic field behavior is fully evolved.

1.3.2. Principles

The FDTD method utilizes the central difference approximation to discretize the two Maxwell's curl equations, namely, Faraday's and Ampere's Laws, in both the time and spatial domains, and then solves the resulting equations numerically to derive the electric and magnetic field distributions at each time step using an explicit leapfrog scheme. The FDTD solution, thus derived, is second-order accurate, and is stable if the time step satisfies the Courant condition.

In Yee's scheme,[25] the computational domain is discretized by using a rectangular grid. The electric fields are located along the edges of the electric elements, while the magnetic fields are sampled at the centers of the electric element surfaces and are oriented normal to these surfaces, this being consistent with the duality property of the electric and magnetic fields in Maxwell's equations. A typical electric element is shown in Figure 1.4(a), and the relative location of the electric and magnetic elements is also displayed in Figure 1.4(b).

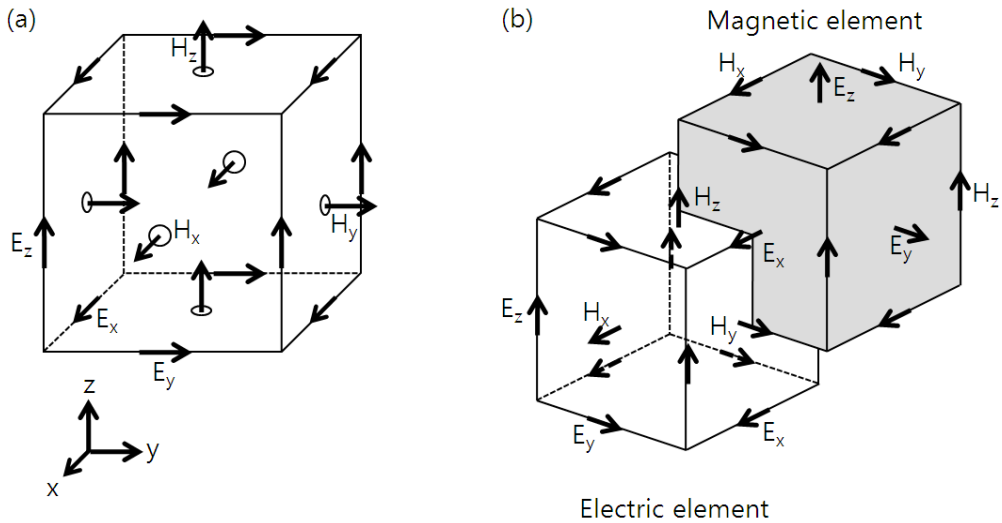

Figure 1.4. Position of the electric and magnetic fields in Yee's scheme. (a) Electric element (b) Relationship between the electric and magnetic elements.

The FDTD utilizes rectangular pulses as basic functions in both the time and spatial domains, implying that the electric field is uniformly distributed along the edge of electric element, while the distribution of magnetic fields is uniform on the surface of the electric element, In addition, in the time domain, the electric fields are sampled at times $n\Delta t$, and are assumed to be uniform in the time period of $(n-1/2\Delta t)$ to $(n+1/2\Delta t)$. Similarly, the magnetic fields are sampled at $(n+1/2\Delta t)$, and are assumed to be uniform in the time period of $n\Delta t$ to $(n+1)\Delta t$. The FDTD algorithm constructs a solution to the following two Maxwell's curl equations:

$$\nabla \times \vec{E} = -\mu \frac{\partial \vec{H}}{\partial t} - \sigma_M \vec{H} \qquad \text{(Faraday's Law)}$$

$$\nabla \times \vec{H} = \varepsilon \frac{\partial \vec{E}}{\partial t} - \sigma \vec{E} \qquad \text{(Ampere's Law)}$$

Chapter 2

: SERS of 4-Nitrobenznethiol and 4-Aminobenznethiol on Ag in Icy Environments at Liquid Nitrogen Temperature

2.1. Introduction

Photochemical reactions are typically classified as either direct or indirect. In direct photochemical reactions, the chemical of interest absorbs light.[28-34] Indirect photochemical reactions occur when a species other than the chemical of interest absorbs light and subsequently initiates a series of reactions transforming the target compound. Indirect photolysis can be induced by both organic and inorganic species. One example is the photolysis of 4-nitrobenzenethiol (4-NBT) on Ag under visible laser illumination.[35-39] The normal Raman (NR) spectrum of 4-NBT is invariant over time with an excitation wavelength of 514.5 nm, implying that 4-NBT itself is not involved in any direct photochemical reactions. However, unlike the NR spectrum, the surface-enhanced Raman scattering (SERS) spectrum was shown to be subject to change with time.[38,39] The SERS peaks of 4-NBT gradually lose their intensities, coupled with the appearance of a new set of peaks. The intensity of the new peaks rapidly increases, as a function of the laser-illumination time. The plasmonically generated hot electrons from the Ag substrate are the origin of this reaction.[40-47] The chemical structure of the reaction product is uncertain, though either 4-aminobenzenethiol (4-ABT) [48-53] or 4,4′-dimercaptoazobenzene (4,4′-DMAB) [54-57] has been proposed as the potential products.

The ambiguity of the photochemical reaction product from 4-NBT on Ag is associated with the SERS of 4-ABT. 4-ABT is an unusual molecule because its SERS spectrum depends on the type of SERS substrate and on the measurement conditions. While only totally symmetric vibrational bands are observed in the NR spectrum, the

SERS spectrum reveals several additional nonsymmetric lines.[50,52,53] A similar phenomenon was also observed for the analogs of 4-ABT.[58,59] The origin of these additional peaks has recently been debated, and many researchers believe that these peaks can be attributed either to the enhancement mechanism or to surface-catalyzed photolysis.[54,60,61] From the perspective of the enhancement mechanism, these SERS bands are attributed to the b_2-type bands of 4-ABT, which appear by the metal-to-adsorbate electronic charge transfer. Another point is that the bands could be the a_g modes of 4,4′-DMAB produced from 4-ABT as a result of catalytic coupling on metal nanostructures, as the two spectra are very similar.[60-66] If the b_2-type SERS peaks of 4-ABT were formed by the a_g modes of 4,4′-DMAB, then conversion of 4-NBT on Ag to 4,4′-DMAB would also be possible under laser light illumination at 514.5 nm.

Ice comprises a network of strong hydrogen bonds with one water molecule uniting with four other water molecules. The hydrogen bonds of water are very strong, and other molecules rarely penetrate the ice crystal lattice. Therefore, it is generally believed that ice suppresses chemical reactions. However, reactions in ice can occasionally proceed faster than in solution, which can be understood in terms of the microscopic freeze-concentration.[67,68] Polycrystalline ice is formed by the normal freezing method. When each crystal of polycrystalline ice grows, the unfrozen solution becomes confined within the space of several ice crystals. The concentration of the confined solution continually increases as the ice crystals continue to grow. As a result, the elevated reaction rate caused by the freeze-concentration can become greater than the reduced reaction rate caused by the

decrease in the temperature. Using this information, it was intended in this thesis to determine what would happen if 4-NBT and 4-ABT on Ag, were trapped between ice crystals and then illuminated using a visible laser with a wavelength of 514.5 nm. For conversion of 4-NBT to 4-ABT or 4,4′-DMAB, a N–O bond scission must take place. A photochemical reaction accompanying such a bond cleavage will be less likely to occur within an icy environment than under ambient conditions because 4-NBT or 4-ABT is already present in a close-packed structure.

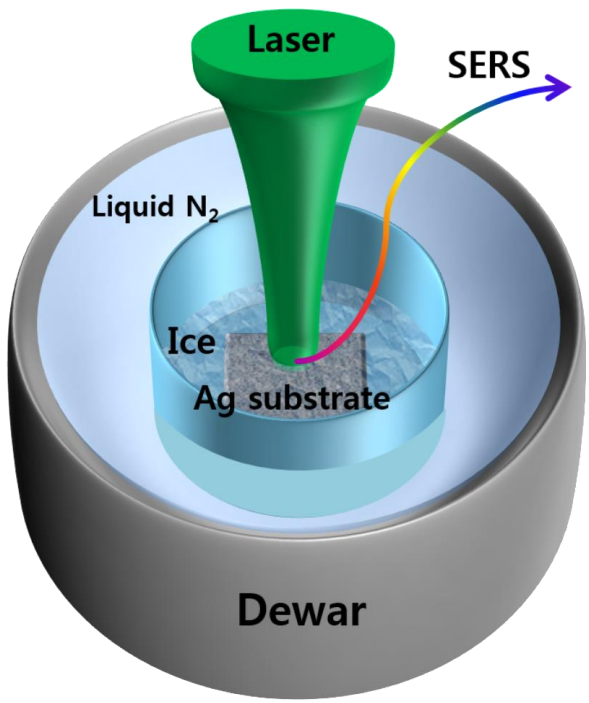

Scheme 2.1. Experimental arrangement for the measurement of SERS spectra of 4-NBT, 4-ABT, and Fe^{3+}-adsorbed cyanide on Ag in ice, performed at the temperature of liquid N_2 (77 K).

This thesis aimed to clarify the origin of the b_2-type bands appearing in the SERS of 4-NBT and 4-ABT. The first objective was to examine the b_2-type bands in the SERS spectra of 4-NBT and 4-ABT on Ag within icy environments. Using the SERS of cyanide, it was recently demonstrated that plasmonic generation of hot electrons is possible using nanostructured Ag substrates, even at the temperature of liquid N_2 (77 K).[69] Because the conversion of 4-NBT on Ag to 4-ABT or 4,4′-DMAB is a reductive process, the reaction will likely proceed even at 77 K if the reactant molecules have enough room to move around. However, if the reactant molecules are trapped between ice crystals, the reductive reaction requiring the N–O or N–H bond scission will not occur, even in the presence of hot electrons. In fact, when both the systems were trapped between ice crystals at 77 K, 4-NBT on Ag did not undergo a photoreaction, whereas 4-ABT on Ag still exhibited the b_2-type bands in its SERS spectrum. Thus, it was concluded that 4-ABT was responsible for the b_2-type bands, not 4,4′-DMAB. The formation of 4,4′-DMAB through the coupling of two different 4-ABT and/or 4-NBT molecules must not be feasible in icy environments at 77 K.

2.2. Experimental

Chemicals. The following chemicals were purchased from Sigma-Aldrich and used without further purification: silver nitrate ($AgNO_3$) 99.8%, branched poly(ethylenimine) (PEI, MW ~25 kDa), benzenethiol (BT) 99+%, 4-NBT 80%, 4-ABT 97%, sodium borohydride ($NaBH_4$) 99%, and potassium cyanide (KCN) 96%. All other chemicals were reagent grade or better and also used without purification. Aqueous solutions were prepared using deionized water (resistivity > 18.0 MΩ·cm) generated by a Millipore Milli-Q system.

Preparation of SERS-Active PEI-capped Ag film. At first, 1 mL of 2%-by mass aqueous solution of PEI was added to 100 mL of 10 mM aqueous solution of $AgNO_3$ and boiled for 15 min to produce the PEI-stabilized Ag nanoparticles.[70-72] The Ag nanoparticles produced were spherically shaped and their average size was determined to be 19 ± 9 nm by transmission electron microscopy (TEM) analysis. Thereafter, 2 mL of toluene was added to 5 mL of PEI-stabilized aqueous Ag sol. As 1.0 mL of BT was added further into the toluene phase, a highly homogeneous film of Ag nanoparticles formed at the toluene-water interface. Such Ag nanoparticle films could also be formed on a separate glass or mica by immersing the substrate in the mixture. BT was subsequently removed from the Ag film by treating with 0.1 M aqueous solution of borohydride for 30 min: the SERS activity of the Ag film remained even after the borohydride treatment.[72,73] The SERS active PEI-capped Ag film was finally washed with ethanol and dried under nitrogen.

Instrumentation. TEM images of Ag nanoparticles were obtained using a JEM-200CX transmission electron microscope operating at 200 kV. Raman spectra were measured using a Renishaw Raman system model 2000 spectrometer, equipped with excitation lines at 514.5 nm (20 mW Ar^+ laser, Melles-Griot model 351MA520), 488 and 560 nm (20 mW Ar^+/Kr^+ laser, Melles-Griot model 35KAP431), and 632.8 nm (17 mW He/Ne laser, Spectra Physics model 127). Raman scattering was recorded with 180° geometry using a Peltier-cooled CCD detector (400 × 600 pixels). A Raman band of a silicon wafer at 520 cm^{-1} was used as the reference to calibrate the spectrometer.

2.3. Results and Discussion

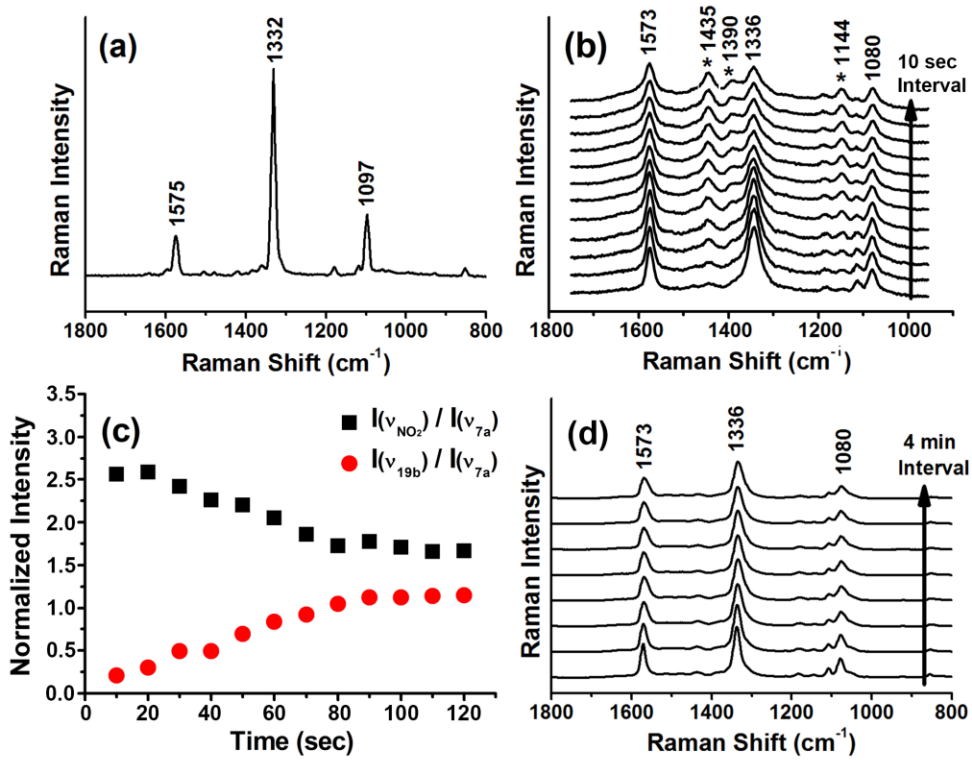

Figure 2.1. (a) NR spectrum of neat 4-NBT and (b, d) SERS spectra of 4-NBT on Ag obtained (b) under ambient conditions and (d) in icy environments at 77 K. Changes are plotted against time at 514.5 nm. (c) Relative peak intensities of the $\nu_s(NO_2)$ band at 1336 cm^{-1} and of the 19b band at 1435 cm^{-1} compared to the 7a band at 1080 cm^{-1}, i.e. $I(\nu_s(NO_2))/I(\nu_{7a})$ and $I(\nu_{19b})/I(\nu_{7a})$ in (b). See text for details.

The NR spectrum of neat 4-NBT obtained using 514.5 nm radiation is presented in Figure 2.1(a). Three distinct peaks were observed, at 1332 cm^{-1}, 1575 cm^{-1}, and 1097 cm^{-1}. These peaks are from the symmetric stretching vibration of the nitro group, the C–C stretching vibration, and the in-plane C–H bending vibration, respectively.[74] Figure 2.1(b) displays a series of SERS spectra of 4-NBT on a silver substrate obtained as a function of time upon exposure to 514.5 nm radiation. It can be seen that the $\nu_s(NO_2)$ peak at 1336 cm^{-1} gradually decreased with an increase in the irradiation time, with the emergence of new peaks at 1435, 1390, and 1144 cm^{-1} (see the relative peak intensities plotted against time in Figure 2.1(c)). The new peaks cannot be assigned to 4-NBT, implying that 4-NBT underwent a photoreaction on Ag. The reaction product was presumed to be 4-ABT, as discussed later.

The NR spectrum of neat 4-ABT and its SERS spectrum on Ag are shown in Figures 2.2(a) and (b), respectively, using 514.5 nm radiation. The two strong peaks observed in the NR spectrum, at 1086 and 1592 cm^{-1}, are identified as the C–S and C–C stretching vibrations, respectively (a_1 vibration modes).[48] In the SERS spectrum, the enhanced peaks of controversial origin are observed around 1435, 1390, and 1144 cm^{-1}. As stated, the purpose of this work was to determine whether they are formed by 4-ABT, or are from the products of photoreaction such as 4,4′-DMAB. It is notable that the new peaks observed in 4-NBT (Figure 2.1(b)) are similar to those of 4-ABT (Figure 2.2(b)). This implies that 4-NBT on Ag is photo-reduced to 4-ABT; however, it is still unclear whether 4-ABT on Ag is subsequently photo-oxidized to 4,4′-DMAB.

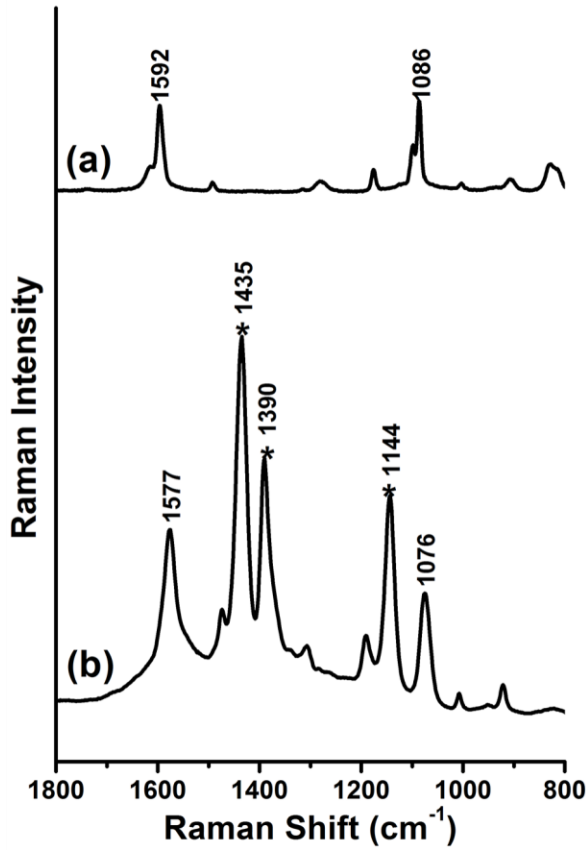

Figure 2.2. (a) NR spectrum of neat 4-ABT and (b) its SERS spectrum on Ag, with an excitation source of 514.5 nm; b_2-type bands are starred in (b).

The SERS spectra of 4-NBT and 4-ABT on Ag shown in Figures 2.1(b) and 2(b), respectively, were all obtained under ambient conditions. We also attempted to obtain the SERS spectra when 4-NBT and 4-ABT on Ag were trapped between ice crystals at 77 K (liquid N_2 temperature; refer to Scheme 2.1 for configuration of the experiment). In Figure 2.1(d), the SERS spectra of 4-NBT on Ag in icy conditions are shown. The SERS spectra were invariant over time, and correlated well with the NR spectrum of 4-NBT (Figure 2.1(a)). Some peaks from photoproduct(s) seen in

Figure 2.1(b) were not detected in the SERS spectra (Figure 2.1(d)). This result confirmed that 4-NBT on Ag, if buried within ice crystals, could not be converted to 4-ABT. One may argue that this observation was due to hot electrons not being efficiently generated from Ag at 77 K and/or the N–O bonds could not be broken within the icy environment. However, it was recently demonstrated that hot electrons are efficiently generated, even in icy environments, from Ag nanostructures by exposure to visible laser at 514.5 nm.[69] The difficulty of the photo-reduction of 4-NBT on Ag in icy environments must then be because the N–O bonds cannot be broken owing to the small spaces between the ice crystals. If so, 4-ABT on Ag will not be subject to a photoreaction in icy environments because much more space is definitely needed between the ice crystals than the N–O bond breaking in order to produce bimolecular products, such as 4,4′-DMAB, from 4-ABT by photo-dimerization: the volume required for the reaction must be larger than the size of the ice cavities.

There are two mechanisms operative in SERS, one is an electromagnetic enhancement mechanism and the other is a chemical enhancement mechanism.[16,75,76] It is well-known that at least 8~10 orders of enhancement can arise from electromagnetic surface plasmon excitation. On the other hand, the chemical enhancement is associated with either the metal-to-molecule or the molecule-to-metal charge-transfer transition, necessitating chemical bonding between the molecules and the SERS substrate, while not in electromagnetic theory, and has long been regarded as a source of one or two orders of enhancement. Lombardi and Birke have shown recently by expressing the SERS signal as a product of three

contributions, i.e. the surface plasmon resonance, the metal-to-molecule charge-transfer resonance, and a molecular resonance, that the charge-transfer contribution could dominate the SERS spectrum.[77] The plasmonically generated hot electrons must be associated with the charge-transfer chemical enhancement.[69] We may have to admit, however, that when the energy of hot electrons is not enough to reach the lowest unoccupied molecular orbital (LUMO) of the adsorbate, the charge-transfer chemical enhancement will be negligible. In this work, we just witnessed from the SERS of 4-NBT that the hot electrons can also participate in the reduction of the adsorbate at least in ambient conditions.

The SERS spectra of 4-ABT on Ag within the icy environment is presented in Figure 2.3(a), plotted against time with illumination at 514.5 nm. We noticed that the b_2-type bands appeared at 1435, 1390, and 1144 cm^{-1} even in the icy environments (see the starred peaks). The SERS spectral pattern observed in icy environments (in Figure 2.3(a)) was identical to that observed under ambient conditions (in Figure 2.2(b)). Thus, we conclude that the b_2-type bands are not related to the formation of azo molecules, such as 4,4′-DMAB. Those bands must be originated from the presence of 4-ABT. This also implies that 4-NBT on Ag can be photo-reduced to 4-ABT but not to 4,4′-DMAB. The appearance of the b_2-type bands is presumably associated with the hot electrons which are plasmonically generated from the Ag substrate. One can imagine that the efficiency of the generation of hot electrons depends on the excitation wavelength. Recently, it was observed from the Fe^{3+}-adsorbed cyanide on Ag (Fe^{3+}/NC/Ag) system that Fe^{3+} to Fe^{2+} conversion is more facile for excitation performed at shorter wavelengths.[69]

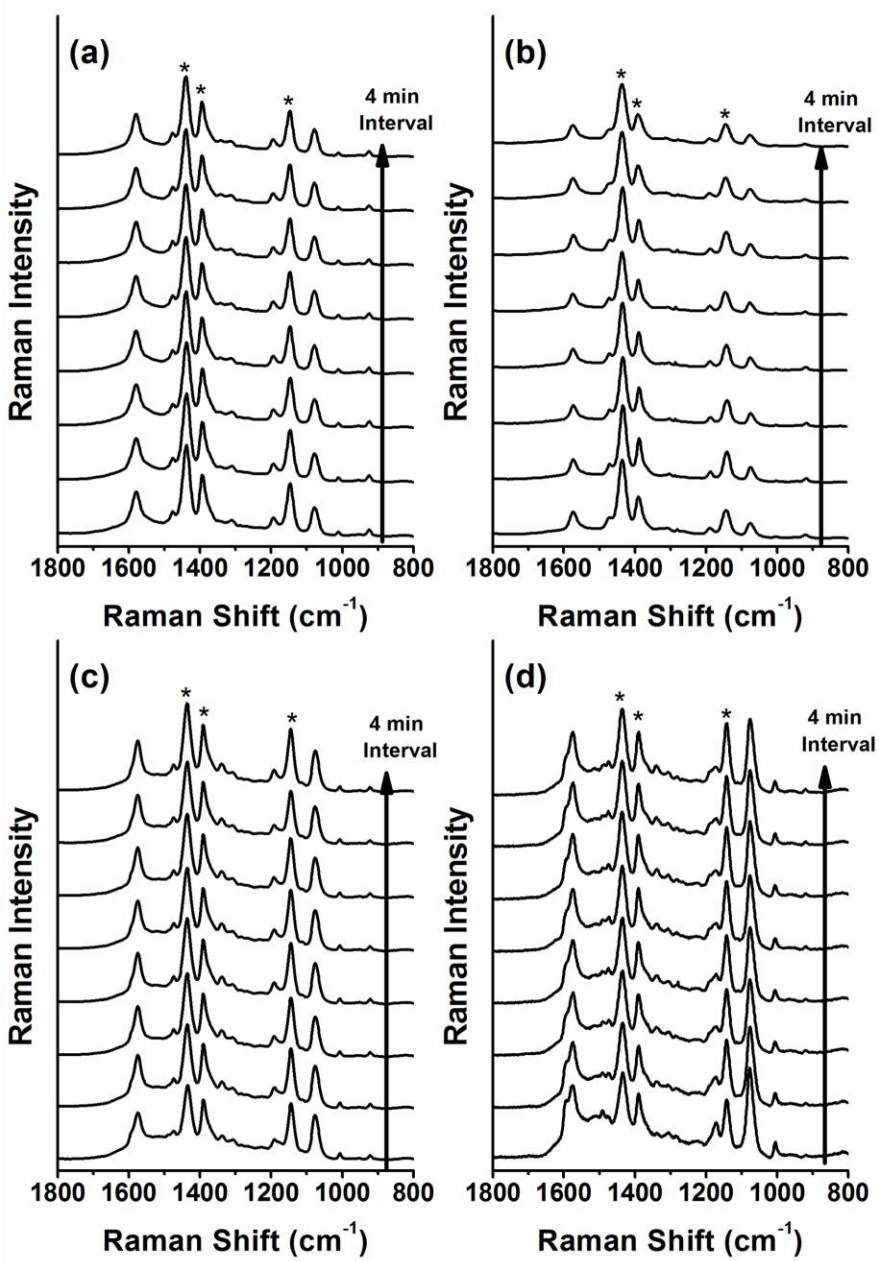

Figure 2.3. Series of SERS spectra of 4-ABT on Ag measured in icy environments plotted against time, under illuminations of (a) 514.5, (b) 488, (c) 568, and (d) 632.8 nm radiation; b_2-type bands are starred in the figures.

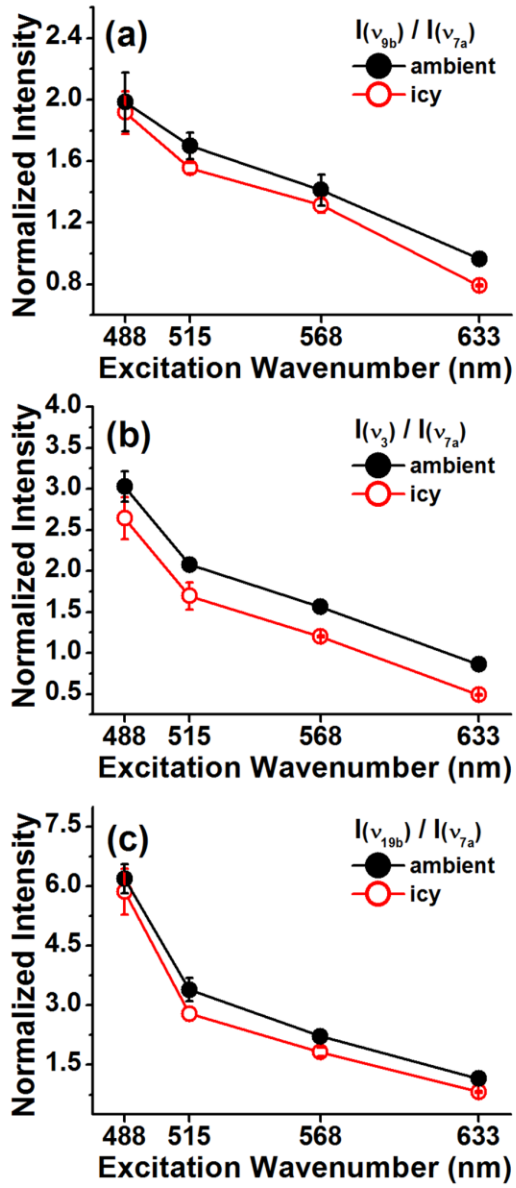

Figure 2.4. Relative peak intensities of the (a) 9b, (b) 3, and (c) 19b bands of 4-ABT on Ag compared to the 7a band, i.e. $I(\nu_{9b})/I(\nu_{7a})$, $I(\nu_3)/I(\nu_{7a})$, and $I(\nu_{19b})/I(\nu_{7a})$, measured under ambient conditions (filled circles) and in icy environments (open circles); plotted against excitation wavelengths. Error bars indicate the average and standard deviation from the experiments performed in triplicate.

The SERS spectra for 4-ABT on Ag in icy environments at 77 K, measured with exposure to 488, 568, and 632.8 nm radiations, can be observed in Figures 2.3(b), (c), and (d), respectively. Normalization of the peak intensities in Figure 2.3 was carried out with the use of a silicon wafer standard. Notably, the b_2-type bands were present in all the spectra presented in Figure 2.3. Evidently, the b_2-type bands appeared to be more intense when the excitation occurred at shorter wavelengths. This would imply that the appearance of the b_2-type bands was strongly correlated to the hot electrons generated from Ag.

Although not shown here, the SERS spectra of 4-ABT on Ag was also measured at room temperature with excitation at 488, 568, and 632.8 nm. The SERS spectral patterns observed at room temperature were the same as those in icy environments. The intensity ratio of the b_2-type band to the a_1-type band was evaluated in terms of the excitation wavelength for the SERS spectra measured at room temperature and SERS spectra measured in icy environments at 77 K. Assigning the b_2-type bands at 1144, 1390, and 1435 cm^{-1} in Figure 2.3 to the 9b, 3, and 19b bands of 4-ABT, respectively, it was observed that all b_2 bands increased in intensity with respect to the 7a band at 1080 cm^{-1} with a decrease in the excitation wavelength, as shown in Figure 2.4. There is also no temperature dependence. These results clearly indicate equal involvement of the chemical enhancement mechanism in all of the observed Raman spectra (Figure 2.3). Otherwise, there would be no reason for the b_2 bands to have varied intensity relative to the a_1 bands, as a function of the excitation wavelength.

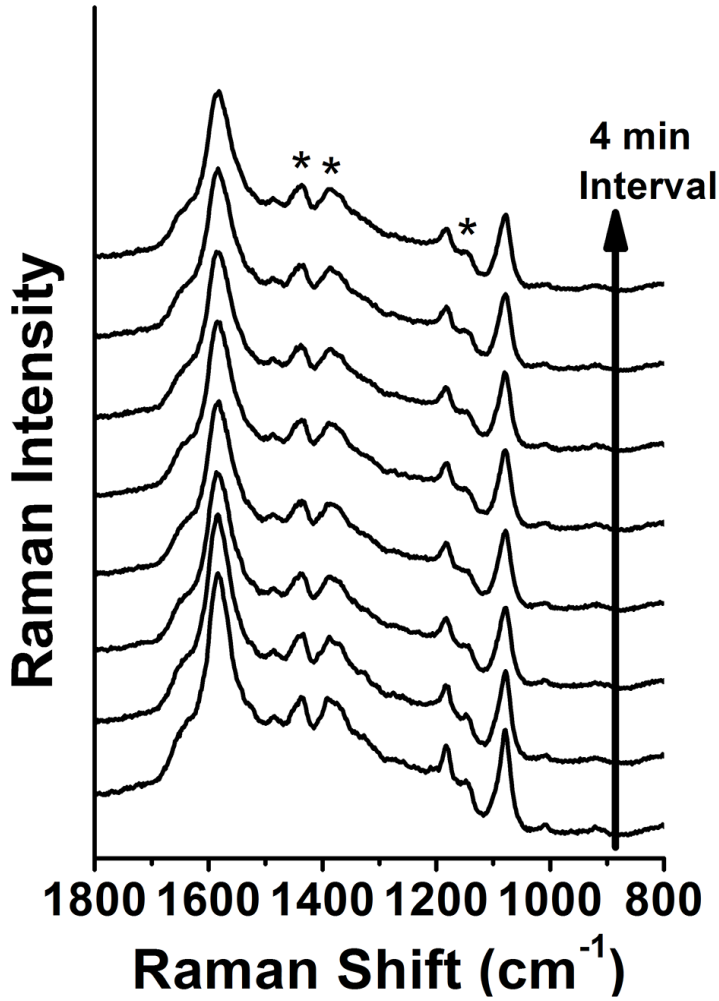

Figure 2.5. Series of SERS spectra of 4-ABT on Ag obtained after cooling a surrounding acidic solution (pH 3) down to 77 K using an excitation source of 514.5 nm; b_2-type bands are starred in the figure.

It was recently demonstrated that pH of the solution had a strong influence

on the b_2-type bands of 4-ABT.[78] In fact, the b_2-type bands were either weak or not present at acidic pH, without relation to wavelength or type of SERS substrate used, though the bands were very distinctively present at basic pH. For 4,4′-DMAB, no dependence on pH was found in the SERS spectra. From the pH-dependent UV-vis absorption spectra and ab initio quantum mechanical calculations, it was determined that the weakness of the b_2-type bands observed at acidic pH could be related to an upshift of the LUMO level of 4-ABT, as a result of protonation of the amine group. Figure 2.5 shows the SERS spectra obtained for 4-ABT on Ag after cooling an acidic solution (pH 3) (wetting 4-ABT) down to 77 K. As expected, very weak b_2-type bands were present at the icy conditions (see the starred peaks). This compares well with their strong appearance at neutral pH (Figure 2.3(a)). Though not shown here, the b_2-type bands in the basic ice were as strong as those in the neutral ice. Evidently, chemical enhancement due to charge transfer resonance is not as likely to take place at acidic conditions.

2.4. Summary and Conclusion

In the SERS spectrum of 4-NBT on Ag under ambient conditions, a few peaks which were not assignable to 4-NBT appeared. These peaks were also identified at the same positions in the SERS spectrum of 4-ABT on Ag. The origin of these peaks has been recently debated because their counterparts are not present in the NR spectra of 4-ABT and 4-NBT. One hypothesis was that these bands are the b_2-type bands of 4-ABT, appearing because of the metal-to-adsorbate electronic charge transfer. Another hypothesis was that the bands are formed by the a_g modes of 4,4′-DMAB, which is produced from 4-ABT (as well as 4-NBT) via catalytic coupling on metal nanostructures. In this work, it was confirmed that these bands do not appear in the SERS of 4-NBT on Ag in icy environments at 77 K. That is, the photo-reduction of the nitro group did not take place in icy environments. Hot electrons that might take part in the reduction of the nitro group were generated plasmonically from the Ag substrate even in icy environments, demonstrating that the infeasibility of the photo-reduction of 4-NBT on Ag in icy environments was attributed to the small spaces between the ice crystals. It is difficult to break the N–O bond under such extreme conditions. A similar situation occurred for 4-ABT on Ag in icy environments. However, in case of 4-ABT on Ag, the b_2-type bands were observed even in icy environments. Thus, it was conclude that the b_2-type bands are formed by 4-ABT, and have nothing to do with the formation of azo compounds such as 4,4′-DMAB. The appearance of the b_2-type bands is clearly the result of hot electrons plasmonically generated from the Ag substrate. The movement of hot electrons from

Ag to 4-ABT is related to the charge-transfer chemical enhancement mechanism in SERS. Since hot electrons are generated more easily at shorter excitation wavelengths, the b_2-type bands become more distinct as the excitation wavelength decreases.

Chapter 3

: Enhanced Raman Scattering in Gaps Formed by Planar Au and Au/Ag Alloy Nanoparticles

3.1. Introduction

SERS can be induced to occur even on the surfaces of SERS-inactive substrates by using Ag or Au nanoparticles. For instance, it is difficult to observe the Raman peaks of 4-aminobenzenethiol (4-ABT) adsorbed on a platinum substrate, but attaching Ag nanoparticles onto the pendent amino group of 4-ABT, we can observe the Raman peaks distinctly. This is possibly owing to the electromagnetic coupling of the localized surface plasmon (LSP) of the Ag nanoparticles with the surface plasmon polariton (SPP) of the platinum substrate, leading to a noticeable enhancement of the electromagnetic field at the gaps.[79-81] In addition to the coupling interaction between the LSP of a nanoparticle and the SPP of a flat substrate, there is an interaction between the nanoparticle with its image in an infinite metallic substrate, which is similar to a nanoparticle dimer in many aspects. Therefore, a nanogap formed by a planar substrate and a spherical nanoparticle, where the SERS-active molecules are sandwiched between the planar substrate and the spherical nanoparticle, is an ideal geometry for SERS study.

Over the decades, metal alloy nanoparticles have attracted great attention because their changeable compositions lead to their unique size-dependent electronic, optical, and catalytic characteristics, which are different from those of the corresponding individual metal particles.[82-88] For example, gold-containing bimetallic nanoparticles show enhanced catalytic activity.[89] Ag-Au alloy nanoparticles are more catalytically active than monometallic nanoparticles, Ag or Au nanoparticles, in the oxidation of CO at low temperatures.[90] Au alloys have been

utilized as a Pt replacement for oxygen reduction in proton exchange membrane (PEM) fuel cells,[91] and colloidal Au-Ag alloys have shown an enhanced electrocatalytic activity in direct borohydride fuel cells.[92] In addition, the surface plasmon properties of Au-Ag alloy nanoparticles are continuously tunable because of the possibility of composition changes, whereas monometallic Ag and Au nanoparticles have relatively unchanging optical properties.[93-95]

In this thesis, firstly, it was examined the SERS inducing activity of Ag nanoparticles themselves more precisely, as the outmost surfaces of Au-Ag alloy nanoparticles are highly enriched with Ag atoms. In fact, we have previously compared the SERS inducing capability of Ag and Au nanoparticles by fabricating a nanogap system, comprised of 4-ABT sandwiched between a macroscopically smooth Au substrate and Ag and Au nanoparticles, labeled as Ag(Au)@4-ABT/Au(flat).[96,97] When 55-nm sized Ag and Au nanoparticles were used, intense Raman spectra were obtained in both cases using a laser light at wavelengths 632.8 > 568 > 514.5 nm.[96] A careful examination indicated that the spectrum induced by Ag nanoparticles was more intense than that by Au nanoparticles. Although a measurable Raman signal was obtained at all excitations when using Ag nanoparticles, a meaningful signal was only obtained at 632.8 nm excitation when using Au nanoparticles. On the other hand, a separate size-dependent study on Au showed that a more intense Raman signal is obtained with increasing size of the Au nanoparticles, at least for dimensions of under ~100 nm. Much the same trend was confirmed from 3D-FDTD calculation.

It is our experience that at least at a fixed excitation wavelength, an even

more intense Raman signal is obtained for Ag with increasing size of nanoparticles. It is uncertain, however, whether the excitation wavelength dependence would be similar to the case of Au nanoparticles or opposite, or whether a maximum signal would be observable at the 568 nm excitation. A possible complication is associated with the fact that the surface plasmon resonance of Ag nanoparticles is located at far below 514.5 nm so that the excitation wavelength dependence of Ag nanoparticles might be quite different from that of Au nanoparticles. For this reason, in this thesis we prepared four differently sized spherical Ag nanoparticles, i.e. 20-, 40-, 60-, and 80-nm in diameter, and examined the effects of size of nanoparticles and the excitation wavelength by manufacturing a nanogap electrode using planar Au as the bottom substrate and 4-ABT as the probe molecule. The SERS induction characteristics of Ag nanoparticles in a nanogap mode are found to differ from those of Au nanoparticles. For the case of certain sized Ag, a higher EF was observed at 568 nm excitation rather than at 514.5 or 632.8 nm excitation. We learned that both the size of metal nanoparticles and the laser excitation wavelength have to be optimized properly in order to induce SERS by means of a nanogap mode.

The next step would be to investigate how the nano gap characteristics are affected by the presence of Au/Ag alloy nanoparticles. Over the decades, metal alloy nanoparticles have attracted great attention because their changeable compositions lead to their unique size-dependent electronic, optical, and catalytic characteristics, which are different from those of the corresponding individual metal particles.[82,83] For example, gold-containing bimetallic nanoparticles show enhanced catalytic activity.[89] Ag-Au alloy nanoparticles are more catalytically active than monometallic

nanoparticles, Ag or Au nanoparticles, in the oxidation of CO at low temperatures.[90] Au alloys have been utilized as a Pt replacement for oxygen reduction in proton exchange membrane (PEM) fuel cells,[91] and colloidal Au-Ag alloys have shown an enhanced electrocatalytic activity in direct borohydride fuel cells.[92] In addition, the surface plasmon properties of Au-Ag alloy nanoparticles are continuously tunable because of the possibility of composition changes, whereas monometallic Ag and Au nanoparticles have relatively unchanging optical properties.[93-95]

Indeed, this work is particularly relevant because it was discovered recently that the surface characteristics of citrate-reduced Au/Ag alloy nanoparticles were similar to those of pure Ag nanoparticles.[98] For Au/Ag alloy nanoparticles, the positions of the surface plasmon resonance (SPR) absorption peaks are known to vary linearly as a function of the bulk concentration of Au or Ag atoms, which implies that the SPR absorption characteristics are determined mainly by the bulk composition of alloy nanoparticles. In this context, when Au/Ag nanoparticles are interacting electromagnetically with a planar Au substrate, the outermost surface composition of alloy nanoparticles may not be important. The chemical interaction associated with chemical enhancement should, however, be affected by the surface composition of alloy nanoparticles. The validity of these hypotheses is thus examined by observing the Raman spectra of 1,4-phenylenediisocyanide (1,4-PDI) and 4-aminobenzenethiol (4-ABT), which are both positioned in the nanogaps formed by Au/Ag alloy nanoparticles and a flat Au substrate. 1,4-PDI was selected because the Au-binding of the isocyanide group is different from the Ag-binding site,[99,100] whereas 4-ABT is a prototypical molecule exhibiting SERS peaks

associated with chemical enhancement, as described in chapter 2.[51,52,78,91,101-104] To help interpret the experimental results, the characteristics of the nanogap were simulated using the 3-D FDTD method.[105,106]

3.2. Experimental

Chemicals. Silver nitrate ($AgNO_3$, 99+%), hydrogen chloroaurate ($HAuCl_4$, 99.99%), trisodium citrate ($C_6H_5Na_3O_7 \cdot 2H_2O$, 99.9%), 1,4-PDI, and 4-ABT were purchased from Aldrich Co. and used as received. Other chemicals, unless specified otherwise, were of reagent grade, and highly pure water with resistivity greater than 18.0 MΩ·cm was used throughout.

Preparation of Ag, Au, Au/Ag alloy sols. Pure Au sol and Au/Ag alloy sol were prepared by following the recipes of Link et al.[107] To prepare pure Au sol, 95 mL of aqueous $HAuCl_4$ solution containing 5 mg of Au was brought to a boil, 5 mL of 1% sodium citrate was then added with vigorous stirring, and boiling was continued for ~30 min. To prepare the 1:1 Au/Ag ($Au_{0.5}Ag_{0.5}$) alloy sol and the sol containing 5 mole percent of Ag atoms ($Au_{0.95}Ag_{0.05}$), a predetermined number of moles of Au atoms was substituted with the equivalent number of moles of Ag atoms in the form of silver nitrate, $AgNO_3$. Ag sol was prepared by following the recipes of Lee and Meisel.[108] Specifically, depending on the size of nanoparticles to be formed, a different amount of trisodium citrate solution (1% w/v) was added into the boiling $AgNO_3$ (100 mL, 1 mM) solution with vigorous stirring. After boiling for an hour, the mixture was allowed to cool while still being stirred.

Preparation of smooth Au substrate. A macroscopically smooth Au substrate was prepared by resistive evaporation of titanium and Au at 1×10^{-6} Torr onto a cleaned glass slides. After deposition of approximately 200 nm of Au, the evaporator was back-filled with nitrogen. The Au substrate was subsequently

immersed in 20 mM 1,4-PDI (or 4-ABT) in ethanol for 1 h. To adsorb Au (or Ag or Au/Ag alloy) nanoparticles onto the pendent NC (or NH_2) groups, the 1,4-PDI (or 4-ABT)-adsorbed Au substrate was soaked in Au (or Ag or Au/Ag alloy) sol for a predetermined period of time. Metal (Au or Ag or Au/Ag alloy) nanoparticles (NP) are then bound to the pendent NC (or NH_2) group such that 1,4-PDI (or 4-ABT) is situated in the gaps between planar Au and nanosized metal particles; hereafter, the system will be denoted by NP@1,4-PDI/Au (or NP@1,4-PDI/Au). The number of metal nanoparticles adsorbed on 1,4-PDI on Au (1,4-PDI/Au) or 4-ABT on Au (4-ABT/Au) was counted using FE-SEM images. While obtaining the Raman spectra, the substrates were rotated at 3000 rpm to average out any inhomogeneous distribution of metal nanoparticles.

Instrumentation. UV-visible (UV/vis) spectra were obtained with a SCINCO S-4100 spectrometer. FE-SEM images were obtained with a JSM-6700F field emission scanning electron microscope operating at 5.0 kV. Energy-dispersive X-ray (EDX) analyses were taken from a CM20 transmission electron microscope at 200 kV. Raman spectra were obtained using a Renishaw Raman system Model 2000 spectrometer equipped with an integral microscope (Olympus BH2-UMA). The The 488 and 514.5-nm line from a 20 mW Ar^+ laser (Melles-Griot Model 351MA520) or the 568-nm line from a 20 mW Ar^+/Kr^+ laser (Melles-Griot Model 35KAP431) or the 632.8-nm line from a 17 mW He/Ne laser (Spectra Physics Model 127) were used as the excitation source. Raman scattering was detected using 180° geometry with a Peltier cooled (-70 °C) charged-coupled device (CCD) camera (400 × 600 pixels). The Raman peak of a silicon wafer at 520 cm^{-1} was used to calibrate

the spectrometer, whereas its intensity was used in spectral normalization. The data acquisition time was usually 90 s.

FDTD simulation. 3D-FDTD electrodynamics simulation[105,106] was carried out using the FDTD SOLUTIONS software (version 7.0.1) provided by Lumerical Solutions, Inc. A nanostructure composed of a Au (or Au/Ag or Ag) nanoparticle and a flat Au surface was modeled as a single metal sphere (35 nm) laid on a cuboid Au substrate with dimensions of 400 nm × 400 nm × 150 nm. The dielectric constants of Au and Ag were taken from the report of Palik[109] and those of Au/Ag alloy nanoparticles were given by the composition-weighted average of Au and Ag.[110,111] The dielectric film between the sphere and the cuboid was fixed to be 1 nm, and the refractive index of it was taken to be constant at 1.5.[112-115] Different mesh sizes were used for each calculation. Small mesh size (0.25 nm) was employed at the gap site between the sphere and the cuboid, while the mesh grid size of 1 nm was adopted around the surrounding region. Such nonuniform meshes can make 3D-FDTD calculations more accurate, while requiring less memory and computation time than comparable uniform meshes. The propagation direction of a plane wave was chosen to be along the x-axis (parallel to the surface of the cuboid) and the electric field was assumed to be polarized along the z-axis (perpendicular to the surface of the cuboid). Boundary conditions were imposed using the perfectly matched layer method. After the computation of the local electric field, the field intensity was evaluated for each mesh by integration and finally compared with the EF values estimated from the measured Raman spectra.

3.3. Results and Discussion

3.3.1 SERS of 4-ABT sandwiched between flat Au and Ag nanoparticles: Effects of size of Ag nanoparticles and the excitation wavelength

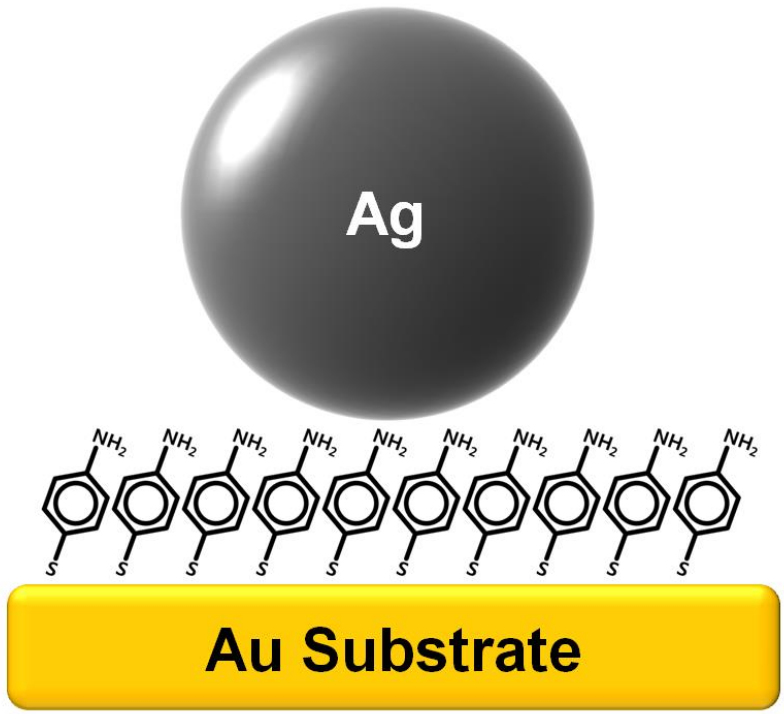

Scheme 3.1. Schematic diagram of a nanogap, formed by a planar Au substrate and a spherical Ag nanoparticle (20-, 40-, 60-, and 80-nm in diameter), in which a probe molecule, 4-aminobenzenethiol, is bound via thiolate sulfur and amine group to Au and Ag, respectively.

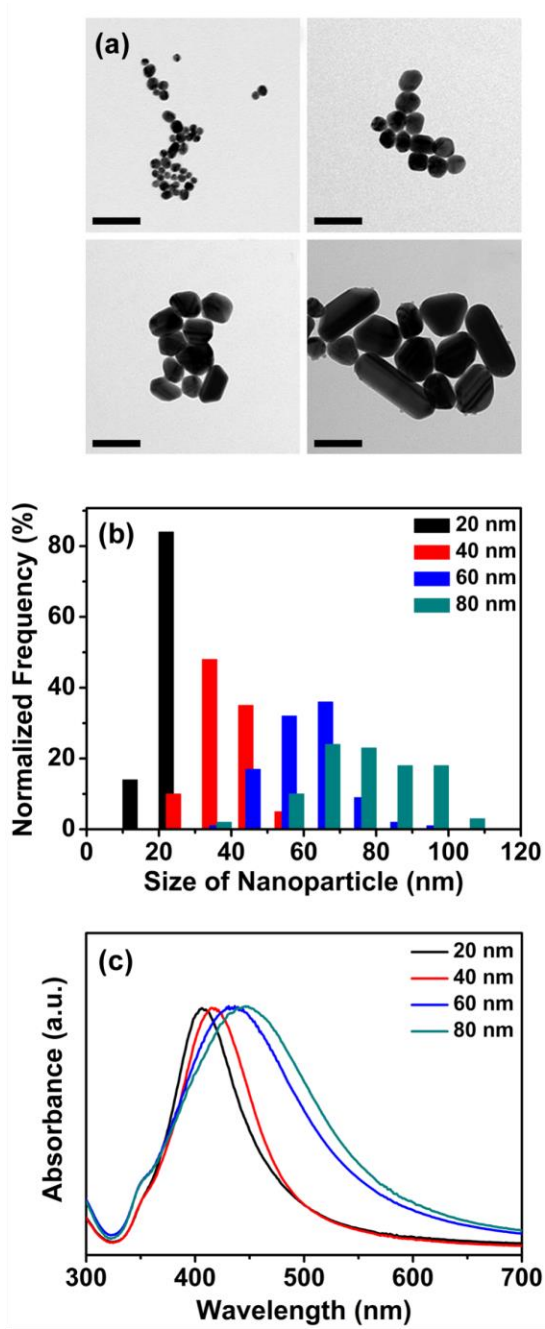

Figure 3.1. (a) TEM images of four different Ag nanoparticles prepared in this work (scale bar = 100 nm), (b) their histograms of size distribution, and (c) their UV/vis absorption spectra in colloid state.

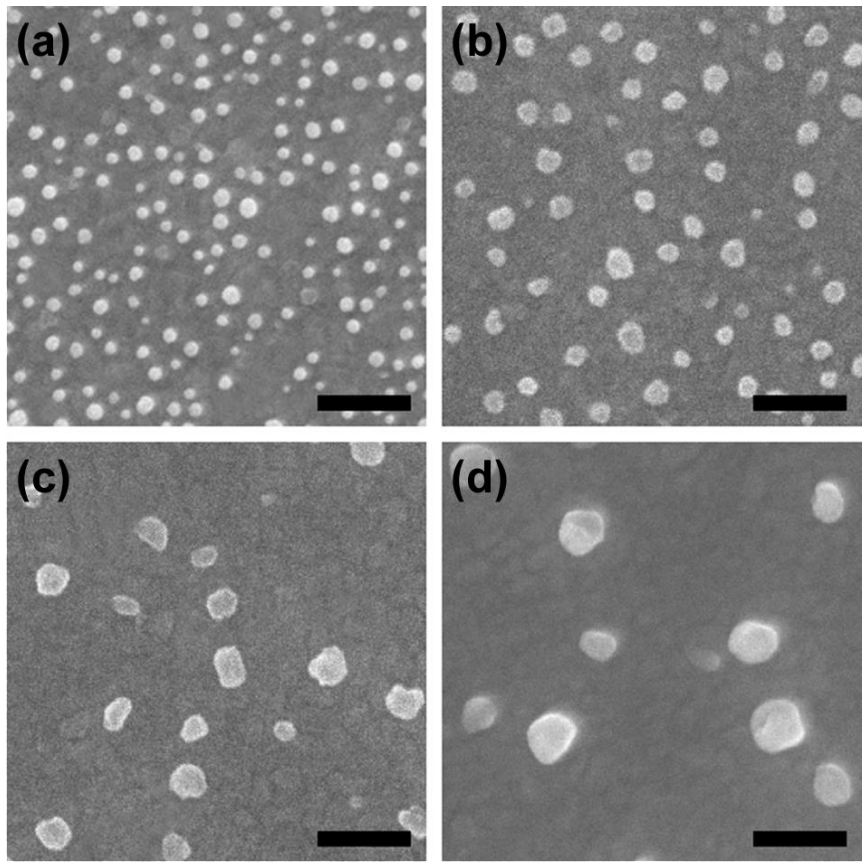

Figure 3.2. FE-SEM images of Ag@4-ABT/Au measured after soaking in Ag sol, comprised of (a) 20-, (b) 40-, (c) 60-, and (d) 80-nm sized Ag particles, for 1 h (scale bar = 200 nm).

Figure 3.1(a) shows the TEM images of four different Ag sol particles prepared in this work. Most of the nanoparticles were spherical shape, but the number of rod-shaped and/or truncated particles clearly increased along with the size of Ag nanoparticles. According to the histograms shown in Figure 3.1(b), the mean

diameters of the four different Ag nanoparticles were determined to be 23.0 ± 3.1, 38.8 ± 6.0, 59.4 ± 9.9, and 75.6 ± 13.3 nm, respectively: For simplicity, hereafter we will let their sizes be 20-, 40-, 60-, and 80-nm, respectively. As shown in Figure 3.1(c), these Ag particles exhibited very distinct surface plasmon absorption bands, from smaller to larger particles, at 406, 416, 434, and 446 nm, respectively: They are all well separated from the Raman laser wavelengths used in this work.

Due to the electrostatic repulsion of negatively charged Ag nanoparticles,[116] we did not expect the surface coverage of Ag nanoparticles adsorbed onto the pendent NH_2 groups of 4-ABT on a flat Au substrate to be large. Furthermore, since the concentrations of larger Ag nanoparticle sols are lower than those of smaller ones, fewer particles will adsorb onto the amine groups of 4-ABT. This could be evidenced from the FE-SEM images shown in Figure 3.2 that were taken after soaking the 4-ABT/Au(flat) substrates in Ag sol for 1h. In fact, the average number of Ag nanoparticles is determined to be 108, 70, 18, and 8 particles/μm^2, respectively, for the 4-ABT/Au substrates adsorbed with 20-, 40-, 60-, and 80-nm sized Ag nanoparticles. The surface coverage is at most 10.5%. The Ag nanoparticles are thus separated by at least 80 nm. No SERS peaks would then be significantly affected by the mutual interaction of Ag nanoparticles.

As usual, for a better interpretation of the SERS spectra we obtained the normal Raman (NR) spectra of 4-ABT in its neat and anionic states using 514.5, 568, and 632.8 nm radiation as the excitation sources. The peak intensities, as well as the peak positions, at specific excitation wavelengths were all normalized with respect to the Raman band of a silicon wafer appearing at 520 cm^{-1}. The normalized Raman

spectral patterns shown in Figures. 4.3(a)-(b) for neutral and anionic species, respectively, are largely independent of the excitation wavelength. Any spectral difference between neat and anionic states is due to the deprotonation of the thiol in the anionic state. The major peaks in Figure 3.3 are collectively summarized in Table 1 along with their vibrational assignments.

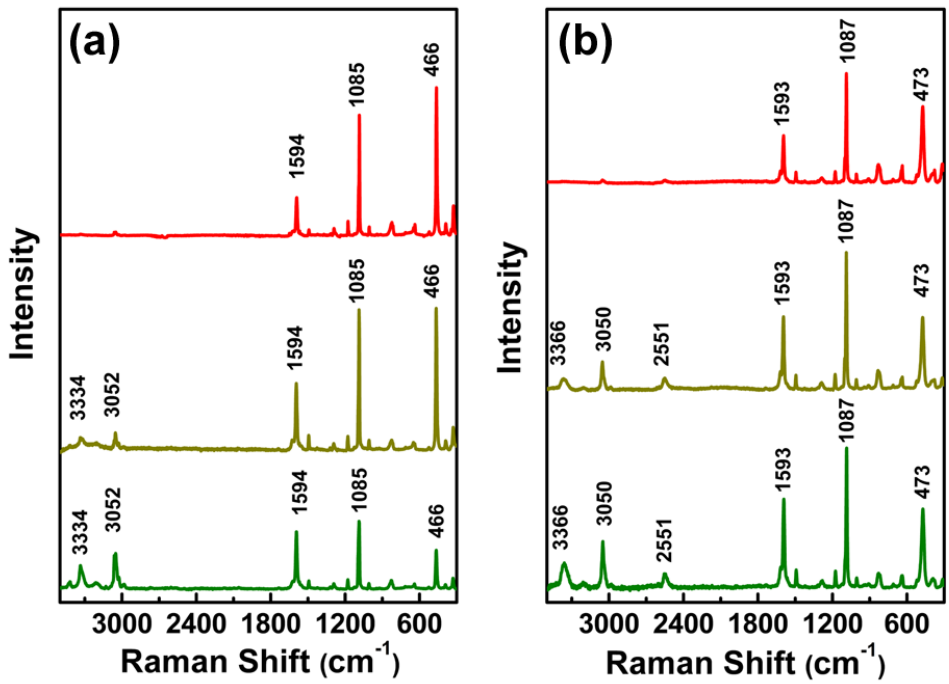

Figure 3.3. Normal Raman spectra of 4-ABT (a) in neat solid state and (b) in anionic state in alkaline solution, taken using the 632.8 nm line of a He/Ne laser (top), the 568 nm line of an Ar/Kr laser (middle), and the 514.5 nm line of an Ar ion laser (bottom) as excitation sources. All spectral intensities were normalized with respect to those of silicon wafers used for instrument calibration.

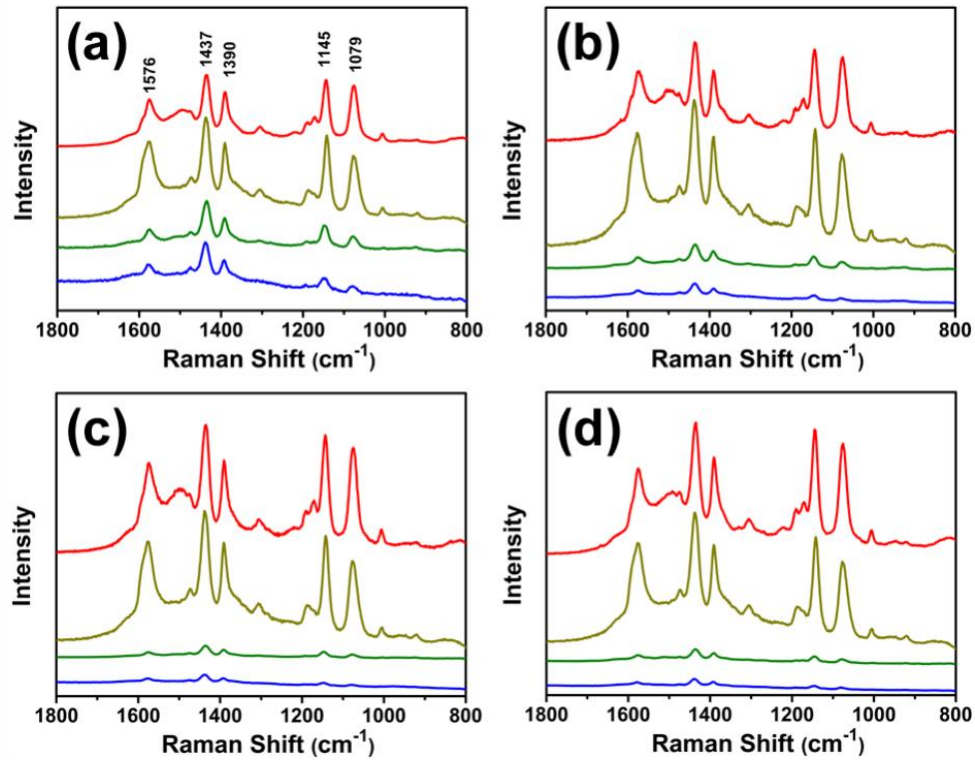

Figure 3.4. SERS spectra of 4-ABT on flat Au taken after soaking for 1 h in Ag sol comprised of (a) 20-, (b) 40-, (c) 60-, and (d) 80-nm sized Ag particles, using 632.8, 568, 514.5, and 488 nm radiation (from top to bottom) as the excitation sources. All spectra were taken while spinning at 3000 rpm to minimize the effect of inhomogeneous distribution of Ag nanoparticles. In addition, all spectral intensities were normalized with respect to those of silicon wafers used for instrument calibration and also to the number of Ag nanoparticles adsorbed on 4-ABT on Au.

Figures. 4.4(a)-(d) show the Raman spectra of Ag@4-ABT/Au(flat) comprised of 20-, 40-, 60-, and 80-nm sized Ag nanoparticles, respectively, taken using 488, 514.5, 568, or 632.8 nm radiation as the excitation sources. To minimize any effect due to inhomogeneous distribution of the Ag nanoparticles, the Raman spectra were all taken while spinning the samples at 3000 rpm. As mentioned previously, all the spectra were represented after normalizing with respect to the number of surface coverage, i.e. particles/μm^2, of Ag nanoparticles, as well as the absolute intensity of a silicon wafer at 520 cm^{-1} at a specified excitation wavelength. The results indicate that fairly intense Raman spectra were obtained at both the 568 and 632.8 nm excitation, irrespective of the size of Ag nanoparticles attached to 4-ABT, while comparatively far weaker spectra were observed at the 514.5 and 488 nm excitation. Considering the fact that only a featureless spectrum was obtained when Ag nanoparticles were attached onto 4-aminophenylsilane monolayers assembled on a silicon wafer (data not shown),[117,118] the appearance of Raman peaks in Figures. 4.4(a)-(d) should be attributed to the electromagnetic coupling of the localized surface plasmon of Ag nanoparticles with the surface plasmon polariton of the Au substrate. This also implies that the Ag nanoparticles adsorbed on amino groups were neither hot particles nor hot clusters exhibiting electromagnetic enhancement. Without any noticeable electromagnetic enhancement, the chemical enhancement would also be harder to identify.

Normal Raman[a]		SERS[a]	Vibrational
Neat (solid)	Anion state	Ag@4-ABT/Au	assignment[b]
	3422vw		
3366vw	3334vw		
3050vw	3052vw		ν_{CH}, 2(a_1)
	3031vw		ν_{CH}, 13(a_1)
	2990vw		
2551vw			ν_{SH}
1737vw	1737vw		
1616w	1627vw		δ_{NH}
1593m	1594m	1592w	ν_{CC}, 8a(a_1)
1570vw	1568vw	1585m	ν_{CC}, 8b(b_2)
1492vw	1495vw	1489w	ν_{CC}+ δ_{CH}, 19a(a_1)
		1475w	
1422vw	1423vw	1437s	ν_{CC}+ δ_{CH}, 19b(b_2)
1367vw	1371vw	1390m	ν_{CC}+ δ_{CH}, 3(b_2)
		1311vw	ν_{CC}+ δ_{CH}, 14(b_2)
1286w	1290vw		
		1233vw	
1176w	1180w	1186vw	δ_{CH}, 9a(a_1)
1150vw		1145s	δ_{CH}, 9b(b_2)
1099w	1091w		
1087m	1085m	1079m	ν_{CS}, 7a(a_1)
1008vw	1008vw	1006vw	γ_{CC}+γ_{CCC}, 18a(a_1)
		920vw	π_{CH}, 5b(b_1)
907vw			δ_{SH}
829w	828w		
		818vw	
713vw	714vw	714vw	π_{CH} +π_{CS} +π_{CC}, 4b(b_1)
644w	649w	640vw	γ_{CCC}, 12(a_1)
		544vw	
519vw	524vw		γ_{CCC}, 16b(b_1)

Table 3.1. Raman spectral peaks of 4-aminobenzenethiol measured in free and surface adsorbed state using the excitation laser of 568 nm.

[a]Unit in wavenumber (cm^{-1}). [b]Taken from ref. 19, denoting ν; stretch, δ and γ; bend, π; wagging, τ; torsion, vs; very strong, s; strong, m; medium, w; weak, and vw; very weak. The ring modes correspond to those of benzene under C_{2v} symmetry.

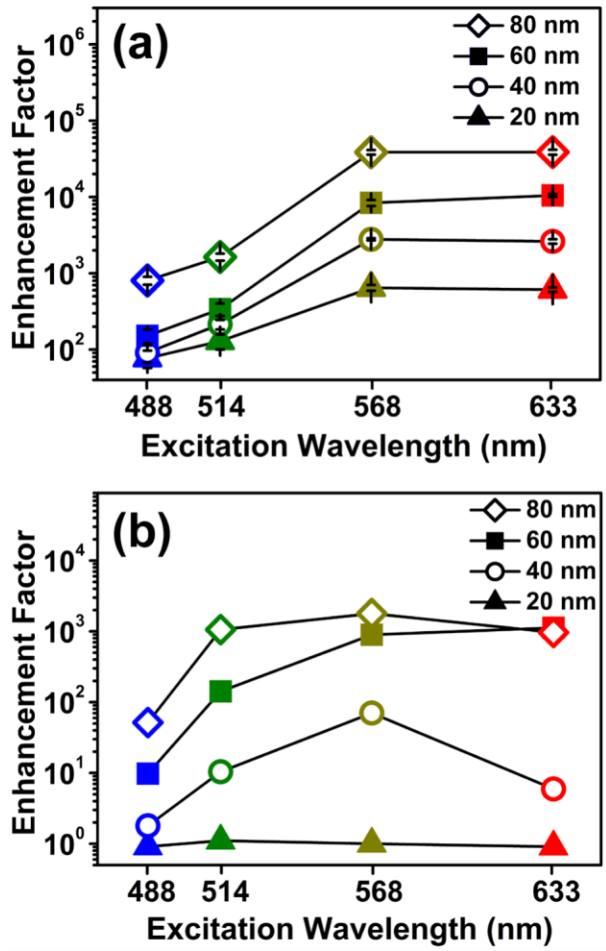

Figure 3.5. (a) Experimental and (b) theoretical enhancement factors (EFs) determined for the 7a band of 4-ABT in Ag@4-ABT/Au drawn as a function of the excitation wavelength, as well as the size of Ag nanoparticles. Experimental EFs were determined by referring to the SERS spectra shown in Figure 3. Theoretical EFs were predicted using the 3D-FDTD method by taking into account the portions of the perpendicular and parallel polarizations in actual experimental conditions. See text.

For a more quantitative comparison, we have estimated the EF values for all spectra shown in Figure 3.4. Specifically, the EFs were determined by comparing the SERS and NR intensities of the 7a band of 4-ABT at ~1080 cm^{-1} because it is a typical a_1-type band supposed to arise from electromagnetic field enhancement coupled with chemical enhancement. At first, the number of 4-ABT molecules illuminated by the laser light used in obtaining the NR spectrum in Figure 3.3 had been estimated by taking account of the facts that the size of the laser spot is ~1 μm, its penetration depth into 4-ABT is ~40 μm (since Raman signals reached a steady state when the thickness of an organic film became greater than 40 μm),[119] and the density of 4-ABT in the solid state is 1.18 g/cm^3.[120] Assuming that the sampling volume is well represented by the product of the laser spot size and its penetration depth, the number of 4-ABT molecules illuminated is calculated to be 1.8×10^{11} (i.e., 3.0×10^{-13} mol). We subsequently estimated the number of 4-ABT molecules that could be present on the planar Au substrate. Invoking the fact that each 4-ABT molecule occupies an area of ~0.20 nm^2 at the full coverage limit on Au,[121] the number of 4-ABT molecules that can be illuminated by an 1 μm sized laser beam is calculated to be 3.9×10^6 (i.e., 6.5×10^{-18} mol). The ratio of the numbers of 4-ABT molecules illuminated in NR and SERS spectral measurements would then amount to 4.6×10^4 (i.e., $1.8 \times 10^{11}/3.9 \times 10^6$). The apparent EF values may then be obtained by dividing the latter value with the intensity ratio of the 7a band of 4-ABT in NR and SERS spectra. Dividing further the apparent EF values with the average number of Ag nanoparticles per μm^2 on 4-ABT on planar Au should result in EF values that can eventually be used when assessing the size effect of Ag nanoparticles. The EF

values obtained in this way are plotted in Figure 3.5(a) as a function of the excitation wavelength, as well as the size of Ag nanoparticles. It is evident that a more intense Raman signal is obtained with an increase in the size of the Ag nanoparticles, as well as an increase in the excitation wavelength, for instance, from 488 and 514.5 nm to 568 and/or 632.8 nm.

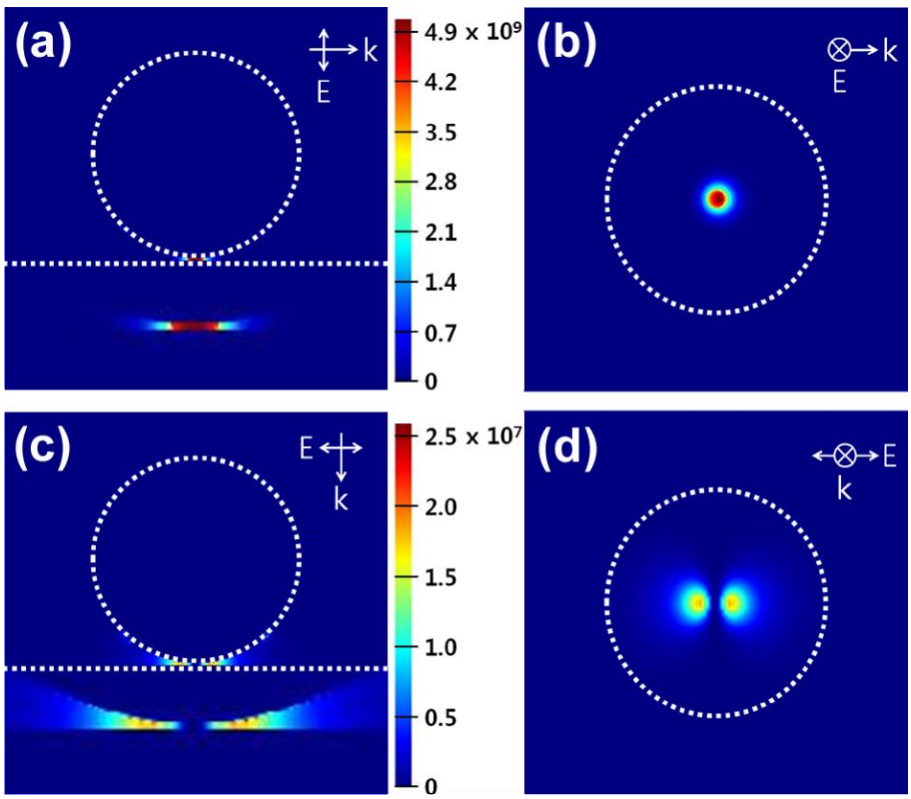

Figure 3.6. Intensity distribution ($|E/E_0|^4$) of induced local electric field E relative to the excitation field E_0 near 80-nm sized Ag sphere and Au cuboid, calculated by the 3D-FDTD method in a condition that the electric field (568 nm radiation) is directed perpendicular (a and b) or parallel (c and d) to the surface of the Au cuboid. Insets are the magnified images of the gap sites.

It is intriguing to see that according to Figure 3.5(a) the maximum EF

values are observed, irrespective of the size of Ag nanoparticles, at the 568 nm excitation, and are maintained up to the excitation at 632.8 nm. To see whether this is acceptable, we have carried out 3D-FDTD simulations. As described in the Experimental section, a nanostructure was modeled in this simulation to be composed of a single silver sphere of diameter 20 ~ 80 nm laid on a cubical gold substrate of dimensions 400 nm × 400 nm × 150 nm. The gap distance between the Ag sphere and Au cuboid was fixed at 1 nm. Figure 3.6 shows the FDTD result obtained using an 80-nm sized Ag nanoparticle irradiated by 568 nm light. As in other cases, the intensity of the induced electric field was extremely sensitive to the polarization direction of the incident radiation. An especially strong electric field was thus induced at the gap when a perpendicularly polarized light was used as the incident light. Hence, taking account of the fact that the Raman scattering enhancement could be represented as $|E/E_o|^4$ (E and E_o are the local and input fields, respectively),[8] the maximum EF value could be as large as 5.1×10^9, while the maximum in response to the parallel-polarized light would be at most 2.6×10^5. However, these maximum values are not wholly representative of the effect of Ag nanoparticles. Firstly, therefore, we have averaged out the theoretical EF values all around the Ag nanoparticle. Secondly, for a better comparison with the experimental values, we have taken into account the arrangement of the Raman laser used in this work. Actually in our experimental configuration, the laser beam was directed along the normal to the sample. In this configuration, the electric field of the incident light would be considered mostly to be polarized parallel to the substrate. However, we have to acknowledge that a lens with a very short focal length was used to measure

the Raman spectra. A part of the laser beam would then have been highly refracted, especially at the edge. A perpendicularly polarized beam was therefore inevitably present at the sampling position. We have accordingly estimated the percentage of a perpendicularly polarized beam by referring to the diameter of the laser beam (7 mm before focusing) and the focal length of the object lens (9 mm). The theoretical EF values thus computed by weighting the contribution of perpendicular and parallel polarized light are finally represented in Figure 3.5(b).

Although the theoretical EF values are an order of magnitude smaller than the experimental values, the general pattern of variation is similar in both cases. First of all, in agreement with experiment, the higher EF value was computed in all excitation states when the larger Ag particle was laid on the flat Au. Secondly, the maximum EF value was computed to occur in most cases under the irradiation of 568 nm light, which is also consonant with the experimental observation. In our previous study, when an Au nanoparticle was laid on 4-ABT on a flat Au substrate, increasing EF values were observed for larger particles, as in this case. However, for the case when an Au nanoparticle was laid on 4-ABT, the EF value at the 568 nm excitation was several tens of times smaller than that at the 632.8 nm excitation. This obviously contrasts with what is observed when an Ag nanoparticle was laid on 4-ABT. Supposedly, it is connected with the fact that the surface plasmon band of an Ag nanoparticle is located at 420 nm, but that of an Au nanoparticle is located at 520 nm. This would suggest that the kind of metal itself determines the optimum excitation wavelength to be applied to induce the maximum SERS effect in a nanogap system (comprised of a spherical metal nanoparticle and a flat metal

substrate), and even in that condition, the highest enhancement can be achieved only when a proper sized metal nanoparticle is used.

As described in chapter 2, 4-ABT is an unusual molecule in the sense that its SERS spectral feature is dependent not only on the kinds of SERS substrates but also on the measurement conditions.[51,52,102,103] Osawa et al.[51] reasoned that the appearance of strong lines of b_2 symmetry is due to intensity borrowing from an intense $\pi \rightarrow \pi^*$ molecular transition ($^1A_1 \rightarrow {}^1B_2$) at 300 nm. In line with this reasoning, Lombardi and Birke[77] explained the observed spectrum of 4-ABT using the Herzberg-Teller surface selection rules: They even figured out the relative charge-transfer (CT) contribution to SERS in 4-ABT. This was based on a unified expression for SERS, which contained a product of three resonance denominators, representing the surface plasmon resonance, the molecule-metal charge-transfer resonance at the Fermi level, and an allowed molecular resonance. Since those three resonances were linked by a product of four matrix elements in the numerator, they could not be totally independent. The polarizability tensor for the molecule-metal system would then be represented as the sum of three terms, i.e. A, B, and C alike the Albrecht terms,[122] and accordingly, a totally symmetric mode could be enhanced via a CT mechanism (along with an electromagnetic mechanism), by virtue of the A term associated with resonance Raman spectroscopy involving the Fermi state. Furthermore, both the totally and nontotally symmetric vibrations are able to be enhanced via a CT mechanism from the contribution of either the B or C terms, involving the Herzberg-Teller vibronic couplings associated with the molecule-to-metal or molecule-to-metal transition. Hence, it is impractical to separate out the CT

contributions from the electromagnetic contributions. Anyhow, in the absence of CT contributions, the relative enhancement of the nontotally symmetric bands to the totally symmetric bands should be the same, regardless of the excitation wavelength. On the other hand, if we excite in the region of a CT resonance, the enhancement of the nontotally symmetric bands relative to the totally symmetric bands will vary as we scan through the resonance. In this sense, we have evaluated the band areas of the three strong b_2 bands (3, 9b, and 19b), as well as that of one strong a_1 band (7a) in all the spectra in Figure 3.4. Figures. 4.7(a)-(c) show the relative intensity of the 3-, 9b-, and 19b-bands with respect to that of the 7a band, drawn versus the excitation laser wavelength. It is seen that all b_2 bands decrease in intensity with respect to the 7a band as the excitation wavelength is increased. There is also no size dependence of Ag nanoparticles laid on 4-ABT on Au. These all clearly indicate that the chemical enhancement mechanism is involved equally in all Raman spectra shown in Figure 3.4. Otherwise, as mentioned above, there is no reason for the b_2 bands to vary in intensity relative to the a_1 bands as a function of the excitation wavelength.

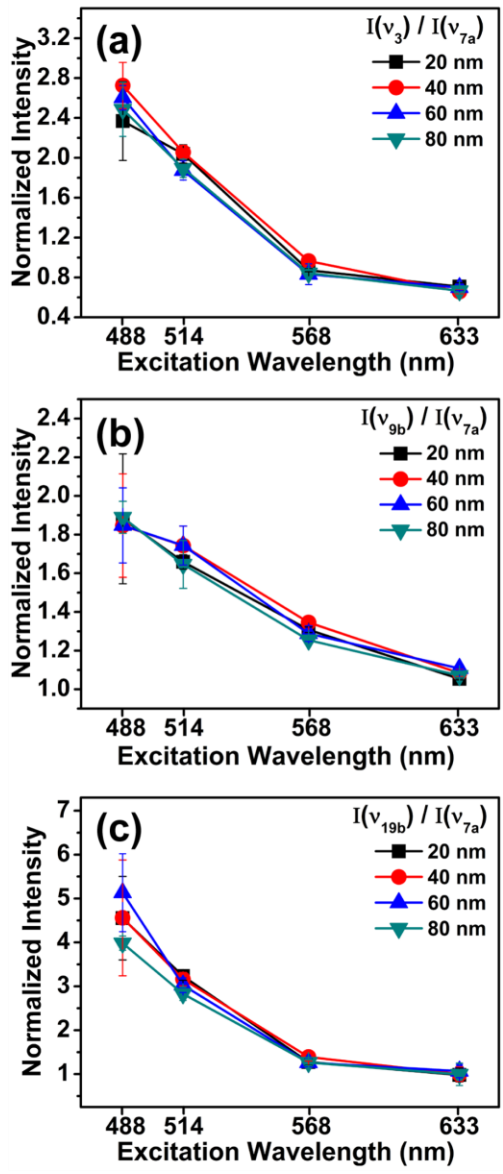

Figure 3.7. The relative peak intensities of the (a) 3, (b) 9b, and (c) 19b bands of 4-ABT in Figure 3.4 with respect to the 7a band, i.e., $I(\nu_3)/I(\nu_{7a})$, $I(\nu_{9b})/I(\nu_{7a})$, and $I(\nu_{19b})/I(\nu_{7a})$, drawn versus the excitation wavelength. All of the symbols shown were the average of 5 different measurements with the error bars denoting their standard deviation.

3.3.2 SERS of 4-ABT sandwiched between flat Au and Au/Ag alloy nanoparticles

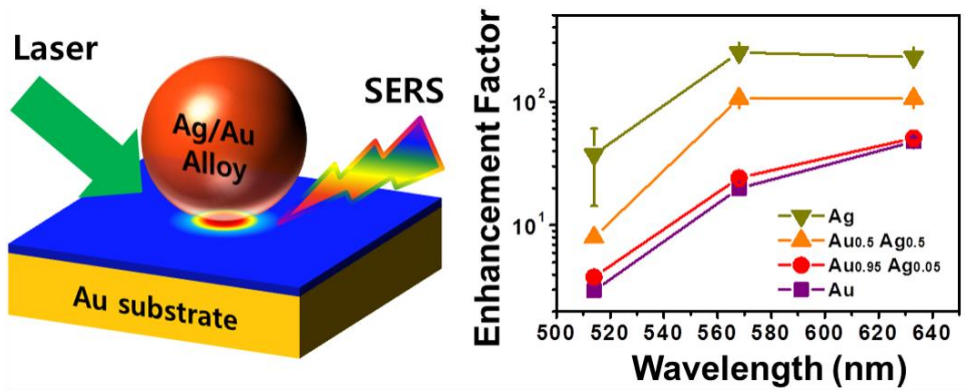

Scheme 3.2. A scheme for the preparation of a nanogap and the enhancement factor

Au/Ag alloy nanoparticles were generated when Au and Ag ions were reduced simultaneously by sodium citrate in the same solution. Figure 3.8(a) shows the UV/vis spectra of Au, $Au_{0.95}Ag_{0.05}$, $Au_{0.5}Ag_{0.5}$, and Ag nanoparticles in a colloid state. Only 1 plasmon band appeared for each type of nanoparticle, probably because of predominance of spherical particles. According to the FE-SEM images (see Figure 3.9), most of the nanoparticles were in fact spherically shaped, with a mean diameter of ~35 nm. According to EDX analyses, the molar ratios of Au and Ag atoms in the $Au_{0.5}Ag_{0.5}$ and $Au_{0.95}Ag_{0.05}$ nanoparticles were 49.4 : 50.6 and 93.2 : 6.8, respectively; the apparent compositions are thus acceptable. Pure Au and Ag nanoparticles exhibited strong SPR bands at 522 and 406 nm, respectively. The plasmon band of Au was blue-shifted as Ag was added into Au. The SPR peak position varied linearly

as a function of the mole fraction of Ag (x_{Ag}) contained in Au/Ag nanoparticles (Figure 3.8(b)). For a mechanical mixture of 50% Ag and 50% Au sols, the SPR of Ag nanoparticles was identified at 406 nm along with that of Au at 522 nm (data not shown). However, the SPR band of $Au_{0.50}Ag_{0.50}$ nanoparticles was identified only at 467 nm. For $Au_{0.95}Ag_{0.05}$ nanoparticles, the SPR band was observed at 516 nm.[18]

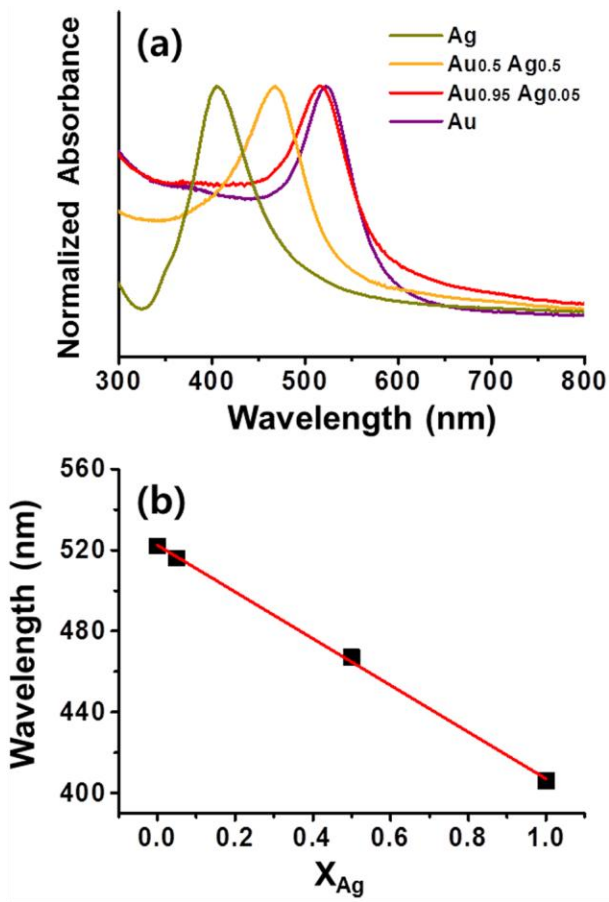

Figure 3.8. (a) UV/vis absorption spectra of Ag, $Au_{0.5}Ag_{0.5}$, $Au_{0.95}Ag_{0.05}$, and Au nanoparticles in the colloid state. (b) Positions of surface plasmon bands plotted against the mole fraction of Ag (x_{Ag}) in the nanoparticles.

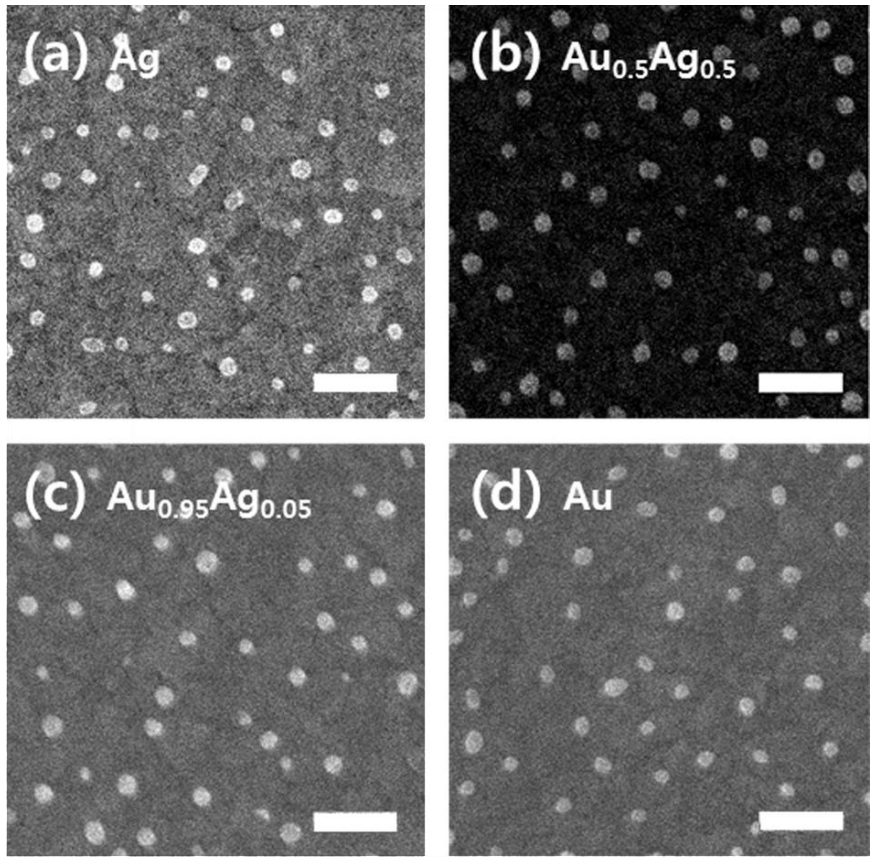

Figure 3.9. FE-SEM images measured after soaking 1,4-PDI/Au for 1 h in (a) Ag, (b) $Au_{0.5}Ag_{0.5}$, (c) $Au_{0.95}Ag_{0.05}$, or (d) Au sols (scale bar = 200 nm).

Vacuum-evaporated Au films consisted of atomically planar terraces. Raman peaks were not observed for 1,4-PDI and 4-ABT assembled on these Au films, irrespective of the excitation wavelength in the region of 514.5 to 632.8 nm. As described below, Raman peaks were observed when 1,4-PDI- or 4-ABT-adsorbed Au substrates were immersed in Au, Ag, or Au/Ag alloy sols, which was due to the formation of SERS-active nanogaps between nanoparticles and the flat Au substrate.

For a comparative study, the number of Au, Ag or Au/Ag nanoparticles that form the nanogaps are needed to be taken into account. The surface coverage of metal nanoparticles was not large even after immersion in sols for 1 h,[123,124] which was due to a repulsive interaction between metal nanoparticles capped with negatively charged citrate ions as a stabilizer.[116] As shown in Figure 3.9, Au, Ag, or Au/Ag nanoparticles were quite evenly distributed over 1,4-PDI without coagulation. The number density of Ag, $Au_{0.5}Ag_{0.5}$, $Au_{0.95}Ag_{0.05}$, and Au nanoparticles on 1,4-PDI were 58, 54, 45, and 43 particles/μm^2, respectively: these correspond to the surface coverage of 4.9, 4.7, 4.6, and 4.6%, respectively. Because of the low surface coverage, all the nanoparticles were separated by more than 100 nm. The SERS peaks of 1,4-PDI should then be independent of the interaction of nanoparticles. A similar presumption was made for the 4-ABT on Au system.

Figures 3.10(a)-(d) show the Raman spectra of 1,4-PDI on Au observed after adsorption of Ag, $Au_{0.5}Ag_{0.5}$, $Au_{0.95}Ag_{0.05}$, and Au nanoparticles, respectively; 3 spectra in each panel from top to bottom were measured using 632.8-, 568-, and 514.5-nm excitation sources, respectively. As described in the Experimental section, all spectra in Figure 3.10 were obtained under rotation at 3000 rpm to average out any inhomogeneous distribution of metal nanoparticles on 1,4-PDI/Au. In addition, all spectra were normalized to that of a silicon wafer at 520 cm^{-1} and to the number of metal nanoparticles bound to 1,4-PDI. Four peaks are observed in Figure 3.10, specifically at 2173 (or 2179), 1598, 1204, and 1163 cm^{-1}, each of which can be assigned to NC stretching, ring 8a, ring 7a, and ring 9a modes of 1,4-PDI, respectively. More intense signal was observed, irrespective of the excitation

wavelength, when Ag-rich nanoparticles were adsorbed on 1,4-PDI/Au (consult the vertical scale bars in Figure 3.10). Regarding the excitation wavelength, a 568-nm light was the most effective in induction of Raman signal, especially when Ag nanoparticles were adsorbed on 1,4-PDI/Au, whereas a 632.8-nm light was slightly more effective than a 568-nm light when Au nanoparticles were adsorbed onto it. The 514.5-nm light was the least effective among the 3 lights.

Notably, the NC stretching band was observed at ~2179 cm^{-1} in Figure 3.10(d), whereas it was observed at ~2173 cm^{-1} in Figures 3.10(a)-(c) because the NC stretching frequency was dependent on the surface characteristics of metal nanoparticles bonded to 1,4-PDI. The surface of Au/Ag nanoparticles must be enriched with Ag in comparison with their bulk. For 35-nm sized Au/Ag nanoparticles, the outermost surfaces were covered fully with Ag in that the total mole percent of Ag was greater than 5 mole percent as for $Au_{0.95}Ag_{0.05}$.[98] The lone pair of electrons in the NC group has antibonding character; therefore, their donation to metal must result in strengthening the NC bond, exhibiting a blue-shift of the NC stretching band.[125] The higher NC stretching frequency in Figure 3.10(d) reflects the fact that the NC group had greater capability for donation of electrons to Au than to Ag.

The Raman signals in Figures 3.10(a)-(d) were likely induced not only via the electromagnetic enhancement mechanism, but also via the chemical enhancement mechanism, although the contribution of the chemical enhancement was smaller than that of the electromagnetic enhancement, which can be demonstrated by comparing the behaviors of $Au_{0.5}Ag_{0.5}$ nanoparticles with those of

Au and Ag nanoparticles. The SPR frequency of $Au_{0.5}Ag_{0.5}$ nanoparticles was approximately at the median of the Ag and Au nanoparticle frequency. The Raman signal measured after adsorption of $Au_{0.5}Ag_{0.5}$ nanoparticle onto 1,4-PDI was also near the mean of those measured after adsorption of Ag and Au nanoparticles. The origin of the Raman signal was therefore predicted to be primarily electromagnetic. The extent of electromagnetic enhancement must, however, be dependent not only on the excitation wavelength but also on the type of Au/Ag nanoparticle. On the basis of the 9a band intensity shown in Figure 3.10 (located at 1163 cm^{-1}), we estimated the enhancement factors per Au/Ag alloy nanoparticle at 3 excitation wavelengths; the results are collectively represented in Figure 3.11(c). The maximum enhancement factor was about ~2.5×10^2 when 568-nm light was irradiated onto Ag nanoparticle-adsorbed 1,4-PDI/Au. As previously discussed, higher EF values were obtained, irrespective of the excitation wavelength, when Ag-rich nanoparticles were adsorbed on 1,4-PDI on Au. The 514.5-nm light was ineffective even when using Ag nanoparticle, however, although Ag nanoparticle was more effective than Au nanoparticle. This was because a flat Au film was used as the basal substrate. To rationalize these observations, we carried out a series of FDTD calculations as described in the Experimental section.

Figure 3.11(a) shows the normalized extinction spectra calculated by 3D-FDTD for nanostructures composed of Au, $Au_{0.95}Ag_{0.05}$, $Au_{0.5}Ag_{0.5}$ or Ag nanoparticles and a flat Au surface. The extinction spectra spanned from ~575 nm to ~800 nm.[126] When a Ag nanoparticle was laid on a planar Au surface, the maximum

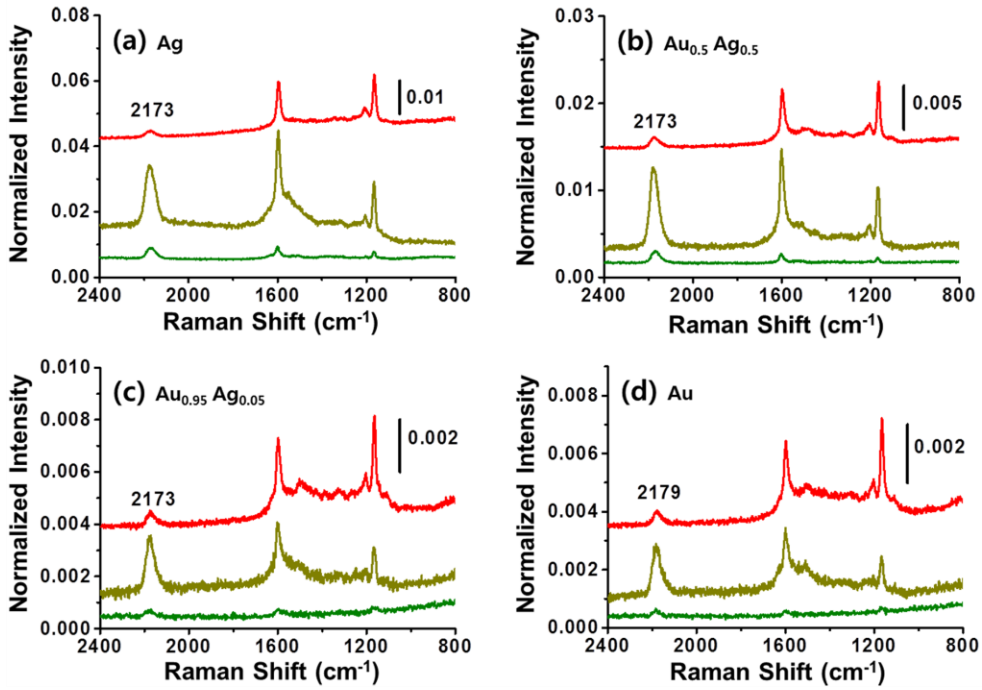

Figure 3.10. Raman spectra of 1,4-PDI/Au measured after soaking for 1 h in (a) Ag, (b) $Au_{0.5}Ag_{0.5}$, (c) $Au_{0.95}Ag_{0.05}$, or (d) Au sols, using 632.8-, 568-, or 514.5-nm radiation (from top to bottom) as the excitation source.

extinction occurred at ~620 nm, but the maximum was at ~650 nm when a Au nanoparticle was laid onto it. The 3 wavelengths of the excitation lasers used in this work are marked as vertical lines in Figure 3.11(a); their Stokes regions (covering 800 – 2400 cm^{-1}) are marked as shaded areas. A 632.8-nm light overlapped quite well with the extinction spectra, although 568-nm and 514.5-nm lights barely overlapped. However, the Stokes region of 632.8-nm light overlapped less effectively with the excitation spectra than that of 568-nm light, which is qualitatively in accordance with the experimental EFs summarized in Figure 3.11(c).

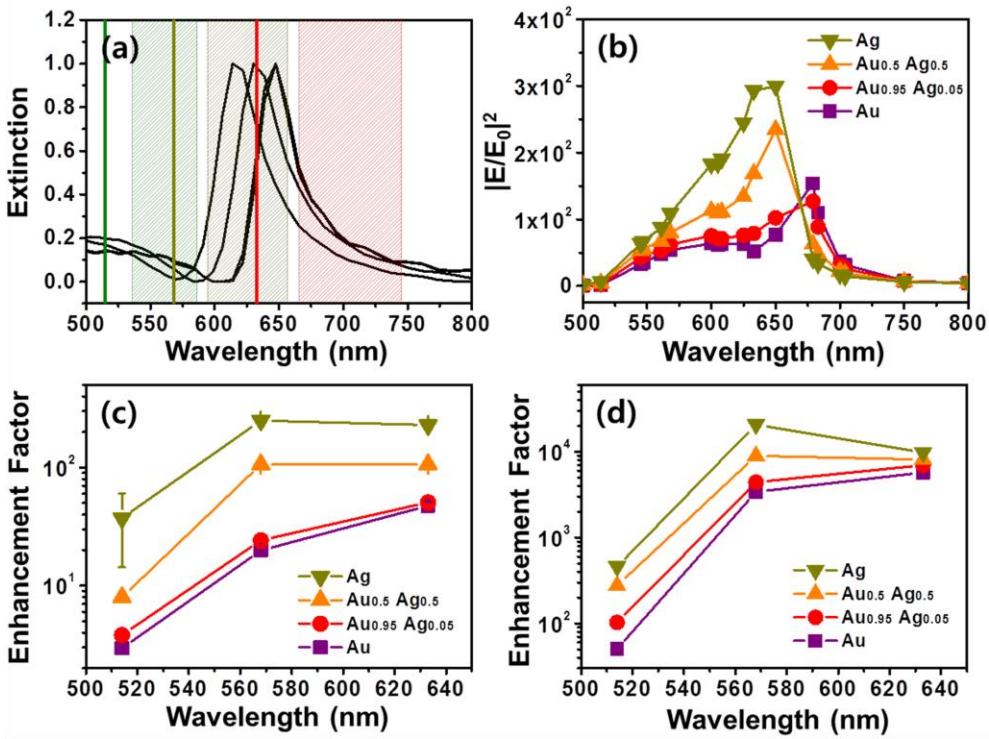

Figure 3.11. (a) Extinction spectra and (b) electric field intensities calculated by the 3D-FDTD method for nanogaps composed of a 35-nm Ag, $Au_{0.5}Ag_{0.5}$, $Au_{0.95}Ag_{0.05}$, or Au sphere and a Au cuboid. Spectra in (a) correspond, from left to right, to Ag, $Au_{0.5}Ag_{0.5}$, $Au_{0.95}Ag_{0.05}$, and Au spheres. Wavelengths of excitation lasers used in this work are marked as vertical lines; their Stokes regions (covering 800 to 2400 cm^{-1}) are marked with shaded areas. Intensities in (b) refer to those at the gap center determined as a function of the wavelength of an illuminating light. (c) Experimental EFs determined for the 9a band of 1,4-PDI and (d) FDTD-calculated EFs drawn as a function of excitation wavelength and Au/Ag alloy nanoparticle type. For (c), the error bars indicate the average and standard deviation of 3 different measurements.

To further evaluate the theoretical EF values, we calculated the electromagnetic field

intensity at the gap center as a function of the illuminating wavelength, and the results are shown in Figure 3.11(b). An incident light with the wavelength of ~640-nm sharply intensified when the nanogap was made of Ag-rich nanoparticles; however, a ~670-nm light was intensified when the nanogap was made of Au-rich nanoparticles. These characteristic wavelengths were qualitatively in accordance with the extinction maxima in Figure 3.11(a). We estimated the theoretical EF values by using the data in Figure 3.11(b). For obtaining better comparisons with the experimental values, EF was set to be $EF = |E_{ex}|^2|E_{scat}|^2$, in which E_{ex} and E_{scat} are the electric field strengths of the incident and scattered lights, respectively.[89,127] The wavelength of the incident light was chosen to be 514.5, 568, or 632.8 nm. The wavelength of the scattered light associated with the Stokes 9a band of 1,4-PDI (located at 1163 cm^{-1}) must then be 547, 608, or 683 nm. Figure 3.11(d) shows the obtained theoretical EF values. In agreement with the experimental data, higher EF values were expected, irrespective of the excitation wavelength, when Ag-rich nanoparticles were adsorbed on 1,4-PDI/Au. Specifically, a 568-nm light was the most effective when Ag-rich nanoparticles were adsorbed on 1,4-PDI/Au, while a 632.8-nm light was slightly more effective when Au-rich nanoparticles were adsorbed onto it. The maximum EF value was calculated to be as large as 2.0×10^4. Although the latter value is 2 orders of magnitude greater than the experimental value, the patterns of variation of the EF values in Figures 3.11(c) and (d) were comparable to each other. These data may suggest that the origin of the Raman signals in Figure 3.10 was primarily electromagnetic.

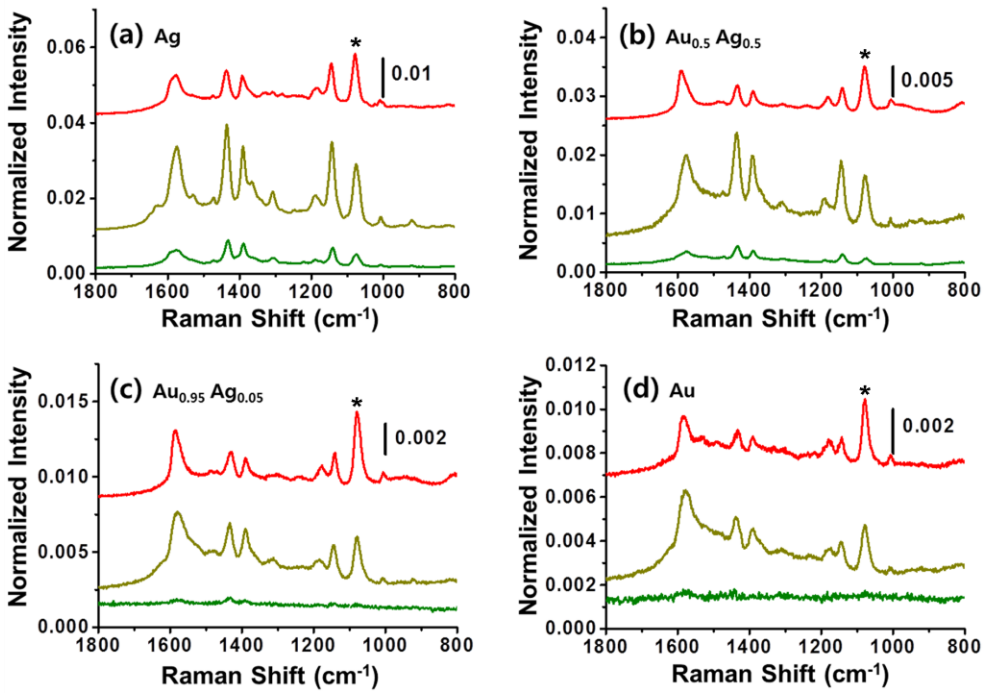

Figure 3.12. Raman spectra of 4-ABT/Au measured after soaking for 1 h in (a) Ag, (b) $Au_{0.5}Ag_{0.5}$, (c) $Au_{0.95}Ag_{0.05}$, or (d) Au sols, using 632.8-, 568-, or 514.5-nm radiation (from top to bottom) as the excitation source. Starred peak is the 7a band of 4-ABT.

In contrast to 1,4-PDI, the SERS of 4-ABT was contributed largely by chemical enhancement. Figures 3.12(a)-(d) show the Raman spectra of 4-ABT/Au measured after the adsorption of Ag, $Au_{0.5}Ag_{0.5}$, $Au_{0.95}Ag_{0.05}$, and Au nanoparticles, respectively, onto the amine group using 632.8-, 568-, or 514.5-nm radiation (top to bottom) as the excitation source. All spectra in Figure 3.12 were measured under rotation at 3000 rpm and were normalized to a silicon wafer and to the number of metal nanoparticles. The number density of Ag, $Au_{0.5}Ag_{0.5}$, $Au_{0.95}Ag_{0.05}$, and Au

nanoparticles on 4-ABT were 47, 42, 36, and 35 particles/μm^2, respectively, corresponding to the surface coverage of 4.7, 4.7, 4.0, and 4.0%, respectively. In Figure 3.12, three to four peaks were present in the region of 1100 ~ 1500 cm^{-1}, although their counterparts were not found in the normal Raman (NR) spectrum of 4-ABT (data not shown). Those peaks were attributed to the b_2-type bands of 4-ABT due to the involvement of the chemical enhancement mechanism. These b_2-type bands were invariably observed even when an acidic solution was dropped over the 4-ABT-containing nanogap system. These data indicate that the amine group of 4-ABT cannot be protonated once it has been adsorbed onto Au/Ag nanoparticles.[78] The peak at ~1070 cm^{-1} (below 1100 cm^{-1}) in Figure 3.12 can be attributed to the a_1-type ring 7a mode, which must occur mainly via the electromagnetic enhancement mechanism. On the basis of the Raman spectral characteristics of 1,4-PDI, it is not surprising that the 7a band also became stronger as Ag-rich nanoparticles were laid on 4-ABT/Au (see the starred peaks in Figure 3.12). As for 1,4-PDI, the 7a band of 4-ABT was enhanced equally by 568- and 632.8-nm lights. In those cases, the maximum electromagnetic EF per metal nanoparticle was estimated to be 6.4×10^2. As observed for 1,4-PDI in Figure 3.10, a 514.5-nm light was largely ineffective at inducing electromagnetic enhancement. After all, in all SERS spectra of 4-ABT and 1,4-PDI with different laser excitation, the enhanced Raman intensity were observed when Ag-rich nanoparticles were adsorbed on 4-ABT/Au or 1,4-PDI/Au. Consulting the FDTD calculation in Figure 3.11(b), the electromagnetic coupling of the localized surface plasmon of an Ag nanoparticle with the surface plasmon polariton of a flat Au substrate must be more effective than that of an Au nanoparticle at least

under a laser excitation at λ_{exc} < 675 nm as in this work.

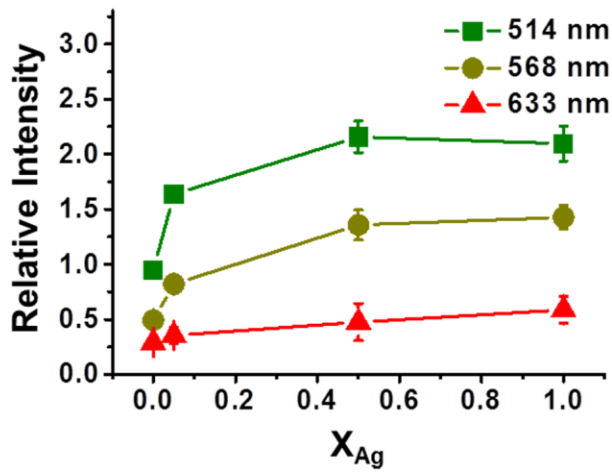

Figure 3.13. Relative peak intensity of the 19b and 7a bands of 4-ABT in Figure 3.12 drawn versus the mole fraction of Ag (x_{Ag}) in Au/Ag alloy nanoparticles and the excitation wavelength. The error bars indicate the average and standard deviation of 3 different measurements.

The relative peak intensities of the b_2-type and a_1-type bands in Figure 3.12 were highly dependent not only on the excitation wavelength, but also on the type of metal nanoparticle laid onto it.[79] Because the appearance of the b_2-type bands in the region of 1100 ~ 1500 cm^{-1} could be attributed to the combined effects of electromagnetic and chemical enhancement, the relative intensity of the b_2- and a_1-type bands must be indicative of the extent of contribution of chemical enhancement. Figure 3.13 shows the relative intensities of the 19b and 7a bands of 4-ABT in Figure 3.12 versus the mole fraction of Ag contained in the Au/Ag alloy nanoparticles laid on 4-ABT/Au. The relative intensity was more dependent on the excitation

wavelength in the following order: 514.5-nm > 568-nm > 632.8-nm. The relative peak intensity in the spectrum of $Ag_{0.5}Au_{0.5}$@4-ABT/Au was nearly the same as that of Ag@4-ABT/Au. These data may be better understood by recalling the fact that the surface characteristics of $Ag_{0.5}Au_{0.5}$ nanoparticles must be the same as that of pure Ag nanoparticles. It is particularly notable that the relative peak intensity of the $Au_{0.95}Ag_{0.05}$@4-ABT/Au system was more comparable to that of the Ag@4-ABT/Au system than to that of the Au@4-ABT/Au system. This was probably because the outermost surface of $Au_{0.95}Ag_{0.05}$ nanoparticles was also covered fully with Ag atoms. The present observation clearly indicates that chemical enhancement is governed by the composition of the metal nanoparticle surface. Therefore, we conclude that the Ag-to-4-ABT electron transfer is more favorable than the Au-to-4-ABT transfer is; charge transfer is more easily induced using a 514.5-nm light than 568- or 632.8-nm lights.[104]

3.4. Summary and Conclusion

A nanogap formed by a planar substrate and a spherical nanoparticle, where the SERS-active molecules are sandwiched between them, is an ideal geometry for SERS study. Firstly we have examined the size effect of Ag nanoparticles, along with the excitation wavelength dependence, by assembling 4-ABT in a gap between a planar Au and a variable-size Ag nanoparticle. In fact, no Raman signal was observed when 4-ABT was self-assembled on a flat Au substrate, but upon attaching Ag or Au/Ag alloy nanoparticles to the pendent isocyanide or amine groups, the Raman peaks were distinctly observed. On the one hand, a higher Raman signal was observed when larger Ag nanoparticles were attached onto 4-ABT. That is, the signal measured after attaching an 80-nm sized Ag nanoparticle was greater than that after attaching a 60-nm sized particle, and the latter was greater than that observed after attaching 40- and then 20-nm sized Ag particles. Regarding the excitation wavelength dependence, the highest Raman signal was measured at the 568 nm excitation, though that observed by the excitation at 632.8 nm was comparable. The Raman signals measured at the 514.5 and 488 nm excitations were clearly an order of magnitude weaker than that at the 568 nm excitation. When an Au nanoparticle is adsorbed on 4-ABT on flat Au, the highest Raman signal is observed at the 632.8 nm excitation, but in this case, a signal a few tens of times weaker is observed as the excitation wavelength is lowered down to 568 nm. This must be due to the different SPR of Ag and Au nanoparticles, thus suggesting that the kind of metal, the size of metal nanoparticle, and even the excitation wavelength all have to be taken into

account for the highest SERS to occur at the nanogap formed by a planar metal and a spherical metal nanoparticle.

Secondly we obtained the Raman spectral characteristics of 1,4-PDI and 4-ABT positioned at the nanogap formed by Au/Ag alloy nanoparticles and a flat Au substrate. The Raman spectra of 1,4-PDI positioned in the nanogaps could then be interpreted completely in terms of the electromagnetic enhancement mechanism. On the other hand, the a_1-type band of 4-ABT was interpretable solely by invoking the electromagnetic enhancement mechanism, whereas the b_2-type bands were derived from the combined effect of electromagnetic and chemical enhancement. The effect of electromagnetic enhancement as well as that of chemical enhancement was more distinct as Au/Ag alloy nanoparticles contained more Ag atoms In all cases, the relative intensity of the b_2 to a_1 bands was found to increase along with a decrease in the excitation wavelength, suggesting that the appearance of the b_2 bands was in fact associated with the chemical enhancement mechanism in SERS..

This was in conformity firstly with the FDTD calculation that the electromagnetic coupling of the LSP of an Ag nanoparticle with the SPP of a flat Au substrate should be more effective than that of an Au nanoparticle at least under a laser excitation at $\lambda_{exc} < 675$ nm. Separately, the outermost surface of the Au/Ag alloy nanoparticles was confirmed to be covered first with Ag atoms. Becau se the surface of $Au_{0.95}Ag_{0.05}$ nanoparticles was covered fully with Ag atoms, chemical enhancement was thus more pronounced than when pure Au nanopa rticles were laid on 4-ABT on Au.

Chapter 4

: Photoreduction of 4-Nitrobenzenethiol on Au by Hot Electrons Plasmonically Generated from Ag Nanoparticles: Gap-Mode Surface-Enhanced Raman Scattering Observation

4.1. Introduction

We concluded in chapter 2, on the basis of the SERS spectra of 4-NBT and 4-ABT on Ag in icy environments at liquid N_2 temperature, that the non-totally symmetric lines in the SERS of 4-ABT are intrinsically due to 4-ABT itself.[128] Accordingly, 4-NBT on Ag was assumed to be reduced photochemically to 4-ABT, but not to oxidize further to 4,4′-DMAB. The hot electrons generated plasmonically from Ag nanostructures must have acted as a reducing agent to convert 4-NBT on Ag to 4-ABT. The generation of hot electrons from a nanostructured Au substrate has also been reported in the literature.[40-46] Mukherjee et al. claimed that under the illumination of a 632.8 nm laser light, H_2 molecules adsorbed on Au dissociated due to hot electrons plasmonicaly generated from Au nanostructures.[47] The 4-NBT molecules adsorbed on Au, however, did not undergo photoreaction by a 632.8 nm laser light. Au substrates are, usually, SERS-inactive under 514.5 nm excitation, and therefore it is not certain whether 4-NBT on Au can be reduced to 4-ABT by 514.5 nm radiation and thus monitored by SERS. In Ag substrates, hot electrons are plasmonically generated more readily at lower excitation wavelengths; however, it is yet not confirmed whether 4-NBT on Au can also be reduced by hot electrons generated from distantly located Ag nanostructures.

Based on the nanogap characteristics described in chapter 3, it was also attempted to obtain the Raman spectra of 4-NBT on a flat Au substrate by overlying Ag-coated, micrometer-sized silica beads thereon, wherein the Ag surface was derivatized in advance with 1-alkanethiols such that 4-NBT molecules were not in

direct contact with the Ag surface. Firstly, we confirmed that the nanogaps formed by a planar Au substrate and Ag-coated, micrometer-sized silica beads are more SERS-active under 632.8 nm excitation than under 514.5 nm excitation. Secondly, we confirmed that the hot electrons generated from Ag by 514.5 nm radiation are more effective than those generated by 632.8 nm radiation in their ability to reduce 4-NBT to 4-ABT on Au. Thirdly, we demonstrated that the reduction capability of the hot electrons decreases, almost linearly, with the distance they travel from the Ag surface; the hot electrons are able to effectively transmit over a distance of, at least, ~2 nm (equivalent to the chain length of 1-hexadecanethiol) to reduce 4-NBT. Finally, we deduced that charge transfer to 4-ABT can also occur from a planar Au substrate based on the gap-mode SERS spectra of 4-ABT that exhibit the typical b_2-type vibrational bands of 4-ABT.

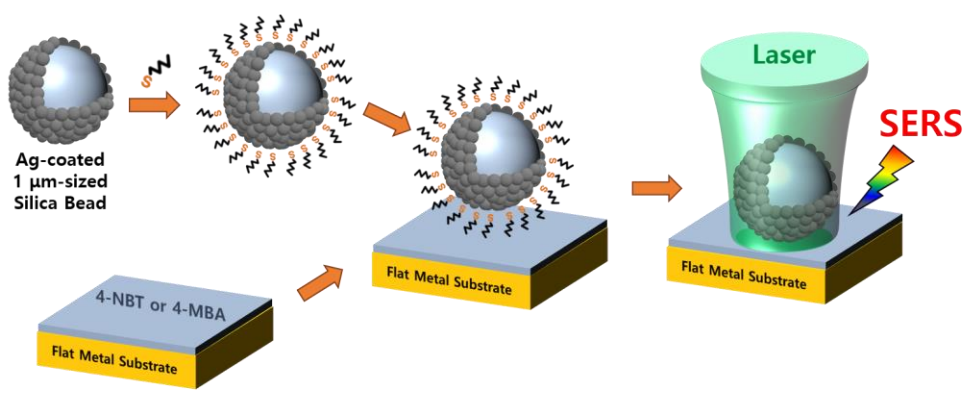

Scheme 4.1. A scheme for the preparation of a nanogap and the subsequent Raman spectral measurement adopted in this work.

4.2. Experimental

Chemicals. Au wire (99.999%), silver nitrate (99.8%), butylamine (99.5%), 4-mercaptobenzoic acid (4-MBA, 99%), 4-nitrobenzenethiol (4-NBT, 80%), 4-aminobenzenethiol (4-ABT, 97%), 1-butanethiol (1-BT, 99%), 1-decanethiol (1-DT, 98%), and 1-hexadecanethiol (1-HDT, 92%) were purchased from Sigma Aldrich Co. and used as received. Silica beads (1 μm, 99%) were obtained from Alfa Aesar Co. Other chemicals, unless specified, were of reagent grade. Aqueous solutions were prepared using triply distilled water (resistivity greater than 18.0 MΩ·cm).

Preparation of SERS-Active Ag-coated silica beads. To prepare Ag-coated silica beads, ethanol-cleaned silica was added to the silvering medium up to a final concentration of 0.10 $mg \cdot mL^{-1}$ (w/v, dried bead mass/ethanol) and then incubated for 50 min at 50°C under vigorous shaking. As a silvering mixture, the concentrations of $AgNO_3$ and butylamine were each maintained at 1 mM. After rinsing with ethanol, the Ag-coated silica were redispersed in ethanol under sonication for 5 min. Subsequently, 1 mL ethanolic solution of 10 mM 1-BT, 1-DT, or 1-HDT was added to 9 mL of ethanolic Ag-coated silica beads and later filtered out after 6 h. After rinsing the 1-BT (or 1-DT or 1-HDT)-adsorbed Ag-coated silica beads with ethanol, they were redispersed in 10 mL of ethanol under sonication.[129,130]

Preparation of smooth Au substrates. Macroscopically smooth Au substrates were prepared by resistive evaporation of titanium and gold at $1x10^{-6}$ Torr on cleaned glass slides. After the deposition of approximately 200 nm of gold, the evaporator was back-filled with nitrogen. The gold substrates were subsequently

immersed overnight in 1 mM 4-NBT (or 4-ABT) in ethanol. For the gap-mode SERS measurements, 10 μL ethanolic solution of 1-alkanethiol derivatized Ag-coated silica beads was dropped onto the 4-MBA (or 4-NBT or 4-ABT) adsorbed Au substrate.

Instrumentation. UV-vis extinction spectra were obtained using a SCINCO S-4100 spectrometer. Atomic force microscope (AFM) images were obtained on a Digital Instruments Nanoscope IIIa system. Field-emission scanning electron microscopy (FE-SEM) images were obtained using a JSM-6700F field-emission scanning electron microscope operated at 2.0 kV. Raman spectra were obtained using a Renishaw Raman system model 2000 spectrometer. The 514.5 nm line from a 20 mW Ar^+ laser (Melles-Griot model 351MA520) or the 632.8 nm line from a 17 mW He/Ne laser (Spectra Physics model 127) was used as the excitation source.

4.3. Results and Discussion

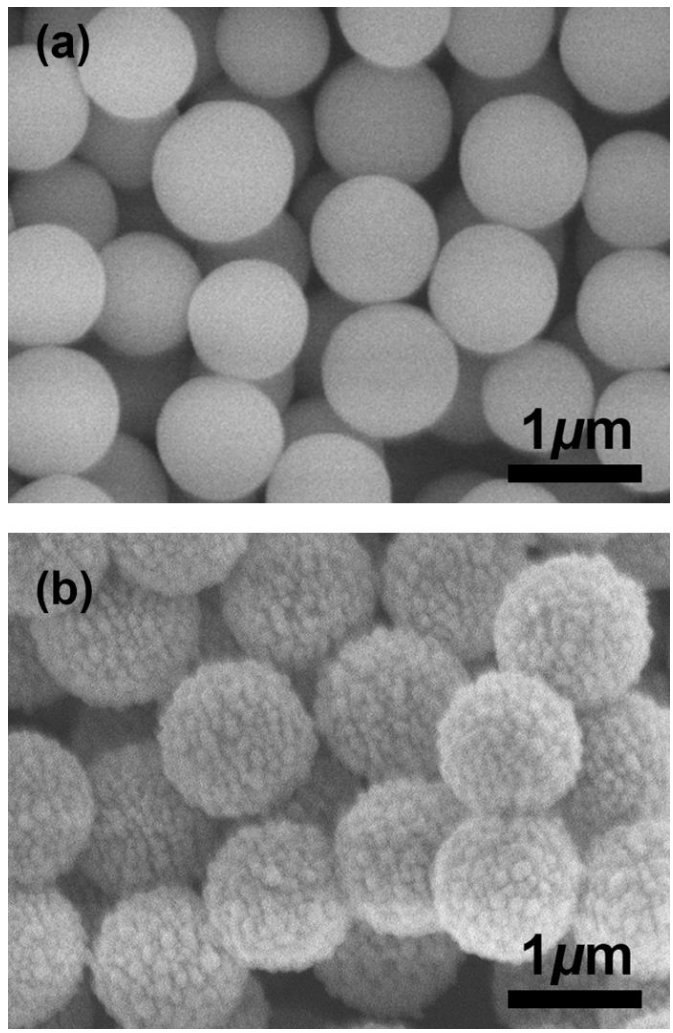

Figure 4.1. FE-SEM images of 1 μm-sized silica beads recorded (a) before and (b) after silvering them using butylamine as the reductant of $AgNO_3$.

Figures 4.1(a) and 4.1(b) show the FE-SEM images of 1 μm-sized silica beads taken before and after silvering them using butylamine as a reductant of $AgNO_3$, respectively. The Ag-coated silica beads themselves are highly SERS-active, not only at 514.5 nm excitation but also at 632.8 nm excitation. Figures 4.2(a) and 4.2(b) shows the SERS spectra of 4-MBA adsorbed on Ag-coated silica beads measured at 514.5 nm and 632.8 nm excitations, respectively; the laser power at the sampling position was the same at both excitations. The Ag-coated silica beads were first soaked in 1 mM ethanolic 4-MBA solution for 6 h and washed with ethanol, after which 10 μL aliquot was spread on a Si wafer for the Raman spectral measurement. All SERS peaks could be correlated with the normal Raman peaks of 4-MBA shown in Figure 4.2(c). The Ag-coated silica beads were more SERS-active, by a factor of ~7, under the 632.8 nm excitation than under the 514.5 nm excitation. Based on the peak intensity of the ring breathing band at 1587 cm^{-1} (ν_{8a}), the enhancement factor (EF) at the 632.8.5-nm excitation is estimated to be ~10^6; in this estimation, the roughness factor of Ag is assumed to be 1.37 by referring to the earlier publication.[130]

As described in the Experimental section, atomically smooth Au films were prepared on glass slides by a vacuum deposition process. The AFM image in Figure 4.3(a) clearly shows that the Au films are composed of atomically flat terraces. In order to evaluate the SERS activity of the nanogaps formed by a planar Au substrate and Ag-coated silica beads, we first allowed 4-MBA molecules to adsorb fully onto the Au film and then 1-alkanethiol-derivatized, Ag-coated silica beads were sparsely spread thereon. As shown in Figure 4.3(b), the Ag-coated silica beads were easily

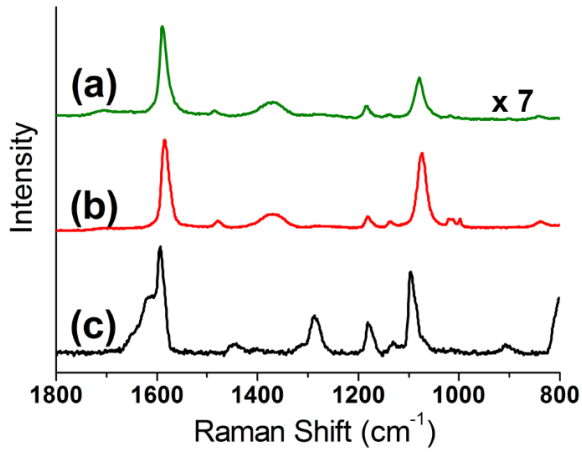

Figure 4.2. SERS spectra of 4-mercaptobenzoic acid (4-MBA) adsorbed on Ag-coated silica beads measured at (a) 514.5 nm and (b) 632.8 nm excitations. (c) Normal Raman spectrum of 4-MBA.

visualized by an optical microscope. A number of Raman spectra can thus be measured by focusing the excitation laser light on a couple of well-isolated nanogaps. Although no 4-MBA Raman peaks were identifiable at all when the excitation laser light was focused solely on the Au film, we were able to obtain their spectra by focusing the laser light on the Ag-coated silica bead. Hereafter, we will label the 1-alkanethiol adsorbed Ag-coated silica beads as SiO_2@Ag@Cn (n = 4, 10, or 16 for 1-BT, 1-DT, or 1-HDT, respectively). The bare Ag-coated silica bead is labeled as SiO_2@Ag@Cn (n = 0). On this basis, the nanogap formed by spreading SiO_2@Ag@Cn on the 4-MBA-adsorbed Au film will be labeled as SiO_2@Ag@Cn /4MBA/Au. Other nanogaps will be similarly denoted. The overall scheme of the preparation of a nanogap and the subsequent Raman spectral measurement is drawn in Scheme 4.1.

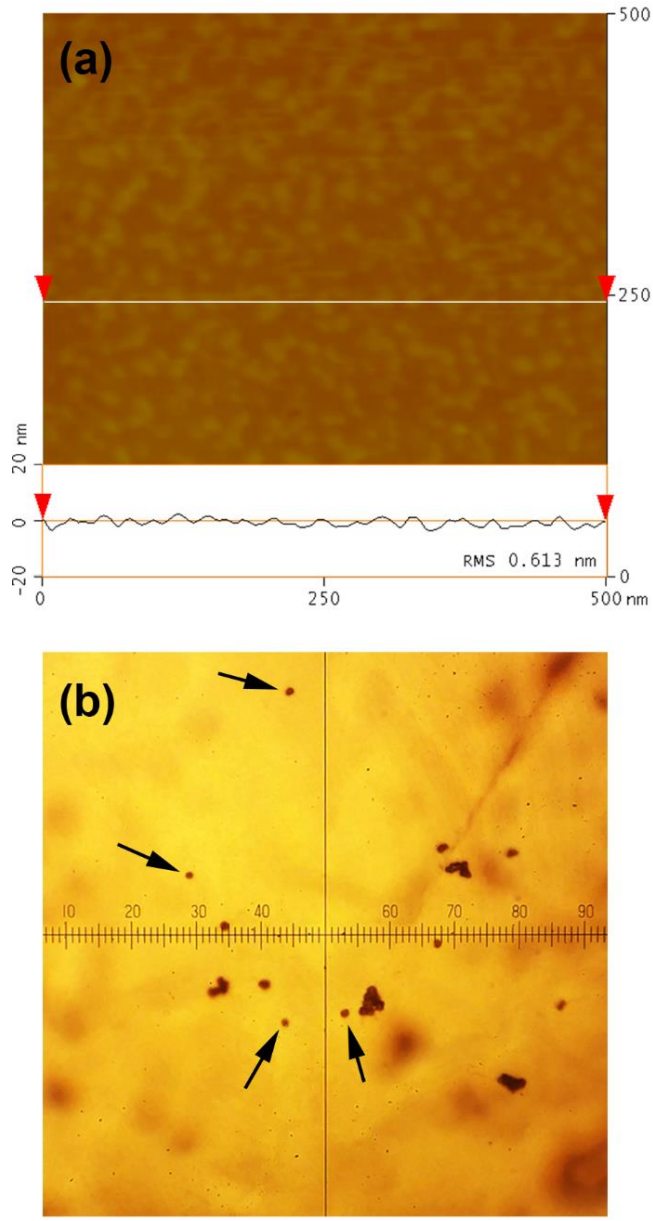

Figure 4.3. (a) AFM image of a vacuum-evaporated Au film on a glass slide and (b) optical microscope image of micrometer sized, Ag-coated silica beads spread on an Au film.

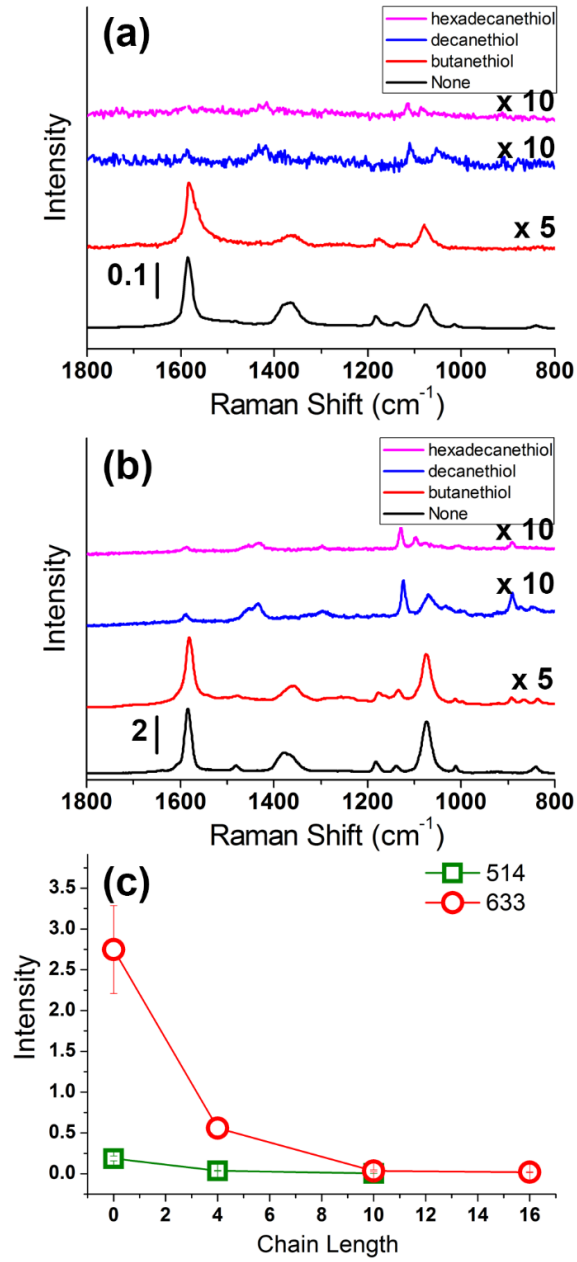

Figure 4.4. Raman spectra of Ag@C_n0/4MBA/Au, Ag@C_n4/4MBA/Au, Ag@C_n10/4MBA/Au, and Ag@C_n16/4MBA/Au obtained using (a) 514.5 nm and (b) 632.8 nm radiations as the excitation sources. (c) Intensity variation of the 4-MBA ring 8a band versus the chain length observed in (a) and (b).

Figures 4.4(a) and 4.4(b) show the collective Raman spectra of SiO_2@Ag@Cn/4MBA/Au (n = 0, 4, 10, 16) obtained using, respectively, 514.5 nm and 632.8 nm radiations as the excitation sources. Each spectrum is contributed not only by 4-MBA peaks but also by CH_2-group associated peaks. The peaks in Figure 4.4(b) are about 20 times more intense than those in Figure 4.4(a), reflecting the fact that the nanogaps formed by a planar Au substrate and Ag-coated micrometer-sized silica beads are about 20 times more SERS-active with the excitation at 632.8 nm than at 514.5 nm: the EF for the nanogap of SiO_2@Ag@C0/4MBA/Au under the 632.8 nm excitation is estimated to be ~10^5. The peak intensities of the 4-MBA ring 8a band at ~1600 cm^{-1} in Figures 4.4(a) and 4.4(b) are depicted in Figure 4.4(c) as a function of the number of methylene groups (n) separating the Ag-coated silica bead and the 4-MBA monolayer on Au film.[131] The SERS peaks decrease exponentially along the nanogap distance in conformity with the electromagnetic enhancement mechanism in SERS. Evidently, the SERS peaks are stronger at all distances with the excitation at 632.8 nm than at 514.5 nm. The 8a peak decreases in intensity to half its value as the distance increases from zero to 0.3 nm (C16 = 2.2 nm thick). The same observation is made for other peaks, suggesting that all peaks in Figures 4.4(a) and 4.4(b) are electromagnetically enhanced ones.

Figures 4.5(a) and 4.5(b) show the collective Raman spectra of SiO_2@Ag@Cn/4NBT/Au (n = 0, 4, 10, 16) obtained using 514.5 nm and 632.8 nm radiations as the excitation sources, respectively. Each spectrum is contributed not only by the peaks of the unreacted 4-NBT but also by the peaks of the photoproduct, i.e., 4-ABT, as well as the CH_2-group associated peaks.[35-39] All spectra in Figures

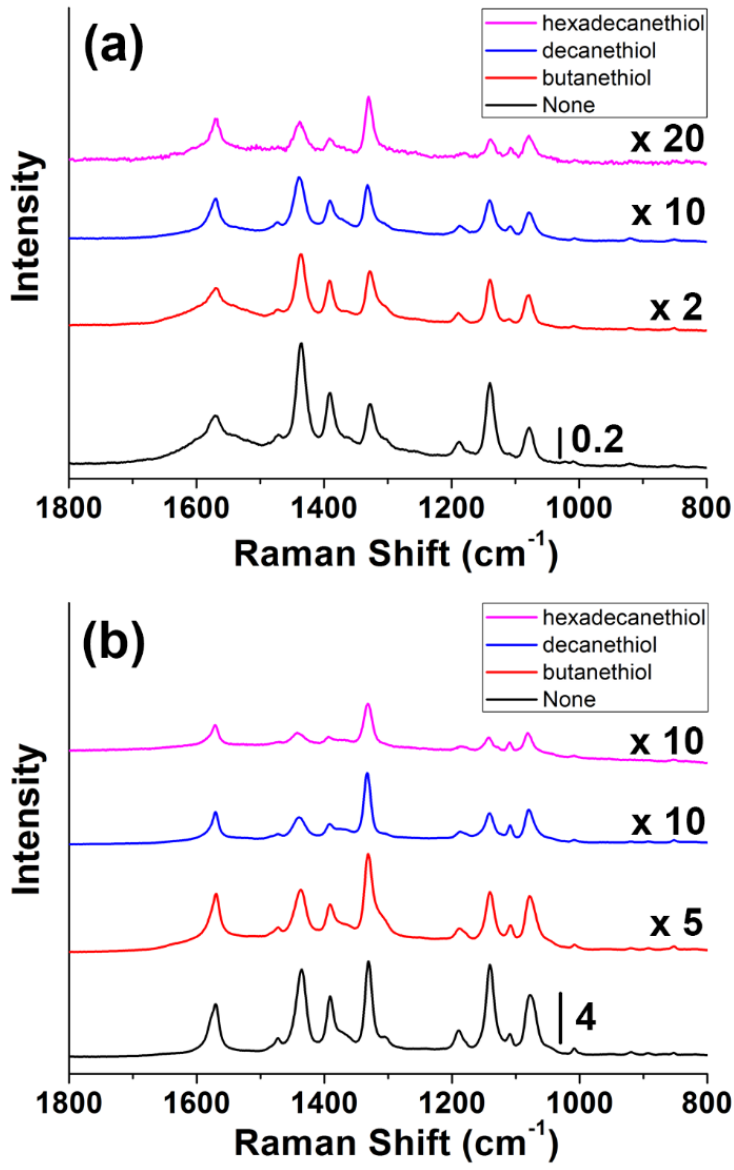

Figure 4.5. Raman spectra of Ag@C_n0/4NBT/Au, Ag@C_n4/4NBT/Au, Ag@C_n10/4NBT/Au, and Ag@C_n16/4NBT/Au obtained using (a) 514.5 nm and (b) 632.8 nm radiations as the excitation sources.

3.5(a) and 3.5(b) were obtained after irradiation by the excitation laser light for 1 min: no spectral change occurred in the following minutes. The peak intensity of the NO_2-stretching band at 1350 cm^{-1} in Figures 4.5(a) and 4.5(b) is plotted as a function of the number of methylene groups (n) of SiO_2@Ag@Cn/4NBT/Au in Figures 4.6(a) and 4.6(b), respectively (see the full lines). The dotted lines in Figures 4.6(a) and 4.6(b) correspond to the NO_2-stretching band intensities expected when 4-NBT has not been subjected to a photoreduction (deduced from the data for 4-MBA in Figure 4.4(c)). The discrepancy between the full and dotted lines is greater in Figure 4.6(a) than in Figure 4.6(b). This happens because the photoreduction of 4-NBT to 4-ABT occurs more easily with the excitation at 514.5 nm than at 632.8 nm.

Figure 4.7(a) shows the relative peak intensities of the ring 7a band at ~1080 cm^{-1} and the NO_2-stretching band at 1350 cm^{-1} in Figures 4.5(a) and 4.5(b) drawn versus the number of methylene groups (n) separating the Ag-coated silica bead and the 4-NBT monolayer on Au. More specifically, the filled circles correspond to the relative intensities measured under the 514.5 nm excitation while the open circles correspond to those under the 632.8 nm excitation. The intensity ratio decreases with the increase in chain length. The ring 7a band must then be attributed more to 4-ABT than to 4-NBT since the ratio would have remained constant if the band was entirely due to 4-NBT. The fact that the filled circles stay above the open circles in Figure 4.7(a) indicates that the photo-conversion of 4-NBT to 4-ABT occurs more readily with the excitation at 514.5 nm than at 632.8 nm. Since the ring 7a vibration is a totally symmetric ring breathing mode, its presence in the SERS spectrum of 4-ABT can be attributed to the electromagnetic

enhancement at the nanogap.

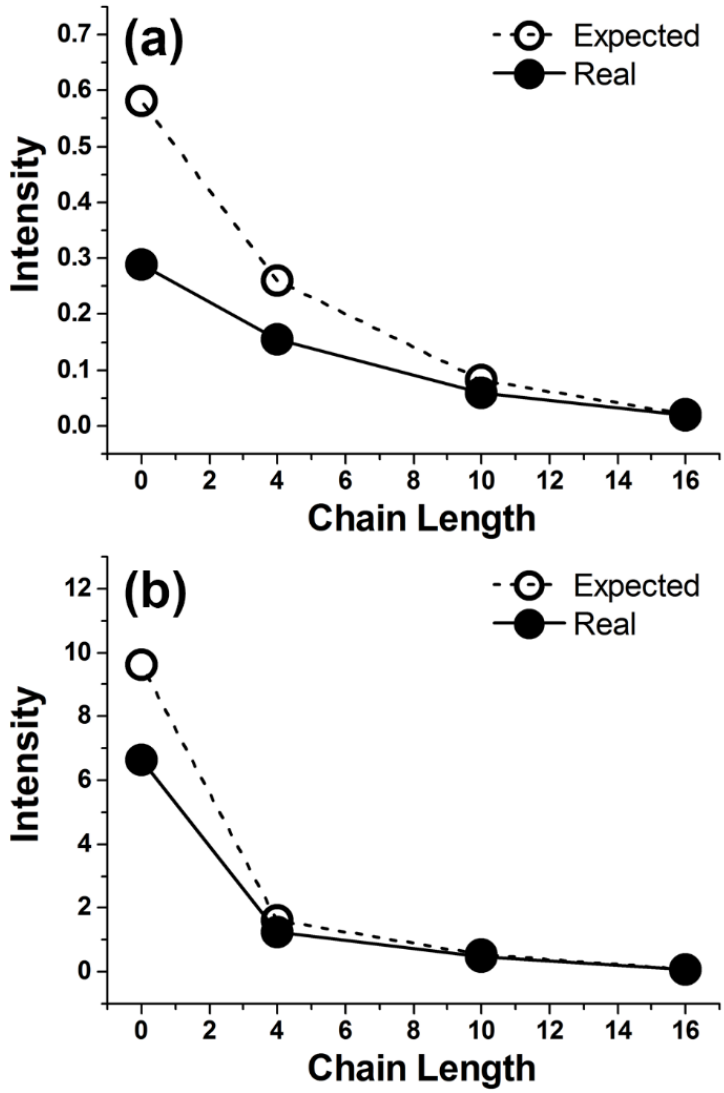

Figure 4.6. (a) Intensity variation of the 4-NBT NO_2-stretching band in Figure 4.5(a) and (b) that in Figure 4.5(b) represented versus the chain length. The dotted lines represent the NO_2-stretching band intensities expected when 4-NBT has not been subjected to a photoreduction. See text.

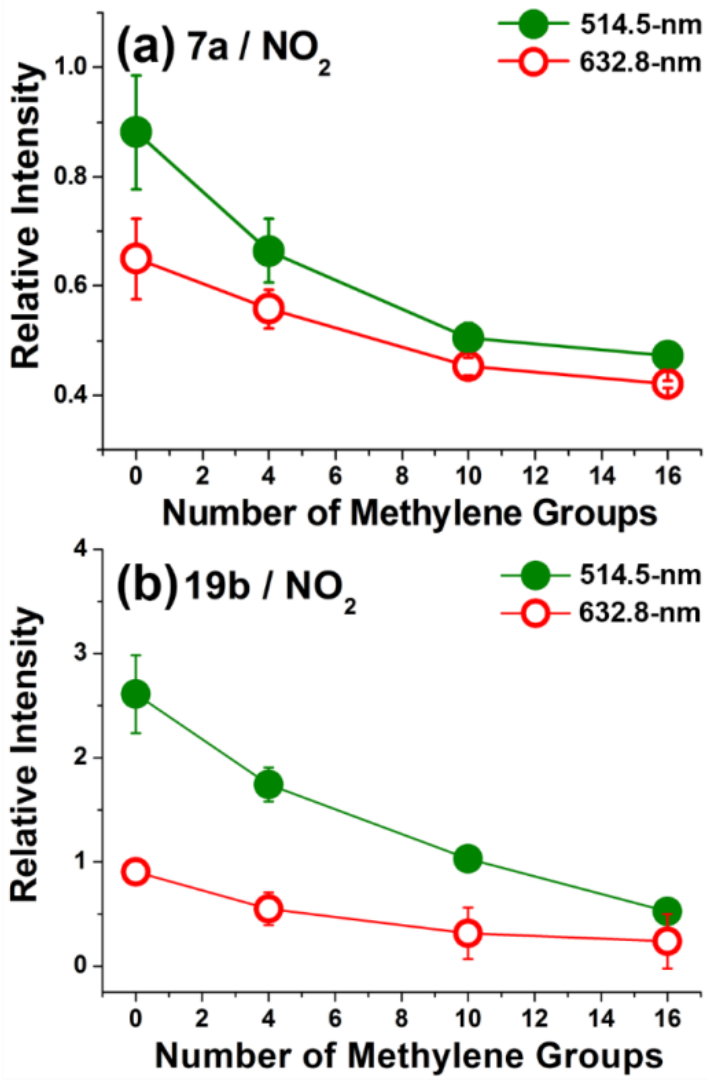

Figure 4.7. (a) Relative peak intensities of the 4-ABT ring 7a band at ~1080 cm^{-1} and (b) ring 19b band at 1435 cm^{-1}, both measured with respect to the peak intensities of the NO_2-stretching band at 1350 cm^{-1} in Figures 4.5(a) (see filled circles) and 4.5(b) (see open circles). The relative peak intensities are represented versus the chain length.

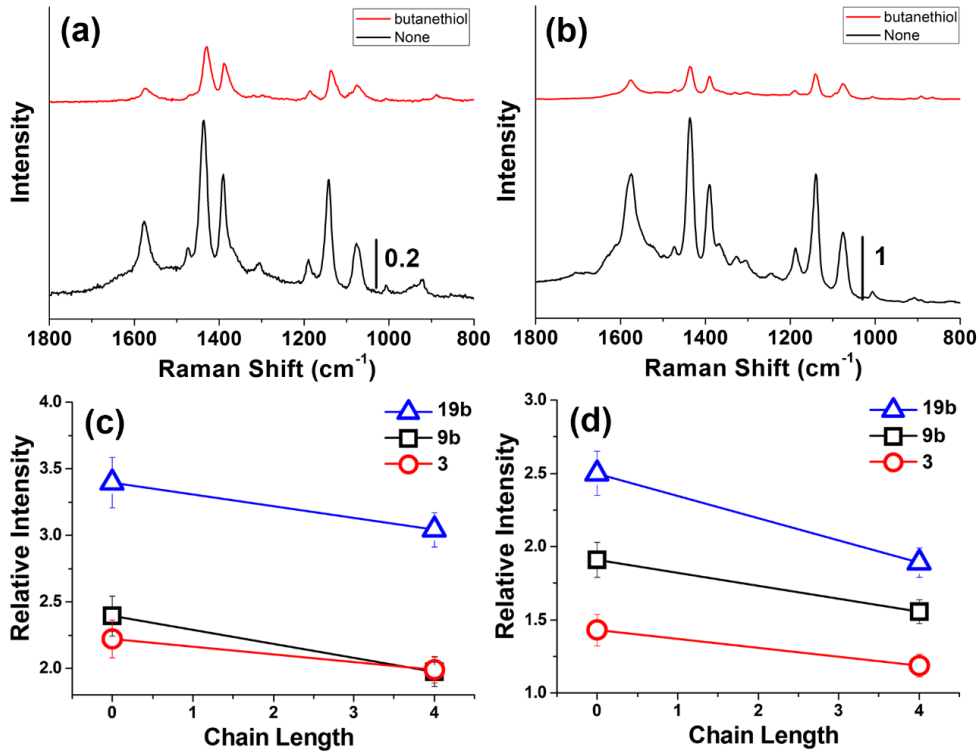

Figure 4.8. Raman spectra of Ag@C_n0/4ABT/Au and Ag@C_n4/4ABT/Au measured using (a) 514.5 nm and (b) 632.8 nm radiations as the excitation sources. (c) Relative peak intensities of the b_2-type bands measured with respect to the ring 7a band in (a) represented versus the chain length. (d) Similar ratios plotted using the data in (b).

Figure 4.7(b) shows the relative peak intensities of the 4-ABT ring 19b band at 1435 cm^{-1} with respect to the 4-NBT NO_2-stretching band at 1350 cm^{-1} in Figures 4.5(a) and 4.5(b) represented versus versus the number of methylene groups (n) of SiO_2@Ag@Cn/4NBT/Au. The filled circles correspond to the relative intensities measured under the 514.5 nm excitation while the open circles correspond to those

under the 632.8 nm excitation. The intensity ratio evidently decreases with the increase in chain length. Once again, the filled circles stay above the open circles since the photo-conversion from 4-NBT to 4-ABT occurs more readily with the excitation at 514.5 nm than at 632.8 nm. The ring 19b band (as well as the ring 7a band) is identified even in the SiO_2@Ag@C16/4NBT/Au system indicating that hot electrons travelling over a length of 2.2 nm (from the nanostructured Ag surface corresponding to the thickness of C16) still have enough energy to reduce 4-NBT to 4-ABT. The 19b band is a typical 4-ABT b_2-type band, known to originate from the chemical enhancement. The relative intensity variation of the 19b band in Figure 4.7(b) is somewhat more abrupt than that of the 7a band in Figure 4.7(a). This would imply that the chemical enhancement portion decreases more rapidly than the electromagnetic enhancement one as the nanogap distance from the Ag surface increases.

We separately confirmed that no photoreduction takes place for 4-NBT adsorbed solely on a SERS-active Au substrate. We also measured the SERS spectra of 4-ABT adsorbed solely on a SERS-active Au substrate using 632.8 nm radiation as the excitation source, not only in ambient conditions but also in an icy environment at 77 K. As seen earlier for 4-ABT on Ag, the b_2-type bands were identified clearly under both conditions, thus confirming that the b_2-type bands were indeed the characteristic bands of 4-ABT. We also measured the Raman spectra of 4-ABT positioned in a nanogap between a flat Au substrate and Ag-coated, micrometer sized silica beads. The Raman spectra of SiO_2@Ag@Cn/4ABT/Au (n = 0, 4) measured in ambient conditions using 514.5 nm and 632.8 nm radiations as the

excitation sources are shown in Figures 4.8(a) and 4.8(b), respectively. Owing to the strong scattering effect of the silica beads, however, the Raman spectra could not be measured in the icy environment. The b_2-type bands are observed in all spectra depicted in Figures 4.8(a) and 4.8(b). Figures 4.8(c) and 4.8(d) show the intensity ratios of the b_2-type bands and the 7a band in Figures 4.8(a) and 4.8(b), respectively, drawn against the number of methylene groups (n) of SiO_2@Ag@Cn/4ABT/Au. The b_2-type bands are, evidently, more intense for SiO_2@Ag@C0/4ABT/Au than for SiO_2@Ag@C4/4ABT/Au. This indicates that the effect of the chemical enhancement decreases as the distance of 4-ABT from the Ag surface increases. This, in turn, implies that hot electrons generated plasmonically from Ag nanostructures must contribute to the chemical enhancement of the b_2-type bands of 4-ABT, though indirectly, by affecting the Fermi level of the Au substrate underneath. Otherwise, the b_2-to-a_1 intensity ratios would remain constant irrespective of the 4-ABT-to-Ag distance.

4.4. Summary and Conclusion

In order to evaluate the photoreduction efficiency of the plasmonically generated hot electrons from Ag nanostructures, gap-mode SERS experiments were carried out. For that purpose, Ag-coated silica beads were initially prepared using butylamine as the reductant of silver nitrate. The Ag-coated silica beads themselves were highly SERS-active, showing a ~10^6 fold enhancement for 4-MBA under the 632.8 nm excitation. The Ag-coated silica beads were subsequently derivatized with 1-alkanethiols to obtain four different hot electron generators labeled as SiO_2@Ag@Cn0, SiO_2@Ag@Cn4, SiO_2@Ag@Cn10, or SiO_2@Ag@Cn16. To fabricate a nanogap system, atomically smooth Au substrates were separately prepared by a vacuum evaporation method and subsequently, 4-MBA, 4-NBT, or 4-ABT was self-assembled thereon. Although no Raman peaks of 4-MBA, 4-NBT, or 4-ABT were observable in this stage, the peaks could be identified by spreading the Ag-coated silica beads onto them. Since the silica beads used were 1 μm, the nanogaps formed were easily distinguished by an optical microscope. These nanogaps were initially characterized using 4-MBA as the model adsorbate owing to its photochemical stability. The EF for the nanogap of SiO_2@Ag@Cn0/4MBA/Au under the 632.8 nm excitation was estimated to be ~10^5; this nanogap was about 20 times more SERS-active with the excitation at 632.8 nm than at 514.5 nm. The 4-MBA SERS peaks decreased exponentially along the nanogap distance, in conformity with the electromagnetic enhancement mechanism in SERS. When there were 4-NBT molecules sitting in the nanogap, these were converted to 4-ABT even

though 4-NBT was not in contact with the Ag nanostructure. Hot electrons generated plasmonically from Ag nanostructures flew to 4-NBT and reduced it to 4-ABT. The photoreduction of 4-NBT to 4-ABT occurred more easily with the excitation at 514.5 nm than at 632.8 nm. Hot electrons travelling over a length of 2.2 nm corresponding to the thickness of C_n16 still had enough energy to reduce 4-NBT to 4-ABT. Presuming that the b_2-type bands of 4-ABT were associated with the chemical enhancement mechanism, the portion of chemical enhancement appeared to diminish more rapidly than that of the electromagnetic enhancement as the nanogap distance from the Ag surface was increased. This certainly implies that hot electrons generated plasmonically from Ag nanostructures must also contribute to the chemical enhancement of the b_2-type bands of 4-ABT, in addition to the Au-to-4-ABT charge transfer contribution.

Reference

References

1. Smekal, A. *Naturwissenschaften* **1923**, *11*, 873.

2. Raman, C. V.; Krishnan, K. S. *Nature* **1928**, *121*, 501.

3. Fleischmann, M.; Hendra, P. J.; McQuillan, A. *J. Chem. Phys. Lett.* **1974**, *26*, 163.

4. Albrecht, M. G.; Creighton, J. A. *J. Am. Chem. Soc.* **1977**, *99*, 5215.

5. Jeanmaire, D. L.; Van Duyne, R. P. *J. Electronanal. Chem.* **1977**, *84*, 1.

6. Nie, S. M.; Emery, S. R. *Science* **1997**, *275*, 1102.

7. Kneipp, K.; Wang, Y.; Kneipp, H.; Perelman, L. T.; Itzkan, I.; Dasari, R. R.; Feld, M. S. *Phys. Rev. Lett.* **1997**, *78*, 1667.

8. Kneipp, K.; Kneipp, H.; I, I.; Dasari, R. R.; Feld, M. S. *Chem. Rev.* **1999**, *99*, 2957.

9. Chang, R. K.; Furtak, T. E. *Surface enhanced Raman scattering*; Plenum press: New York, N.Y. ; London, 1982.

10. Xu, H. X.; Bjerneld, E. J.; Kall, M.; Borjesson, L. *Phys. Rev. Lett.* **1999**, *83*, 4357.

11. Schatz, G. C.; Van Duyne, R. P. In *Handbook of Vibrational Spectroscopy*; John Wiley & Sons, Ltd: 2006.

12. Aroca, R. *Surface-enhanced vibrational spectroscopy*; Wiley: Chichester ; Hoboken, NJ, 2006.

13. Lund, P. A.; Tevault, D. E.; Smardzewski, R. R. *J. Phys. Chem.* **1984**, *88*, 1731.

14. Schulze, W.; Charle, K. P.; Kloss, U. *Surf. Sci.* **1985**, *156*, 822.

15. Campion, A.; Kambhampati, P. *Chem. Soc. Rev.* **1998**, *27*, 241.

16. Moskovits, M. *Rev. Mod. Phys.* **1985**, *57*, 783.

17. Raether, H. *Surface plasmons on smooth and rough surfaces and on gratings*;

Springer-Verlag: Berlin ; New York ; Paris etc., 1988.

18. Maier, S. A. *Plasmonics: Fundamentals and Applications*; Springer Science+Business Media LLC: Boston, MA, 2007.

19. Jones, M. R.; Osberg, K. D.; Macfarlane, R. J.; Langille, M. R.; Mirkin, C. A. *Chem. Rev.* **2011**, *111*, 3736.

20. Kerker, M. *The scattering of light, and other electromagnetic radiation*; Academic Press: New York,, 1969.

21. Bohren, C. F.; Huffman, D. R. *Absorption and scattering of light by small particles*; Wiley: New York, 1983.

22. Reviews of Modern PhysicsKreibig, U.; Michael, V. *Optical Properties of Metal Clusters*; Springer: Berlin, 1995.

23. Fadini, A.; Schnepel, F.-M. *Vibrational spectroscopy : methods and applications*; Ellis Horwood etc.: Chichester, 1989.

24. Garrell, R. L. *Anal. Chem.* **1989**, *61*, A401.

25. Yee, K. *IEEE Transactions on Antennas and Propagation* **1966**, *14*, 302.

26. Taflove, A. *IEEE Transactions on Microwave Theory and Techniques* **1980**, *EMC-22*, 191.

27. Taflove, A.; Hagness, S. C. *Computational electrodynamics : the finite-difference time-domain method*; 3rd ed.; Artech House: Boston, 2005.

28. Nitzan, A.; Brus, L. E. *J. Chem. Phys.* **1981**, *75*, 2205.

29. Goncher, G. M.; Harris, C. B. *J. Chem. Phys.* **1982**, *77*, 3767.

30. Sandroff, C. J.; Herschbach, D. R. *J. Phys. Chem.* **1982**, *86*, 3277.

31. Goncher, G. M.; Parsons, C. A.; Harris, C. B. *J. Phys. Chem.* **1984**, *88*, 4200.

32. Wolkow, R.; Moskovits, M. *J. Chem. Phys.* **1987**, *87*, 5858.

33. Suh, J. S.; Jang, N. H.; Jeong, D. H.; Moskovits, M. *J. Phys. Chem.* **1996**, *100*, 805.

34. Lee, S. B.; Kim, K.; Kim, M. S. *J. Phys. Chem.* **1992**, *96*, 9940.

35. Shin, K. S.; Cho, Y. K.; Kim, K. *Vib. Spectrosc.* **2014**, *70*, 120.

36. Han, S. W.; Lee, I.; Kim, K. *Langmuir* **2002**, *18*, 182.

37. Kim, K.; Lee, I.; Lee, S. J. *Chem. Phys. Lett.* **2003**, *377*, 201.

38. Lee, S. J.; Kim, K. *Chem. Phys. Lett.* **2003**, *378*, 122.

39. Kim, K.; Lee, Y. M.; Lee, H. B.; Park, Y.; Bae, T. Y.; Jung, Y. M.; Choi, C. H.; Shin, K. S. *J. Raman. Spectrosc.* **2010**, *41*, 187.

40. Roukes, M. L.; Freeman, M. R.; Germain, R. S.; Richardson, R. C.; Ketchen, M. B. *Phys. Rev. Lett.* **1985**, *55*, 422.

41. Wellstood, F.; Urbina, C.; Clarke, J. *Phys. Rev. B* **1994**, *49*, 5942.

42. Petek, H.; Ogawa, S. *Prog. Surf. Sci.* **1997**, *56*, 239.

43. Fang, Z.; Wang, Y.; Liu, Z.; Schlather, A.; Ajayan, P. M.; Koppens, F. H.; Nordlander, P.; Halas, N. J. *ACS Nano* **2012**, *6*, 10222.

44. Knight, M. W.; Sobhani, H.; Nordlander, P.; Halas, N. J. *Science* **2011**, *332*, 702.

45. Lee, Y. K.; Jung, C. H.; Park, J.; Seo, H.; Somorjai, G. A.; Park, J. Y. *Nano. Lett.* **2011**, *11*, 4251.

46. Douketis, C.; Haslett, T. L.; Shalaev, V. M.; Wang, Z.; Moskovits, M. *Physica A* **1994**, *207*, 352.

47. Mukherjee, S.; Libisch, F.; Large, N.; Neumann, O.; Brown, L. V.; Cheng, J.; Lassiter, J. B.; Carter, E. A.; Nordlander, P.; Halas, N. J. *Nano. Lett.* **2013**, *13*, 240.

48. Kim, K.; Yoon, J. K. *J. Phys. Chem. B* **2005**, *109*, 20731.

49. Kim, K.; Lee, H. B.; Shin, D.; Ryoo, H.; Lee, J. W.; Shin, K. S. *J. Raman. Spectrosc.* **2011**, *42*, 2112.

50. Kim, K.; Shin, D.; Lee, H. B.; Shin, K. S. *Chem. Commun.* **2011**, *47*, 2020.

51. Osawa, M.; Matsuda, N.; Yoshii, K.; Uchida, I. *J. Phys. Chem.* **1994**, *98*, 12702.

52. Zhou, Q.; Li, X.; Fan, Q.; Zhang, X.; Zheng, J. *Angew. Chem. Int. Ed.* **2006**, *45*, 3970.

53. Uetsuki, K.; Verma, P.; Yano, T. a.; Saito, Y.; Ichimura, T.; Kawata, S. *J. Phys. Chem. C* **2010**, *114*, 7515.

54. Dong, B.; Fang, Y.; Xia, L.; Xu, H.; Sun, M. *J. Raman. Spectrosc.* **2011**, *42*, 1205.

55. Kang, L.; Xu, P.; Zhang, B.; Tsai, H.; Han, X.; Wang, H. L. *Chem. Commun.* **2013**, *49*, 3389.

56. van Schrojenstein Lantman, E. M.; Deckert-Gaudig, T.; Mank, A. J.; Deckert, V.; Weckhuysen, B. M. *Nat. Nanotechnol.* **2012**, *7*, 583.

57. You, T.; Jiang, L.; Yin, P.; Shang, Y.; Zhang, D.; Guo, L.; Yang, S. *J. Raman. Spectrosc.* **2014**, *45*, 7.

58. Kim, K.; Shin, D.; Choi, J. Y.; Kim, K. L.; Shin, K. S. *J. Phys. Chem. C* **2011**, *115*, 24960.

59. Kim, K.; Lee, S. H.; Kim, K. L.; Shin, K. S. *J. Raman. Spectrosc.* **2013**, *44*, 518.

60. Fang, Y.; Li, Y.; Xu, H.; Sun, M. *Langmuir* **2010**, *26*, 7737.

61. Huang, Y. F.; Zhu, H. P.; Liu, G. K.; Wu, D. Y.; Ren, B.; Tian, Z. Q. *J. Am. Chem. Soc.* **2010**, *132*, 9244.

62. Sun, M. T.; Xu, H. X. *Small* **2012**, *8*, 2777.

63. Wu, D. Y.; Liu, X. M.; Huang, Y. F.; Ren, B.; Xu, X.; Tian, Z. Q. *J. Phys. Chem. C* **2009**, *113*, 18212.

64. Sun, M. T.; Huang, Y. Z.; Xia, L. X.; Chen, X. W.; Xu, H. X. *J. Phys. Chem. C* **2011**, *115*, 9629.

65. Zong, S.; Wang, Z.; Yang, J.; Cui, Y. *Anal. Chem.* **2011**, *83*, 4178.

66. Choi, H. K.; Shon, H. K.; Yu, H.; Lee, T. G.; Kim, Z. H. *J. Phys. Chem. Lett.* **2013**, *4*, 1079.

67. Fennema, O.; Duckworth, R. B. *In Water Relations of Foods*, 1975.

68. Lodge, J. P.; Baker, M. L.; Pierrard, J. M. *J. Chem. Phys.* **1956**, *24*, 716.

69. Kim, K.; Lee, S. H.; Choi, J. Y.; Shin, K. S. *J. Phys. Chem. C* **2014**, *118*, 3359.

70. Kim, K.; Lee, H. B.; Lee, J. W.; Park, H. K.; Shin, K. S. *Langmuir* **2008**, *24*, 7178.

71. Sun, X.; Dong, S.; Wang, E. *Langmuir* **2005**, *21*, 4710.

72. Kim, K.; Lee, J. W.; Choi, J. Y.; Shin, K. S. *Langmuir* **2010**, *26*, 19163.

73. Yuan, M. Q.; Zhan, S. H.; Zhou, X. D.; Liu, Y. J.; Feng, L.; Lin, Y.; Zhang, Z. L.; Hu, J. M. *Langmuir* **2008**, *24*, 8707.

74. Skadtchenko, B. O.; Aroca, R. *Spectrochim. Acta. A* **2001**, *57*, 1009.

75. Futamata, M.; Maruyama, Y.; Ishikawa, M. *Vib. Spectrosc.* **2002**, *30*, 17.

76. Jiang, J.; Bosnick, K.; Maillard, M.; Brus, L. *J. Phys. Chem. B* **2003**, *107*, 9964.

77. Lombardi, J. R.; Birke, R. L. *J. Phys. Chem. C* **2008**, *112*, 5605.

78. Kim, K.; Kim, K. L.; Shin, D.; Choi, J. Y.; Shin, K. S. *J. Phys. Chem. C* **2012**, *116*, 4774.

79. Kim, K.; Lee, H. B.; Choi, J. Y.; Shin, K. S. *J. Phys. Chem. C* **2011**, *115*, 21047.

80. Michaels, A. M.; Jiang, J.; Brus, L. *J. Phys. Chem. B* **2000**, *104*, 11965.

81. Markel, V. A.; Shalaev, V. M.; Zhang, P.; Huynh, W.; Tay, L.; Haslett, T. L.; Moskovits, M. *Phys. Rev. B* **1999**, *59*, 10903.

82. Aravind, P. K.; Metiu, H. *Surf. Sci.* **1983**, *124*, 506.

83. Prodan, E.; Radloff, C.; Halas, N. J.; Nordlander, P. *Science* **2003**, *302*, 419.

84. Ni, J.; Lipert, R. J.; Dawson, G. B.; Porter, M. D. *Anal. Chem.* **1999**, *71*, 4903.

85. Kim, N. H.; Lee, S. J.; Kim, K. *Chem. Commun*. **2003**, 724.

86. Cao, P. G.; Gu, R. N.; Tian, Z. Q. *Langmuir* **2002**, *18*, 7609.

87. Chu, W.; LeBlanc, R. J.; Williams, C. T.; Kubota, J.; Zaera, F. *J. Phys. Chem. B* **2003**, *107*, 14365.

88. Tian, Z. Q.; Ren, B.; Wu, D. Y. *J. Phys. Chem. B* **2002**, *106*, 9463.

89. Le Ru, E. C.; Meyer, M.; Blackie, E.; Etchegoin, P. G. *J. Raman. Spectrosc.* **2008**, *39*, 1127.

90. Park, W. H.; Ahn, S. H.; Kim, Z. H. *ChemPhysChem* **2008**, *9*, 2491.

91. Ikeda, K.; Suzuki, S.; Uosaki, K. *Nano. Lett.* **2011**, *11*, 1716.

92. Liu, J. H.; Wang, A. Q.; Chi, Y. S.; Lin, H. P.; Mou, C. Y. *J. Phys. Chem. B* **2005**, *109*, 40.

93. Henglein, A. *Chem. Rev.* **1989**, *89*, 1861.

94. Bond, G. C. *Catal. Today* **2002**, *72*, 5.

95. Wang, A. Q.; Liu, J. H.; Lin, S. D.; Lin, T. S.; Mou, C. Y. *J. Catal.* **2005**, *233*, 186.

96. Fernandez, J. L.; Raghuveer, V.; Manthiram, A.; Bard, A. J. *J. Am. Chem. Soc.* **2005**, *127*, 13100.

97. Atwan, M. H.; Northwood, D. O.; Gyenge, E. L. *Int. J. Hydrogen Energy* **2007**, *32*, 3116.

98. Kim, K.; Kim, K. L.; Choi, J. Y.; Lee, H. B.; Shin, K. S. *J. Phys. Chem. C* **2010**, *114*, 3448.

99. Kim, K.; Choi, J. Y.; Shin, K. S. *Spectrochim. Acta. A* **2013**, *100*, 3.

100. Kim, K.; Choi, J. Y.; Shin, D.; Lee, H. B.; Shin, K. S. *Bull. Korean Chem. Soc.* **2011**, *32*, 2941.

101. Yang, L. B.; Ruan, W. D.; Jiang, X.; Zhao, B.; Xu, W. Q.; Lombardi, J. R. *J. Phys. Chem. C* **2009**, *113*, 117.

102. Liu, S. S.; Zhao, X. M.; Li, Y. Z.; Zhao, X. H.; Chen, M. D. *J. Chem. Phys.* **2009**, *130*.

103. Sun, M. T.; Xu, H. X. *ChemPhysChem* **2009**, *10*, 392.

104. Kim, K.; Lee, H. B.; Yoon, J. K.; Shin, D.; Shin, K. S. *J. Phys. Chem. C* **2010**, *114*, 13589.

105. Sullivan, D. M. *Electromagnetic simulation using the FDTD method*; Institute of Electrical and Electronics Engineers: New York, 2000.

106. Oubre, C.; Nordlander, P. *J. Phys. Chem. B* **2004**, *108*, 17740.

107. Link, S.; Wang, Z. L.; El-Sayed, M. A. *J. Phys. Chem. B* **1999**, *103*, 3529.

108. Lee, P. C.; Meisel, D. *J. Phys. Chem.* **1982**, *86*, 3391.

109. Palik, E. D.; Ghosh, G. In *Academic Press handbook series*; Academic Press: Orlando ; London, 1985, p 1 online resource (5 v.

110. Chowdhury, M. H.; Chakraborty, S.; Lakowicz, J. R.; Ray, K. *J. Phys. Chem. C* **2011**, *115*, 16879.

111. Lee, K. S.; El-Sayed, M. A. *J. Phys. Chem. B* **2006**, *110*, 19220.

112. Malinsky, M. D.; Kelly, K. L.; Schatz, G. C.; Van Duyne, R. P. *J. Am. Chem. Soc.* **2001**, *123*, 1471.

113. Sherry, L. J.; Chang, S. H.; Schatz, G. C.; Van Duyne, R. P.; Wiley, B. J.; Xia, Y. N. *Nano. Lett.* **2005**, *5*, 2034.

114. Rubio, J. E. F.; Arsuaga, J. M.; Taravillo, M.; Baonza, V. G.; Caceres, M. *Exp. Therm. Fluid. Sci.* **2004**, *28*, 887.

115. Dorohoi, D. O.; Airinei, A.; Dimitriu, M. *Spectrochim. Acta. A* **2009**, *73*, 257.

116. Hayat, M. A. *Colloidal gold: principles, methods, and applications. 1*; Academic press: San Diego, 1989.

117. Chumanov, G.; Sokolov, K.; Gregory, B. W.; Cotton, T. M. *J. Phys. Chem.* **1995**, *99*, 9466.

118. Grabar, K. C.; Freeman, R. G.; Hommer, M. B.; Natan, M. J. *Anal. Chem.* **1995**, *67*, 735.

119. Yoon, J. K.; Kim, K.; Shin, K. S. *J. Phys. Chem. C* **2009**, *113*, 1769.

120. Kim, Y. T.; Mccarley, R. L.; Bard, A. J. *J. Phys. Chem.* **1992**, *96*, 7416.

121. Gole, A.; Sainkar, S. R.; Sastry, M. *Chem. Mater.* **2000**, *12*, 1234.

122. Albrecht, A. C. *J. Chem. Phys.* **1961**, *34*, 1476.

123. Kim, K.; Ryoo, H.; Lee, Y. M.; Shin, K. S. *J. Colloid. Interf. Sci.* **2010**, *342*, 479.

124. Kim, K.; Ryoo, H.; Shin, K. S. *Langmuir* **2010**, *26*, 10827.

125. Ontko, A. C.; Angelici, R. J. *Langmuir* **1998**, *14*, 1684.

126. Ciraci, C.; Hill, R. T.; Mock, J. J.; Urzhumov, Y.; Fernandez-Dominguez, A. I.;

Maier, S. A.; Pendry, J. B.; Chilkoti, A.; Smith, D. R. *Science* **2012**, *337*, 1072.

127. Ye, J.; Hutchison, J. A.; Uji-i, H.; Hofkens, J.; Lagae, L.; Maes, G.; Borghs, G.; Van Dorpe, P. *Nanoscale* **2012**, *4*, 1606.

128. Kim, K.; Choi, J.-Y.; Shin, K. S. *J. Phys. Chem. C* **2014**, *118*, 11397.

129. Park, H. K.; Yoon, J. K.; Kim, K. *Langmuir* **2006**, *22*, 1626.

130. Kim, K.; Kim, H. S.; Park, H. K. *Langmuir* **2006**, *22*, 8083.

131. Michota, A.; Bukowska, J. *J. Raman. Spectrosc.* **2003**, *34*, 21.

Appendix

List of Publications

1. Kwan Kim, **Jeong-Yong Choi** and Kuan Soo Shin "Surface-Enhanced Raman Scattering of 4-Nitrobenzenethiol and 4-Aminobenzenethiol on Silver in Icy Environments at Liquid Nitrogen Temperature" *J. Phys. Chem. C* **2014**, *118*, 11397.
2. Kwan Kim, Seung Hun Lee, **Jeong-Yong Choi** and Kuan Soo Shin "Fe^{3+} to Fe^{2+} Conversion by Plasmonically Generated Hot Electrons from Ag Nanoparticles: Surface-Enhanced Raman Scattering Evidence" *J. Phys. Chem. C* **2014**, *118*, 3359.
3. Kwan Kim, **Jeong-Yong Choi** and Kuan Soo Shin "Enhanced Raman Scattering in Gaps Formed by Planar Au and Au/Ag Alloy Nanoparticles" *J. Phys. Chem. C* **2013**, *117*, 11421.
4. Kwan Kim, **Jeong-Yong Choi** and Kuan Soo Shin "Effect of Foreign Molecules on the SERS of Probe Molecules Trapped in Gaps between Planar Ag and Nano-sized Ag Particles" *Bull. Korean Chem. Soc.* **2013**, *34*, 793.
5. Kwan Kim, **Jeong-Yong Choi** and Kuan Soo Shin, "Raman Scattering Characterization of 1,4-Phenylenediisocyanide in Au-Au and Ag-Au Nanogaps" *Spec. Chim. Acta. Part A* **2013**, *100*, 3.
6. Kwan Kim, Ji Won Lee, Dongha Shin, **Jeong-Yong Choi** and Kuan Soo Shin "Organic Isocyanide-Adsorbed Gold Nanostructure: A SERS Sensory Device for Indirect Peak-Shift Detection of Volatile Organic Compounds" *Analyst* **2012**, *137*, 1930.

7. Sung-Soo Kim, **Jeong-Yong Choi**, Kwan Kim and Byeong-Hyeok Sohn, "Large Area Tunable Arrays of Graphene Nanodots Fabricated using Diblock Copolymer Micelles" *Nanotechnology* **2012**, *23*, 125301.
8. Kwan Kim, Kyung Lock Kim, Dongha Shin, **Jeong-Yong Choi** and Kuan Soo Shin "Surface-Enhanced Raman Scattering of 4-Aminobenzenethiol on Ag and Au: pH Dependence of b_2-Type Bands" *J. Phys. Chem. C* **2012**, *116*, 4774
9. Kuan Soo Shin, Young Kwan Cho, **Jeong-Yong Choi** and Kwan Kim, "Facile Synthesis of Silver-Deposited Silanized Magnetite Nanoparticles and Their Application for Catalytic Reduction of Nitrophenols" Appl. Catal. A: General **2012**, *413-414*, 170.
10. Kwan Kim, Dongha Shin, **Jeong-Yong Choi**, Kyung Lock Kim and Kuan Soo Shin, "Surface-Enhanced Raman Scattering Characteristics of 4-Aminobenzenethiol Derivatives Adsorbed on Silver" *J. Phys. Chem. C* **2011**, *115*, 24960.
11. Kwan Kim, Hyang Bong Lee, **Jeong-Yong Choi** and Kuan Soo Shin, "Characteristics of Nanogaps Formed by Planar Au and Pt Nanoparticles Revealed by Raman Spectroscopy" *J. Phys. Chem. C* **2011**, *115*, 21047.
12. Kwan Kim, **Jeong-Yong Choi**, Hyang Bong Lee and Kuan Soo Shin, "Raman Scattering of 4-Aminobenzenethiol Sandwiched between Ag Nanoparticle and Macroscopically Smooth Au Substrate: Effects of Size of Ag Nanoparticles and the Excitation Wavelength" *J. Chem. Phys.* **2011**, *135*, 124705.
13. Kwan Kim, **Jeong-Yong Choi**, Dongha Shin, Hyang Bong Lee and Kuan Soo Shin, "Comparative Characteristics of Gold-Gold and Gold-Silver Nanogaps

Probed by Raman Scattering Spectroscopy of 1,4-Phenylenediisocyanide" *Bull. Korean. Chem. Soc.* **2011**, *32*, 2941.

14. Kwan Kim, Kyung Lock Kim, **Jeong-Yong Choi**, Dongha Shin and Kuan Soo Shin, "Effect of Volatile organic Chemicals on Surface-Enhanced Raman Scattering of 4-Aminobenzenethiol on Ag: Comparison with the Potential Dependence" *Phys. Chem. Chem. Phys.* **2011**, *13*, 15603.
15. Kwan Kim, Hyang Bong Lee, **Jeong-Yong Choi**, Kyung Lock Kim and Kuan Soo Shin, "Surface-Enhanced Raman Scattering of 4-Aminobenznethiol in Nanogaps between a Planar Ag Substrate and Pt Nanoparticles" *J. Phys. Chem. C* **2011**, *115*, 13223.
16. Kwan Kim, Kyung Lock Kim, **Jeong-Yong Choi** and Kuan Soo Shin, "Effect of Organic Vapors and Potential-Dependent Raman Scattering of 2,6-Dimethylphenylisocyanide on Platinum Nanoaggregates" *Phys. Chem. Chem. Phys.* **2011**, *13*, 5981.
17. Kwan Kim, Hyang Bong Lee, **Jeong-Yong Choi** and Kuan Soo Shin, "Silver-Coated Dye-Embedded Silica Beads: A Core Material of Dual Tagging Sensors Based on Fluorescence and Raman Scattering" *ACS Appl. Mater. Inter.* **2011**, *3*, 324.
18. Kwan Kim, Ji Won Lee, **Jeong-Yong Choi** and Kuan Soo Shin, "The pH Effect on Surface Potential of Polyelectrolytes-Capped Gold Nanoparticles Probed by Surface-Enhanced Raman Scattering" *Langmuir* **2010**, *26*, 19163.
19. Kwan Kim, **Jeong-Yong Choi**, Hyang Bong Lee and Kuan Soo Shin, "Silanization of Ag-Deposited Magnetite Particles: An Efficient Route to

Fabricate Magnetic Nanoparticle-Based Raman Barcode Materials" *ACS Appl. Mater. Inter*. **2010**, *2*, 1872.

20. **Jeong-Yong Choi**, Kwan Kim and Kuan Soo Shin, "Surface-Enhanced Raman Scattering Inducible by Recyclable Ag-Coated Magnetic Particles" *Vib. Spectrosc*. **2010**, *53*, 117.
21. Kwan Kim, Kyung Lock Kim, **Jeong-Yong Choi**, Hyang Bong Lee and Kuan Soo Shin, "Surface Enrichment of Ag Atoms in Au/Ag Alloy Nanoparticles Revealed by Surface-Enhanced Raman Scattering of 2,6-Dimethylphenyl Isocyanide" *J. Phys. Chem. C* **2010**, *114*, 3448.
22. Kuan Soo Shin, **Jeong-Yong Choi**, Chan Seok Park, Hee Jin Jang and Kwan Kim, "Facile Synthesis and Catalytic Application of Silver-Deposited Magnetic Nanoparticles" *Catal. Lett.* **2009**, 133, 1.

List of Presentations

International conferences

1. **Jeong-Yong Choi** and Kwan Kim, "Surface-Enhanced Raman Scattering of 4-Nitrobenzenethiol and 4-Aminobenzenethiol on Silver in Icy Environments at Liquid Nitrogen Temperature" *24rd International Conference on Raman Spectroscopy*, Jena, Germany, Aug. 2014. (Oral Presentation)
2. **Jeong-Yong Choi,** Kuan Soo Shin and Kwan Kim, "Silanization of Silver-Coated Magnetic Nanoparticles: A Core Material of SERS-Based Barcoding System" *Surface-Enhanced Spectroscopies 2014,* Chemnitz, Germany, Aug. 2014.
3. **Jeong-Yong Choi** and Kwan Kim, "Silica- and Silver-Coated Magnetic Nanoparticles: A Core Material of SERS-Based Barcoding System" *The 4th International Nanotechnology Conference & Exhibition*, Tel Aviv, Israel, Mar. 2014.
4. **Jeong-Yong Choi,** Kuan Soo Shin and Kwan Kim, "Enhanced Raman Scattering in Gaps Formed by Planar Au and Au/Ag Alloy Nanoparticles" *7th International Conference on Advanced Vibrational Spectroscopy*, Kobe, Japan, Aug. 2013.
5. **Jeong-Yong Choi,** Kuan Soo Shin and Kwan Kim, "Effect of Foreign Molecules on the SERS of Probe Molecules Trapped in Gaps between Planar Ag and Nano-sized Ag Particles" *23rd International Conference on Raman Spectroscopy* Bangalore, India, Aug. 2012.
6. **Jeong-Yong Choi** and Kwan Kim, "Silanization of Ag-Deposited Magnetite Particles: An Efficient Route to Fabricate Magnetic Nanoparticle-based Raman

Barcode Materials" *2nd International Advances in Applied Physics &Materials Science Congress* Antalya, Turkey, Apr. 2012.

7. **Jeong-Yong Choi,** Kuan Soo Shin and Kwan Kim, "Raman Scattering of 4-Aminobenzenethiol sandwiched between Ag Nanoparticle and Smooth Au substrate: Effects of Size of Ag Nanoparticles and Excitation Wavelength" *The Third Asian Spectroscopy Conference* Xiamen, China, Nov. 2011.
8. **Jeong-Yong Choi,** Kuan Soo Shin and Kwan Kim, "Comparative Characteristics of Gold-Gold and Gold-Silver Nanogaps Probed by Raman Scattering Spectroscopy of 1,4-Phenylenediisocyanide" *Colloquium Spectroscopicum Internationale XXXVII*, Búzios, Brazil, Aug. 2011.
9. **Jeong-Yong Choi** and Kwan Kim, "Silanization of Ag-Deposited Magnetic Particles: An Efficient Route to Fabricate Magnetic Nanoparticle-Based Raman Barcode Materials" *2010 International Chemical Congress of Pacific Basin Societies*, Hawaii, USA, Dec. 2010.
10. **Jeong-Yong Choi,** Kuan Soo Shin and Kwan Kim, "Induction of SERS on Smooth Gold by Overlaid Ag-Coated Magnetic Particles" *5th International Conference on Advanced Vibrational Spectroscopy*, Melbourne, Australia, July 2009.

Domestic conferences

1. **Jeong-Yong Choi** and Kwan Kim, "Effect of foreign molecules on the SERS of probe molecules trapped in gaps between flat Ag and Ag nanoparticles" *2013 Asian Core Winter School* Busan, Korea, Jan. 2013
2. **Jeong-Yong Choi,** Kuan Soo Shin and Kwan Kim, "Silanization of Ag-Coated

Magnetite Particles: An Efficient Route to Fabricate Magnetic Raman Barcoding Materials" *The 105th Annual Meeting of the Korean Chemical Society*, Incheon, Korea, Apr. 2010.

요약 (국문초록)

1 장에서는 라만 분광법과 표면 증강 라만 산란 (Surface enhanced Raman scattering: SERS) 에 대한 기본적인 원리와 3 차원 유한 차분 시간 영역 방법 (3D finite-difference time domain (3D-FDTD))에 대해 간략히 설명하였다.

2장에서는 4-aminobenzenethiol (4-ABT)의 b2 모드에 대해 알아보았다. 4-ABT는 C_{2v} 라만 선택규칙에 따라 a_1 모드는 라만 활성이고 b_2 모드는 비활성이라 정규 라만 에서는 b_2모드를 관찰하기가 어렵다. 하지만 은에 흡착한 4-ABT의 라만을 얻으면 정규 라만 에서는 보이지 않는 띠들이 나타난다. Osawa 교수는 전위 의존 SERS를 통해 이 진동 띠가 4-ABT의 고유 b_2 모드에 해당한다고 해석하였다. 하지만 최근 이 진동 띠가 b_2 모드가 아닌 4-ABT가 표면 광 반응에 의해 아조 화합물인 4,4'-dimercaptoazobenzene (4,4'-DMAB)로 변환되어 이 화합물의 N=N 진동띠가 관찰된다는 주장이 제기되고 있다. 마찬가지로 4-nitrobenzenethiol (4-NBT)의 경우 기존에는 빛에 의해 4-ABT로 광 반응이 일어난다고 알려졌지만 최근 4-ABT가 아닌 4,4'-DMAB가 생성된다는 주장이 제기되고 있다. 이를 확인하기 위해 이 실험에서는 77K의 얼음 안과 실온에서 은에 흡착한 4-NBT과 4-ABT 의 라만을 얻어보았다. 먼저 실온에서는 4-ABT와 4-NBT 모두 b_2 모드가 관찰되었다 반면 저온에서 얻은 4-NBT의 SERS에서는 b_2 모드를 관찰할 수 없었고 4-ABT의 SERS에서만 b_2 모드를 확인할 수 있었다. 4-NBT가 열전자에 의해 광 반응을 하기 위해서는 N-

O결합이 끊어져야 한다. 하지만 얼음 안에서 N-O결합을 끊어내기 어렵기 때문에 광 반응이 일어나기 어렵지만, 4-ABT는 열전자에 의해 반응이 아닌 전자전이 효과가 일어나기 때문에 b_2 모드를 관찰 할 수 있었다. 만약 4-ABT가 광 반응을 통해4,4'-DMAB로 변한다면 얼음 안에서 b_2 모드를 관찰할 수 없었을 것이다. 이를 통해 4-NBT와 4-ABT의 SERS에서 나타나는 b_2 모드는 4,4'-DMAB에 의한 것이 아닌 4-ABT 고유의 진동 띠임을 확인하였다.

3 장에서는 평평한 금 표면과 금, 은 및 합금 나노 입자 사이의 4-ABT 의 SERS 를 통해 SERS 전자기적 증강에서 일컫는 열점에 대해 알아보고 이를 3D-FDTD 계산을 통해 이론적으로 검증하였다. 먼저 평평한 금 표면 위에 4-ABT 를 흡착하고 여기에 은 나노 입자를 올려 라만을 얻어보았다. 은 나노 입자 없을 때는 라만 신호가 나오지 않지만 그 위에 은 나노 입자를 얹으면 큰 신호를 확인 할 수 있었다. 이를 바탕으로 은 나노 입자의 크기와 레이저 파장에 따른 라만 신호를 관찰하였고, 나노 입자의 크기가 클수록 라만 세기가 크고, 568 nm 와 633 nm 파장에서 514, 488 nm 보다 큰 라만 신호를 얻을 수 있었다. 이는 FDTD 를 통해 이론적으로도 입증하였다.

두 번째로 평평한 금 표면에 금 은 합금 나노 입자 사이에 있는 1,4-phenylenediisocyanide (1,4-PDI)와 4-ABT 의 라만을 확인하였다. 우선, 나노 입자의 은 함량이 많을수록 파장과는 상관없이 큰 라만 세기를 얻을 수 있었다. 레이저 파장 별로 라만을 얻어보면 568 nm 가 가장 효과적인

라만 세기를 보였고 나노 입자의 금 함량이 많아질수록 633 nm 라만 세기가 커지는 것을 확인하였다. 이 결과 또한 FDTD 를 통한 이론적인 계산과 부합함을 확인하였다.

4 장에서는 금 표면에 4-NBT 를 흡착하고 그 위에 길이가 다른 1-alkanethiol 이 흡착된 은 나노 입자가 코팅된 1μm 실리카 비드를 얹어 라만을 얻어보고, 이를 통해 나노 틈 사이의 거리에 따른 열전자의 효과를 알아보았다. 2 장에서 설명한 바와 같이 은에 흡착된 4-NBT 는 빛을 통해 은에서 생성된 열전자에 의해 4-ABT 로 환원된다. 이 실험에서 은 나노 구조체에서 생성된 열전자가, 길이가 서로 다른 1-alkanethiol 의해 조절된 나노 틈을 통과해 4-NBT 를 환원 할 수 있음을 확인하였고, 나노 틈 사이의 거리와 레이저 파장에 따른 열전자의 효율을 측정하였다. 그 결과 나노 틈 사이의 거리가 가까울수록, 레이저 파장이 단파장일수록 4-NBT 가 4-ABT 로 잘 환원되는 것을 확인하였다.

주요어 : 표면 증강 라만 산란, 전자기 증강 메커니즘, 화학 증강 메커니즘, 열점, 열전자, b2 모드, 3 차원 유한 차분 시간 영역 방법, 4-Nitrobenzenethiol, 4-Aminobenzenethiol, 4,4′-Dimercaptoazobenzene, 나노틈

학번: 2008-22740